Influence of Alzheimer's disease related neuropathology on local microenvironment gene expression in the human inferior temporal cortex

Authors

Sang Ho Kwon[1,2,3], Sowmya Parthiban[*,4], Madhavi Tippani[*,2], Heena R. Divecha[2], Nicholas J. Eagles[2], Jashandeep S. Lobana[2], Stephen R. Williams[5], Michelle Mak[5], Rahul A. Bharadwaj[2], Joel E. Kleinman[2,6], Thomas M. Hyde[2,6,7], Stephanie C. Page[2], Stephanie C. Hicks[+,4,8], Keri Martinowich[+,2,3,6,9], Kristen R. Maynard[+,2,3,6], Leonardo Collado-Torres[+,2]

Affiliations

1. The Biochemistry, Cellular, and Molecular Biology Graduate Program, Johns Hopkins School of Medicine, Baltimore, MD, USA.
2. Lieber Institute for Brain Development, Johns Hopkins Medical Campus, Baltimore, MD, USA
3. The Solomon H. Snyder Department of Neuroscience, Johns Hopkins School of Medicine, Baltimore, MD, USA
4. Department of Biostatistics, Johns Hopkins Bloomberg School of Public Health, Baltimore, MD, USA
5. 10x Genomics, Pleasanton, CA, USA.
6. Department of Psychiatry and Behavioral Sciences, Johns Hopkins School of Medicine, Baltimore, MD, USA
7. Department of Neurology, Johns Hopkins School of Medicine, Baltimore, MD, USA
8. Malone Center for Engineering in Healthcare, Johns Hopkins University, Baltimore, MD, USA
9. The Kavli Neuroscience Discovery Institute, Johns Hopkins University, Baltimore, MD, USA

* Equal Contribution

+ Corresponding authors

Corresponding Authors

Stephanie C. Hicks: shicks19@jhu.edu
Keri Martinowich: keri.martinowich@libd.org
Kristen R. Maynard: kristen.maynard@libd.org
Leonardo Collado-Torres: lcolladotor@gmail.com

Keywords

Spatially-resolved transcriptomics, RNA-protein co-detection, neuropathology, Alzheimer's disease, amyloid-β (Aβ), phosphorylated tau (pTau)

Abstract

Neuropathological lesions in the brains of individuals affected with neurodegenerative disorders are hypothesized to trigger molecular and cellular processes that disturb homeostasis of local microenvironments. Here, we applied the 10x Genomics Visium Spatial Proteogenomics (Visium-SPG) platform, which measures spatial gene expression coupled with immunofluorescence protein co-detection, in post-mortem human brain tissue from individuals with late-stage Alzheimer's disease (AD) to investigate changes in spatial gene expression with respect to amyloid-β (Aβ) and hyperphosphorylated tau (pTau) pathology. We identified Aβ-associated transcriptomic signatures in the human inferior temporal cortex (ITC) during late-stage AD, which we further investigated at cellular resolution with combined immunofluorescence and single molecule fluorescent in situ hybridization (smFISH) co-detection technology. We present a workflow for analysis of Visium-SPG data and demonstrate the power of multi-omic profiling to identify spatially-localized changes in molecular dynamics that are linked to pathology in human brain disease. We provide the scientific community with web-based, interactive resources to access the datasets of the spatially resolved AD-related transcriptomes at https://research.libd.org/Visium_SPG_AD/.

Introduction

Pathological signaling cascades that alter homeostasis in brain microenvironments occur in various disorders including stroke, infection, tumor, and neurodegenerative diseases, as well as in response to traumatic brain injuries (1–6). The molecular and cellular landscape of the local tissue microenvironment is altered via release of cytokines, chemokines, and other secreted proteins, such as interleukin-1β (IL-1β), C-C motif chemokine ligand 2 (CCL2), and reactive oxygen species (ROS), which triggers downstream signaling cascades via second messenger molecules (7–11). Pathological lesions often exhibit remarkable features such as apoptosis, necrosis, neuroinflammation or changes in cell morphology that can be detected with histological or immunohistochemical staining of post-mortem brain tissue. For example, Alzheimer's disease (AD) is characterized by two major neuropathologies - extracellular deposition of amyloid-beta (Aβ) peptides that form senile plaques, and intracellular inclusions of hyperphosphorylated tau (pTau) proteins that form various neurofibrillary elements, including tangles (12–14). The progressive accumulation of Aβ and pTau is hypothesized to functionally contribute to cognitive decline and dementia, and to contribute to cell death during disease progression (12,15). However, the pathophysiological mechanisms rendering Aβ and pTau neurotoxic are still not fully understood (16). Identifying how plaques and tangles contribute to molecular and cellular signaling cascades that trigger cell death in the local microenvironment is essential to develop novel approaches for preventing or reversing disease progression in AD.

Several studies have now deployed spatially-resolved transcriptomics (SRT) to study spatial gene expression in mouse models of AD (17,18). However, only humans and some non-human primates naturally develop plaques, tangles and dementia, and hence rodent models cannot fully recapitulate neurodegenerative diseases in humans (19,20). Therefore, investigative studies in human brain tissue from donors diagnosed with AD that carry plaques and tangles are indispensable to study the molecular sequelae associated with Aβ and pTau deposition. To better understand how Aβ deposition and pTau accumulation in the human brain impacts molecular signaling in the local tissue environment in late-stage AD, we utilized spatial profiling coupled with multiplex immunofluorescence using the 10x Genomics Visium Spatial Proteogenomics platform (Visium-SPG) to generate a proteomic-based, spatially-resolved, transcriptome-scale map of the human inferior temporal cortex (ITC), a region which displays reduced cortical thickness in AD (21–23). By combining proteomic and transcriptomic information, Visium-SPG allows for quantification of transcriptional dynamics with respect to spatially-localized pathology. Here, we evaluated the utility of the Visium-SPG platform by testing the hypothesis that local tissue microenvironments in close proximity to AD-related neuropathology have distinct molecular signatures. We first immunostained post-mortem human brain tissue sections from donors diagnosed with AD for Aβ and pTau, and then conducted SRT using the Visium-SPG platform. Integration of proteomic and transcriptomic data allowed us to measure gene expression profiles within local tissue microenvironments that were spatially defined by the presence of pathology. Our multi-omics approach identified genes differentially expressed by proximity to Aβ, which we further validated at cellular resolution using RNAscope smFISH combined with Aβ immunodetection. To make these data easily available to the neuroscience community, we generated user-friendly web resources to further explore the dataset.

Results

Experimental design and study overview

To identify local gene expression profiles in the tissue microenvironment with respect to Aβ and pTau deposition, we employed the 10x Genomics Visium-SPG technology in tissue sections from the ITC of 4 human brain donors (**Figure 1A** and **Table S1**). Three donors were clinically diagnosed with AD (Braak V-VI/CERAD Frequent), and 1 donor was an age-matched neurotypical control. Tissue blocks containing the ITC (**Figure S1A**) were collected onto a Visium spatial gene expression slide with 4 capture arrays, where each array contains ~5,000 expression spots bearing spatially-barcoded oligonucleotide probes (24). For each donor, we performed 2-3 spatial replicates, resulting in a total of 10 samples. Following collection onto capture arrays, tissue sections were stained using monoclonal primary antibodies, 6E10 (25) and AH36 (26,27) to label Aβ and pTau, respectively. Immediately following staining, the entire slide was imaged and then processed for segmentation of Aβ and pTau signals against the confounding noises and artifacts due to lipofuscin and particulates of ribonucleoside vanadyl complex (RVC) ribonuclease inhibitor (**Figure S2** and **Methods**). We confirmed that the staining protocol of Visium-SPG detected Aβ plaques and various forms of neurofibrillary elements, including tangles (**Figure 1B**). Immunostaining and image processing workflows were validated for specificity using images from neurotypical control samples, which largely lacked pathology (**Figure S3**). Following image acquisition, tissue sections underwent permeabilization (**Figure S1B**), followed by on-slide cDNA synthesis, amplification and subsequent library construction. The resulting transcriptomic data from the sequenced libraries was computationally aligned with the immunofluorescence image data to integrate transcriptomic and proteomic information for each tissue sample. We confirmed the spatial orientation of white and gray matter in each tissue section by visualizing marker genes for oligodendrocytes (*MOBP)* and neurons (*SNAP25)* (**Figure 1C**, **Figure S3B**, **Figure S4**, and **Figure S5**). The final image segmentation of Aβ and pTau was used to classify Visium spots into different AD-related neuropathological categories. Following Visium spot classification, we constructed spatial maps of gene expression by analyzing transcriptomic data with respect to AD-related pathology categories (**Figure 1D** and **Figure S6**).

Gene expression profiling of human brain microenvironments with AD-related neuropathology

While imaging of tissue immunostained for Aβ and pTau revealed diverse spatial patterns of AD pathology in the human ITC (**Figure 1B**), classification of these pathologies is complicated due to the existence of multiple variations of Aβ plaques (e.g. diffuse versus neuritic) and neurofibrillary elements (e.g. tangles versus neuropil threads) (28,29). To simplify classifications for subsequent analysis, we first categorized expression spots based on the presence or absence of Aβ or pTau (**Figure 2A**). This resulted in 7 broad subtypes of spots: 1) containing no Aβ and no pTau, 2) containing only Aβ, 3) containing only pTau, 4) containing both Aβ and pTau, 5) directly adjacent to Aβ spots, 6) directly adjacent to pTau spots, and 7) directly adjacent to spots containing both Aβ and

pTau. The spot categories from 2 to 4 (Aβ, pTau, both) and from 5 to 7 (next_Aβ, next_pTau, next_both) each represent the core and periphery of the brain microenvironment associated with Aβ, pTau, and the combination of the two. Of note, Aβ plaques and different neurofibrillary forms of pTau varied in shape, number, and size within a donor across the different replicates (**Figure S7A**). Given the heterogeneous appearance and variability in pathological load within individual Visium spots, we focused on Visium spots containing relatively high burdens of neuropathology. We selected spots with robust pathology in the AD samples by thresholding for the number and size of plaques and/or neurofibrillary elements. To do this, we first identified the regions of interest (ROIs) to indicate plaques and tangles as ROI objects. We set a baseline cut-off value in the ROI object counts (number) and pixel-based proportion (size) based on what was observed in the neurotypical control samples. Spots above this threshold were then classified according to binary expression of Aβ and/or pTau (**Figure S7B**-**C**).

To address the possibility of synergistic effects of Aβ and pTau co-expression (30–32) as well as the extracellular effects of Aβ peptides (33,34), we prioritized spots containing both Aβ and pTau (both), followed by spots containing Aβ pathology (Aβ), pTau pathology (pTau), and then spots adjacent to Aβ and pTau (next_both; n_bo), Aβ pathology (next_Aβ; n_Aβ), and pTau pathology (next_pTau; n_pT). Spots with no significant pathology were labeled as 'none'. This hierarchical classification of the 7 spot categories allowed for inclusion of a sufficient number of spots for the 'both' category (**Figure S8** and **Methods**). We then calculated a number of quality control (QC) metrics, identifying low-quality spots due to low library size, low number of expressed genes, or high proportions of mitochondrial reads and only dropped low library size spots on the tissue edges (**Figure S9** and **Methods**). Since AD neuropathology is most abundant in the cortical laminae of the human cortex (35–37), we focused our analysis on spots located in the gray matter (**Figure 2B**). To identify the gray matter using a data-driven approach, we first applied batch correction to the 10 tissue samples using *Harmony* (38) (**Figure S10**), and then employed *BayesSpace* (39), an algorithm for unsupervised spatial clustering. At cluster number k=2, we identified spots localizing to the gray and white matter (**Figure S11A**). We verified the identity of *BayesSpace* clusters by spatially registering (40) these spatial domains to manually annotated cortical layers and white matter from our previously published work in the dorsolateral prefrontal cortex (DLPFC) (24) (**Figure S11B**). *BayesSpace* cluster 1 was enriched for genes expressed in the gray matter while *BayesSpace* cluster 2 was enriched for genes expressed in the white matter. As expected, the gray matter-associated *BayesSpace* cluster 1 was enriched with numerous pathology-containing spots associated with Aβ and pTau pathology (**Figure 2B** and **Figure S8)**. Therefore, focusing on the gray matter only, we next pseudo-bulked the unique molecular identifier (UMI) counts for each gene within each individual pathological category across each AD sample. This generated a total of 41 pathology-enriched gene expression profiles across the 7 AD samples (**Figure 2A**) with at least 15 spots per combination, out of the possible 49 gene expression profiles.

Principal component analysis (PCA) revealed that a significant source of biological variation in these 41 pathology-enriched profiles was associated with pathological categories, particularly between Aβ-related categories against the others (**Figure 2C**). To study changes in gene expression associated with these pathological categories, we identified differentially expressed genes (DEGs) between the 7 pathological categories using linear mixed effects modeling. In particular, we used an 'enrichment' model (24,40) in which one pathological category was compared to all other categories. Using this strategy, we identified 9 up-regulated and 687 down-regulated DEGs for the Aβ category, and 51 up-regulated and 2,319 down-regulated DEGs for the next_Aβ category, all with a false discovery rate (FDR) of less than 0.1 (**Figure 2D**, **Table S2**, and **Table S3**). No significant DEGs were identified in the remaining 5 categories (**Figure S12A**). Gene expression levels of representative DEGs for the Aβ and next_Aβ category illustrate their degree of enrichment and depletion (**Figure 2E**). The corresponding spatial gene expression patterns are also depicted in the spot plots (**Figure 2F**). We identified two DEGs implicated in the ubiquitin-proteasome pathway, suggesting dysregulated protein degradation around Aβ plaques. Ubiquitin conjugating enzyme E2 A (*UBE2A*) was enriched within the Aβ category compared to all other spot categories (p=4.90∗10^{-3}), while 26S proteasome AAA-ATPase subunit RPT3 (*PSMC4*) was depleted (p=4.21∗10^{-7}). We also identified complement component 3 (*C3*) and protein phosphatase 3 catalytic subunit alpha (*PPP3CA*) as differentially expressed within the next_Aβ category. Within the gray matter, *C3* was enriched in the next_Aβ category compared to all other categories (p=1.93∗10^{-3}), while *PPP3CA* was depleted (p=4.24∗10^{-3}).

To investigate the gene expression profile of the extended Aβ-associated microenvironment spanning both Aβ and next_Aβ spots, we collapsed the Aβ and next_Aβ spots into a single category and ran differential expression testing compared to the other 5 pathological categories using the same enrichment model (**Table S4**). Based on an exploratory pathway analysis, several DEGs involved in apoptosis, JAK-STAT signaling pathways, inflammation, and cellular response to stress were enriched in the extended Aβ-associated microenvironment. These included genes (**Figure S12B**) encoding the TNF receptor superfamily member 1A (*TNFRSF1A*; p=8.18∗10^{-4}) (41–43), cytochrome P450 family 1 subfamily B member 1 (*CYP1B1*; p=1.37∗10^{-3}) (44,45), zinc finger protein 385A (*ZNF385A*; p=1.06∗10^{-4}) (46), RIO kinase 3 (*RIOK3*; p=1.08∗10^{-3}) (47), metallothionein 1F (*MT1F*; p=5.00∗10^{-4}) (48), and sushi domain containing 6 (*SUSD6*; p=2.68∗10^{-5}) (49), all of which have been recently reported as being associated with AD in human and mouse genomic and transcriptomic studies (50–55). We also identified several depleted DEGs, such as autophagy related 5 (*ATG5*; p=9.87∗10^{-4}), DnaJ heat shock protein family Hsp40 member A3 (*DNAJA3*; p=3.21∗10^{-4}), ubiquitin protein ligase E3 component N-recognin 3 (*UBR3*; p=1.26∗10^{-3}), ubiquitin like modifier activating enzyme 6 (*UBA6*; p=7.81∗10^{-4}), cyclin dependent kinase 5 (*CDK5*; p=2.41∗10^{-4}), and SH3 and multiple ankyrin repeat domains 3 (*SHANK3*; p=7.26∗10^{-5}) (**Figure S12C**). These genes are associated with autophagy (56,57), protein ubiquitination (58), and synaptic plasticity (59,60), which are well-established biological functions associated with AD. Of note, *ZNF385A* (p=8.82∗10^{-1} for next_Aβ) and *SUSD6* (p=2.94∗10^{-2} for next_Aβ) were not previously identified as statistically significant DEGs in any of the 7 spatially resolved pathological categories when Aβ and next_Aβ spots were not collapsed (**Figure S12D**). In summary, using Visium-SPG, we identified a set of genes differentially expressed in the core (Aβ spots) and peripheral (next_Aβ spots) compartments, as well as in the extended Aβ-associated microenvironment spanning the two compartments. Our analysis suggests the potential involvement of stress responses linked to protein degradation and inflammation, as well as regulation of synaptic plasticity in the Aβ-associated microenvironment.

Next, to add clinical relevance to our integrated spatial gene expression and pathology maps, we performed multi-marker analysis of genomic annotation (MAGMA) (61) to evaluate whether genes associated with genetic risk for AD (62), frontotemporal dementia (FTD) (63), and Parkinson's disease (PD) (64) genome-wide association studies (GWAS) are linked to DEGs from the Aβ-associated microenvironment. We found that spots classified as next_Aβ, which represent the peripheral compartments of Aβ-associated microenvironments, harbored a substantial genetic risk for AD and PD (**Figure S13A**). Using gene set enrichment analyses, we further evaluated whether different Aβ-associated microenvironments were enriched and/or depleted in 1) the co-expression gene module M109 associated with both cognitive decline and Aβ pathology in AD based on an bulk RNA sequencing (bulk RNA-seq) data from the ROSMAP cohort by Mostafavi et al (65) or 2) the cell type-specific DEGs in the entorhinal cortex between AD donors and controls from a single nucleus RNA sequencing (snRNA-seq) study by Grubman et al (66). We found no statistically significant (p<0.05) enrichment with bulk RNA-seq (**Figure S13B**) but we noted that genes differentially expressed in microglia between AD donors and controls were enriched in the periphery of the Aβ-associated microenvironments, suggesting an important role for microglia in pathological processes in the late stage of AD (p=0.047) (**Figure S13C**).

Spatial gene expression of Aβ-associated microenvironments at single cell resolution

The resolution of the Visium platform is limited by the size and spacing of spots across the array. First, the size of the expression spot (55μm diameter) does not allow for cellular or sub-cellular resolution. In the present study, we observed an average of 4.5 nuclei per spot, which is consistent with our previous study of the human DLPFC where we observed an average of 3.3 cell bodies per spot (24). In addition, since spots are spaced in a honeycomb pattern with 100μm distance center-to-center between neighboring spots, transcriptomic data is not captured in the 45μm of inter-spot space (67). To add cellular resolution to our Visium data and further explore the expression of promising DEGs related to AD pathology, we used RNAscope smFISH combined with immunofluorescence (RNA-Protein co-detection workflow; FISH-IF) to define transcript expression in single cells located in the vicinity of Aβ plaques (**Figure 3A**).

In particular, we focused on differentially expressed genes in the Aβ and next_Aβ categories at FDR<0.1. We selected 6 DEGs for follow-up based on their biological significance in AD as well as availability for commercialized RNAscope probes. With Visium-SPG, we identified isopentenyl-diphosphate delta isomerase 1 (*IDI1*; p=1.80∗10^{-3} for Aβ>rest) and *C3* as enriched in the vicinity of Aβ plaques. We also identified nerve injury-induced protein 1 (*NINJ1*; p=1.87∗10^{-5} for Aβ<rest), *PPP3CA*, ubiquitin C-terminal hydrolase L1 (*UCHL1*; p=7.62∗10^{-4} for next_Aβ<rest), and somatostatin (*SST*; p=2.68∗10^{-3} for next_Aβ<rest) as depleted in Aβ-adjacent Visium spots (**Figure S14A**). We performed FISH for each selected gene while immunolabeling Aβ plaques in the same tissue sections. We then completed segmentation using HALO software (68–70) to identify Aβ plaques and surrounding cells expressing genes of interest (GOI), which we refer to as GOI expressors (**Figure 3B** and **Figure S15A**). The number of RNAscope puncta was quantified in GOI expressors using the FISH-IF module in HALO (**Figure 3B** and **Figure S15B**-**C**). After image segmentation and quantification, the proximity between Aβ and GOI expressors was analyzed using the spatial analysis module in HALO (**Figure S15D**). To understand the spatial relationship between Aβ plaques and adjacent cells, including GOI expressors, we approximated the Aβ-associated microenvironment used in Visium analyses by introducing a geometric layout based on the Visium spot grid line system. Specifically, we set a maximum proximity between segmented Aβ plaques and neighboring cells at 127.5μm, which is the radial distance from the center of a Visium spot containing Aβ to the opposite end of an adjacent plaque-free spot (**Figure 3B**). To finely resolve spatial gene expression gradients, we divided this approximated Aβ-associated microenvironment into 6 evenly-spaced, concentric rings for a total of 7 sub-regions in which GOI expressors were classified based on their location to neighboring plaques. This proximity analysis was performed for each tissue section per donor, and the spatially classified cells were pooled across the 4 AD donors. The cumulative number of cells measured in each sub-region varied between 1,615 and 26,789 (with an average median of 14,505) (**Figure S16C**), and the total number of segmented fragments of Aβ plaques (**Figure S15C**) per each tissue section ranged from 1,671 to 5,413 (with a mean of 3,359, a median of 3,659, and a standard deviation of 1,135).

Using this approach, we finely resolved changes in gene expression gradients identified with Visium-SPG within Aβ-associated microenvironment at cellular resolution (**Figure 3C**-**D**). Consistent with Visium data, *IDI1* was lowly expressed in the area closest to Aβ plaques (0-21.25μm), but was significantly increased in the region extending to 106.25μm, at which point expression decreased, reaching its lowest expression levels in the regions farthest from plaques (>127.5μm). *C3* expression peaked in regions directly adjacent to plaques, followed by a downward trajectory and then a second peak beyond the defined local microenvironment at 127.5μm (**Figure 3D** and **Figure S16D**). The lowest levels of *NINJ1* were observed close to plaques, and *PPP3CA* was slightly enriched in the inner microenvironment (21.25-63.75μm), but its progressive decrement was detected on the outskirts (>85μm). Similar to this declining trend, *UCHL1* and *SST* both exhibited statistically significant decreases in gene expression levels in the distal region of the microenvironment when the total cell population was counted as a normalization factor (**Figure S16A**). In summary, we defined spatial gene expression patterns of the Aβ-associated genes identified with Visium-SPG at cellular resolution using RNAscope FISH-IF to add further context to how their gene expression levels become spatially variable with respect to proximity to Aβ pathology.

Discussion

Application of SRT to the study of human brain disorders (71,72) has rapidly increased due to the technology's innovative ability to preserve spatial-anatomical context while assessing gene expression. Here, we demonstrate, to our knowledge, the first use case of 10x Genomics Visium-SPG in AD, which incorporates protein co-detection with SRT, in human post-mortem brain tissue to investigate the influence of AD-related neuropathology on local gene expression. The multi-omic approach of immunofluorescent (IF) staining followed by SRT in the Visium-SPG assay allows for simultaneous detection of mRNA with specific proteins of interest. This integrative approach can resolve local transcriptomic profiles of pathology-associated proteins to comprehensively assess the molecular impact of neuropathology on spatially-defined microenvironments. Simultaneous detection of mRNA and proteins on the same tissue section reduces the computational burden associated with aligning spatially adjacent tissue sections and their latent structural variations in tissue architecture (18,73–75).

Using Visium-SPG, we generated transcriptome-scale tissue atlases of human ITC harboring AD-related neuropathology. The ITC is a cortical structure that succumbs to progressive accumulation of Aβ and pTau in AD (76,77). We focused on late-stage AD (Braak V-VI/CERAD Frequent) to define the biological consequences of severe pathology. Consistent with prior clinicopathological examinations, our IF staining revealed heavily intertwined Aβ and pTau pathology, which spanned various cellular and subcellular compartments. Diffuse and neuritic plaques were observed throughout the tissue sections, along with a variety of neurofibrillary elements including neuropil threads and tangles. To investigate dynamic transcriptional patterns associated with Aβ and pTau depositions, we computationally registered the IF image data with SRT data from the same tissue section and aligned Aβ and pTau protein signals with spatially resolved transcriptomics. AD neuropathology within Visium expression spots was classified using a binary categorization based on the absence or presence of protein signal. We subsequently classified spots according to a pathology hierarchy that prioritized the 'both' pathology as we were most interested in potential synergies due to co-localization or proximity between Aβ and pTau. Alternative hierarchies prioritizing either Aβ or pTau did not result in the identification of many 'both' spots due to the categorization into Aβ or pTau only. Pathological maps were generated by measuring the number of ROI objects and proportion of pixels within the ROIs per spot to estimate local pathological burden. We used pseudo-bulking and differential gene expression analyses to investigate molecular changes in microenvironments with a substantial pathological burden of Aβ, pTau or both, as well as their neighboring microenvironments (next_Aβ, next_pTau, and next_both), and microenvironments without significant pathology (none). By integrating spatial transcriptomic data with pathology maps derived from immunofluorescence, we identified differentially expressed genes (DEGs) between the core (Aβ) or periphery (next_Aβ) of the Aβ-associated microenvironments against the other six pathological categories. These DEGs included *UBE2A*, *PSMC4*, *C3*, and *PPP3CA*. Additionally, we performed a sensitivity analysis by combining Aβ and next_Aβ spots into a single category to describe the extended Aβ microenvironment (Aβ_env) that allowed us to identify new Aβ-associated DEGs, such as *ZNF385A* and *SUSD6*. These genes were not initially identified when Aβ and next_Aβ spots were analyzed separately, likely due to their similar gene expression patterns between Aβ and next_Aβ spots. The DEGs we identified suggest a handful of biological processes and signaling networks that may

contribute to the neurodegenerative and proinflammatory conditions in the vicinity of Aβ plaques. Among them were the cell survival/death signaling pathways (e.g., *CYP1B1*, *CDK5*, *TNFRSF1A*, *ZNF385A*, *BCL2*, *BID*, and *AIFM1*), the complement cascade system (e.g., *C3*, *C1QA*, and *C1QBP*) as well as the ubiquitin proteasome system (e.g., *UBE2/4* family, *UBA3B*, *UBA6*, *UCHL1*, *PSMA1*/*3*/*5*/*6*, *PSMC4*/*5*, and *PSMD4*/*6*/*7*/*13*), all of which are commonly dysregulated in neurodegenerative diseases, including AD (52,78–90). Importantly, some of the identified biological processes, especially the complement system, were also found in a SRT study recently published from brain tissue in a mouse model of AD (18).

To investigate the pathobiological implications of spatially-resolved Aβ-associated DEGs in neurodegeneration and dementia, we performed MAGMA and found that the peripheral microenvironments of Aβ plaques (next_Aβ spots) harbored significant genetic risk for AD. We further examined the expression of candidate genes associated with genetic risk for AD in our different Aβ microenvironments. Surprisingly, genes associated with increased risk for early- and late-onset AD did not exhibit differential expression in any of the 7 pathology-associated microenvironments in this late-stage AD tissue, with the exception of ADAM10 (91), a metalloprotease whose gene expression was reduced in the core region of Aβ-associated microenvironments (**Figure S14B**). This result could be due to their ubiquitous (e.g., *APOE*, *CLU*, *PLD3*, and *APP*) or sparse (e.g.,*TREM2* and *PSEN2*) gene expression patterns, which limit their detection of significant spatial variation in AD. Intriguingly, no enrichment of genes associated with frontotemporal dementia (FTD) was found in the core Aβ microenvironments. This observation appears to be consistent with the notion that FTD is devoid of cerebral amyloidosis (92,93), supporting the specificity of Aβ pathology in late-stage AD. Additionally, we observed a strong association between the peripheral compartment of Aβ microenvironment and Parkinson's disease (PD), which may suggest a potentially shared genetic risk between AD and PD in this local brain microenvironment. Our subsequent clinical gene set enrichment analyses using genes identified in bulk RNA-seq (65) and single-nucleus RNA-seq (snRNA-seq) studies (66) confirmed the relevance of our dataset to AD while providing new technical insights into leveraging transcriptomic studies for gene set enrichment analyses. Notably, while genes identified from co-expression modules derived from bulk RNA-seq analysis using *SpeakEasy* (65,94), which is similar to *WGCNA* (95), did not reveal any enrichments, genes differentially expressed between cell type clusters derived from snRNA-seq analysis revealed spatial enrichment patterns of microglia in the peripheral Aβ-associated microenvironments. This example highlights the utility of leveraging integrated single cell/nucleus and spatial transcriptomic approaches to understand the complexity of human brain transcriptomes underlying AD. Indeed, the application of emerging computational analyses for large-scale SRT studies, including spot-level deconvolution (96–98) and cell-to-cell communication (99), could help to better characterize the multicellular composition and crosstalk within the Aβ plaque microenvironments in AD.

To further explore the DEGs associated with spatially-resolved Aβ microenvironments, we conducted RNAscope FISH-IF for a selected subset of genes identified with Visium-SPG. The cholesterol metabolism gene *IDI1* and complement gene *C3* were broadly enriched in the vicinity of Aβ-associated microenvironments, whereas *NINJ1* was significantly depleted in the immediate vicinity of Aβ plaques. *PPP3CA*, *UCHL1*, and *SST* were enriched within Aβ-associated microenvironments, but their enrichment gradually decreased with distance from the Aβ-associated microenvironment. These differential gene expression patterns and topography appeared to inform molecular and cellular events (100) occurring in the proximity of Aβ plaques during the late stages of AD. For example, cholesterol synthesis is altered in both neurons and glial cells in AD and is linked to Aβ accumulation (101–107), which may support our observation of the increased *IDI1* gene expression proximal to Aβ deposition. Elevated *C3* may signify enriched glial cell populations in the vicinity of Aβ and the inflammatory crosstalk between microglia and astrocytes (108,109). Indeed, preliminary findings show the presence of $C3^+$ microglia (TMEM119) and $C3^+$ astrocytes (GFAP) near Aβ plaques (**Figure S16D**), but more work will be needed in the future to determine the extent to which this occurs at plaques across the cortex. In terms of the spatially depleted genes, *NINJ1* was initially identified as a nerve regeneration factor in the peripheral nervous system, but in the central nervous system, it is better known as a mediator of immune cell migration and non-programmed cell death such as necroptosis and pyroptosis by directing membrane rupture to release proinflammatory factors for elimination of pathogenic molecules (110). The decrease in *NINJ1* expression near Aβ can be interpreted in two ways: as a result of lytic cell death of immune cells or as a result of silenced pro-inflammatory reactions that promote the formation and/or spread of Aβ plaques (111,112). Further studies are required to understand how inflammatory factors like *C3* and *NINJ1* coordinate immune reactions in the vicinity of Aβ plaques. The calmodulin-dependent serine/threonine protein phosphatase *PPP3CA* (calcineurin), the deubiquitinating enzyme *UCHL1*, and the neuropeptide *SST* are all implicated in AD (85,113–115). Aβ plaques appear to be enriched near cells expressing these DEGs, but their density decreases with distance from these cells. Given that these three genes are dominantly expressed in neuronal populations in the human cortex (116), it will be informative in the future to investigate the mechanisms underlying the spatial relationship between the neuronal types and Aβ in terms of the plaque formation and transmission. Taken together, RNAscope-based analyses delineated local variations in gene expression around Aβ at cellular resolution. While the majority of tested genes showed good correspondence between Visium-SPG and RNAscope FISH-IF, there were examples where Visium-SPG patterns did not match spatial gene expression patterns with RNAscope FISH-IF. For example, in the Visium-SPG data, *C3* was highly enriched in the peripheral regions of Aβ plaque microenvironments, while with RNAscope FISH-IF, the peak was identified within the core microenvironments. Discrepancies between the two platforms are likely due to the difference in resolution, and hence using orthogonal techniques for further characterizing DEGs identified with Visium-SPG may provide important additional information.

While this study provides the groundwork for identifying changes in gene expression associated with spatially-resolved AD neuropathology, it has several important limitations that can be addressed in future research. First, our analysis focused on the gray matter. We noted a sparse distribution of Aβ (28) and/or pTau (117) in the white matter region near the deeper cortical layers. In particular, these Aβ-associated Visium spots in the white matter expressed several endothelial markers including *CLDN5* (Claudin 5) *and MCAM* (CD146). Cerebral amyloid plaques are rarely found in white matter (118), but our finding suggests that the Aβ deposits may pertain to vascular Aβ localized in capillaries and blood vessels (119–122). It would be interesting to investigate these subcortical Aβ-associated vascular microenvironments, given their putative contribution in white matter hyperintensity and cerebrovascular dysfunction in AD (123–128). Second, while our categorical pathology classification approach allowed us to identify DEGs associated with different pathological microenvironments, we acknowledge it may not address the full spatial heterogeneity of AD pathology, and in the future, more complex modeling approaches could be implemented. With more fine grained measurements one could identify DEGs whose spatial gene expression patterns are sensitive to the pathological gradients of Aβ and pTau. Third, limitations in the sample size precluded assessing differences across the spectrum of AD severity. Since the primary objective was to investigate microenvironments bearing AD-related neuropathology compared to those without, we used a within-subjects design and did not directly compare gene expression between AD donors and a neurotypical control. Nevertheless, our study provides a computational framework for designing future studies in larger cohorts that scale sample size to increase power to answer other biological questions. New innovations in next-generation sequencing, imaging, and computational platforms will also enable follow-up work that has the ability to profile the clinical heterogeneity of AD (129) across other related neurodegenerative diseases and dementias (130,131) as well as across cortical layers (132,133), subcortical structures (28,66,134,135), and developmental stages (136). Lastly, Visium-SPG is currently limited to surveying only a few proteins of interest, but new technologies that use DNA-barcoding approaches for protein detection (137–139) are now emerging. These enhanced platforms will improve the ability to use multiplexed antibodies to simultaneously track different variants of pathogenic Aβ and pTau (140,141). Emerging SRT platforms

using complementary in situ sequencing approaches also have enhanced spatial resolution (142–144), which can finely resolve transcriptomic information at cellular and subcellular levels. Such features will be highly advantageous for detecting subtle differences in transcriptomic profiles of Aβ and pTau elements that are dispersed across neuronal and synaptic structures.

Conclusion

In summary, we used Visium-SPG to identify local transcriptional signatures in spatially-defined Aβ-associated microenvironments in the inferior temporal cortex (ITC) of donors with late-stage AD. We applied RNAscope FISH-IF to further explore spatial gene expression patterns of Visium-identified genes associated with Aβ at cellular resolution. As a proof of concept study, our work lays the groundwork for deploying multi-omic approaches using both proteomics and transcriptomics to understand spatial heterogeneity in human brain diseases. While future studies are needed to produce mechanistic insights, the ongoing collective efforts to deepen single -omics with multi -omics data of different modalities, for example, with genomics, epigenomics, and metabolomics (145–147) are anticipated to contribute to information that sheds light on the complex biological processes and multifactorial nature of AD. To support ongoing effort in the neuroscience community to better understand molecular changes associated with AD, our work is distributed as a resource composed of freely accessible interactive websites for exploring the processed data in analysis-readyR/Bioconductor objects as well as raw data and reproducible code for the computational analyses.

Methods

Post-mortem human brain tissue samples

Brain donations in the Lieber Institute for Brain Development (LIBD) Human Brain Repository were collected from the County of Santa Clara Medical Examiner-Coroner Office in San Jose, CA and from the Western Michigan University Homer Stryker MD School of Medicine, Department of Pathology in Kalamazoo, MI, both under WCG IRB protocol #20111080. Four donors with Alzheimer's disease (AD) ranged in age from 66 to 91 and were matched for age and demographics (European ancestry) with 1 neurotypical donor (**Table S1**). Clinical characterization, diagnoses, and macro- and microscopic neuropathological examinations were performed on all samples using a standardized paradigm. A 15-item series of questions assessing changes in memory, cognition, movement, caregiving, and daily functioning were obtained for all donors, as part of the LIBD Telephone Autopsy Questionnaire. Details of tissue acquisition, handling, processing, dissection, clinical characterization, diagnoses, neuropathological examinations, RNA extraction and quality control measures have been described previously (148,149). Alzheimer's neuropathology was measured and rated with the Braak staging schema and CERAD scoring system (150) to evaluate tau neurofibrillary tangle burden and senile plaque burden, respectively. Scales range from Braak stage 0 to Braak stage VI, and CERAD is none-sparse-moderate-frequent.

Visium-SPG immunofluorescence (IF) staining and image acquisition

Inferior temporal cortex (ITC, Brodmann area 20) from 3 AD subjects and 1 age-matched control was microdissected using a hand-held dental drill. Frozen samples were embedded in OCT (TissueTek Sakura, Cat# 4583) and cryosectioned at 10 micron thickness (Leica, CM3050s). Two to three non-adjacent tissue sections from the same ITC block were mounted on a Visium Spatial Gene Expression Slide (10x Genomics, Cat# 2000233) for each donor, with the exception of the neurotypical donor Br3874, for which two different brain blocks were used to address their different larminar structures. IF staining was performed according to the manufacturer's instructions (10x Genomics, CG000312 Rev B) with no modifications. To maximize preservation of RNA integrity for the downstream Visium-SPG assay, the IF staining procedure was optimized to accommodate methanol fixation and short incubation periods. Briefly, tissue sections on a Visium slide were fixed for 30 minutes in pre-chilled methanol, treated with blocking buffer containing BSA (Miltenyi Biotec, Cat# 130-091-376) and the ribonuclease inhibitor, ribonucleoside-vanadyl complex RVC (New England Biolabs, Cat# S1402S), and incubated for 30 minutes at room temperature with primary antibodies against Aβ, pTau, GFAP, and MAP2 [mouse anti-β-amyloid antibody, clone 6E10 (Biolegend, Cat# 803001, 1:50), rabbit anti-Tau antibody pSer202/pThr205, clone AH36 (StressMarq, Cat# SMC601, 1:100), rat anti-glial fibrillary acidic protein (GFAP) antibody (Thermofisher, Cat# 13-0300, 1:70), and chicken anti-microtubule-associated protein 2 (MAP2) antibody (Abcam, Cat# ab92434, 1:70)]. Following a series of 5 washes, appropriate host species secondary antibodies conjugated to Alexa dyes were applied for 30 minutes at room temperature [donkey anti-mouse IgG conjugated to Alexa 488 (Thermofisher, Cat# A-21202, 1:200) donkey anti-rabbit IgG conjugated to Alexa 555 (Thermofisher, Cat# A-31572, 1:350), donkey anti-rat IgG conjugated to Alexa 594 (Thermofisher, Cat# A-21209, 1:400), and goat anti-chicken IgY conjugated to Alexa 633 (Thermofisher, Cat# A-21103, 1:300)]. DAPI (Thermofisher, Cat# D1306, 1:3000, 1.67 µg/ml for final concentration) was applied for nuclear counterstaining at the same time with the secondary antibodies. After a series of 5 washes and 20 immersions in 3x saline-sodium citrate (SSC) buffer diluted from 20x concentrate (Quality Biological, Cat# 351-003-131), the slide was coverslipped with 85% glycerol supplemented with RiboLock RNase inhibitors (Thermofisher, Cat# EO0382, 2 U/µl for a final concentration).

Slides were imaged on a Vectra Polaris (Akoya Biosciences) slide scanner with a MOTiF™ technology at 20x magnification using multispectral imaging and whole slide scanning. The exposure time per channel was as follows: 1.65-1.80 msec for DAPI; 380-400 msec for Opal 520; 43-65 msec for Opal 570; 150-178 msec for Opal 620; 615-643 msec for Opal 690; 100 msec for Autofluorescence (AF). There are several technical challenges to note regarding the staining, imaging, and analysis steps. First, chemical-based quenchers such as Trueblack (Biotium) were not used to overcome the lipofuscin autofluorescence in post-mortem human tissue due to their potential incompatibility with the Visium platform. Secondly, the dark green precipitates of the RVC ribonuclease inhibitor introduced particulate matter that added background fluorescence. This was an unknown issue in early releases of the Visium-SPG protocol, but it has been addressed in the recent manuals from 10x Genomics (10x Genomics, CG000312 Rev D) and resolved by heating the compound for improved suspension. Lastly, the current specifications of the whole-slide scanning system, though offering impressive speed and performance for multi-spectral imaging to accommodate the time-sensitive Visium-SPG workflow, are limited in its capacity for automatic signal intensity adjustment. This limitation restricted our ability to minimize local saturation of signals across several fields of view while imaging the entire tissue-wide neuropathology. Consequently, the pixel intensities were not considered as a reliable resource to estimate a pathological burden.

Visium-SPG cDNA library generation and sequencing

Immediately after slide imaging, each tissue section was permeabilized and processed for cDNA synthesis, amplification, and library construction according to the Visium Spatial Gene Expression User Guide (10x Genomics, Cat# CG000239 Rev B). Prior to the Visium Spatial Transcriptomics assay, Visium Spatial Tissue Optimization experiments were performed to optimize permeabilization conditions using Visium Tissue Optimization Slides (10x Genomics, Cat# 3000394) with reference to Visium Spatial Tissue Optimization User Guide (10x Genomics, Cat# CG000238 Rev A). 12 minutes was determined to be the optimal permeabilization time for all samples (**Figure S1B**). The resulting whole transcriptome Visium libraries were sequenced on Illumina NovaSeq 6000 with S4 200 cycle kit using a loading concentration of 300 pM (read 1: 28 cycles, i7 index: 10 cycles, i5 index: 10, read 2: 90 cycles).

IF image processing and segmentation for Aβ and pTau

We utilized multispectral imaging and spectral unmixing methods to address background staining from autofluorescent molecules such as lipofuscin, which is common in post-mortem human brain tissue (151,152), as well as from interference effects of undissolved precipitates in the RVC, a ribonuclease inhibitor used in the staining protocol. Specifically, we used a similar strategy to our previous study (153) that allowed us to identify and then mask lipofuscin and RVC-related particulate matter from all fluorescence channels (**Figure S2**). Thresholding background interference with this image processing step allowed us to better distinguish Aβ and pTau aggregates. Our workflow was as follows: first, QPTIFF image files were generated from a Vectra Polaris (Akoya Biosciences) slide scanner. An annotation was drawn to outline each entire slide in a given QPTIFF using Phenochart whole slide viewer (Akoya Biosciences). Spectral fingerprints, based on single positive samples, were generated for DAPI, Alexa 488, Alexa 555, Alexa 594, and Alexa 633, then selected to construct an unmixing algorithm. The unmixing algorithm was applied to the annotated region to decompose multi-spectral profiles into spectrally unmixed multi-channel TIFF tiles using inForm automated image analysis software (Akoya Biosciences). Autofluorescence, including lipofuscin, was segregated to an "AF" channel. Using the `InFormStitch()` function from *VistoSeg* (154), individual image tiles were stitched together into a full slide image using the coordinates of each tile that are saved in the filename. This stitched TIFF was split into multi-channel TIFF images containing an individual capture area using the `splitSlide_IF()` function from *VistoSeg*. GFAP and MAP2 staining data was initially planned as part of the study to investigate the local impact of AD on astrocytes and neuronal processes. However, due to the heavily branched and intermingled morphology of these cells, and the confounding particulate matter from RVC, it proved exceedingly challenging to accurately segment their morphological features. While the raw image data is available and shared to the scientific community, analysis of these image channels for quantification of GFAP and MAP2 signals has been excluded from the present study. Therefore, we focused on pathology-containing Aβ and pTau image channels for quantification. We used *dotdotdot* (153) to segment the channel containing DAPI. Due to the particulate matter background staining from RVC, we observed aberrant punctate staining common to multiple channels including Alexa 488 (Aβ), Alexa 555 (pTau), Alexa 594 (GFAP) and Alexa 633 (MAP2), in addition to the AF channel. To take a conservative approach, we masked the confounding fluorescent signals in Alexa 488 and Alexa 555 channels, using those from Alexa 633, Alexa 594, and AF channels (**Figure S2**). We then used individual thresholds based on the intensity histograms of Aβ and pTau to segment regions of interest (ROIs) from their respective fluorescent channels. For example, in tissue samples from Br3880, ROIs smaller than 1500 pixels were dropped from the Aβ channel due to the inability to distinguish small diffuse Aβ plaques from background lipofuscin and particulate RVC. Then we applied a shape filter to the size-thresholded Aβ ROIs, to retain ROIs mostly circular in shape. We then calculated both the number of ROIs per Visium spot (NABeta and NPTau, the N prefix is for number) and the proportion of the Visium spot covered by segmented signal (PABeta and PPTau, the P prefix is for proportion). In the neurotypical control samples, the same image thresholding approach was applied to address nonspecific background staining, and the final segmentations from samples from a neurotypical control were used to set thresholds in the AD samples.

Visium raw data processing and quality control (QC)

FASTQ and image data were pre-processed with the 10x *SpaceRanger* pipeline (version 1.3.0 for Visium-SPG) (155). Outputs of *SpaceRanger*, including the spotcounts matrix, were stored in a *SpatialExperiment* v1.5.3 (156) object (Bioconductor version 3.13) for downstream analysis. Data were filtered to remove genes that were not detected and spots with zero counts. We used *scran* v1.23.1 (Bioconductor version 3.13) (157) to calculate QC metrics, including mitochondrial expression, low library size, and low gene count. Many of the low-quality spots resided in the white matter and/or at the outermost edges near the leptomeninges (**Figure S9A**). Due to their potential pathobiological significance in cortical laminar organization and AD (158–160), we retained these spots in the downstream analyses. However, we excluded 152 edge spots with low library sizes, which were located on the edges of tissue sections. We also manually eliminated 20 Aβ-positive spots that were falsely annotated due to glare artifacts in the Aβ channel (**Figure S9B**). This preprocessing step for spot-level QC filtered out 172 spots, yielding a total of 38,115 spots across the 10 samples for downstream analyses. We performed dimensionality reduction using the *scater* v1.23.1 package (161) to calculate the top 50 PCs followed by using the *Harmony* package v0.1.0 (38) to perform batch-correction across Visium capture areas.

Unsupervised clustering by *BayesSpace*

To study AD-related neuropathology from gray matter, we applied the spatially-aware clustering method *BayesSpace* v1.5.1 (39) to identify anatomical regions in the Visium data that best corresponded to gray matter spanning cortical layers. *BayesSpace* is a Bayesian statistical model that uses the spatial arrangement of Visium spots to borrow information from each spot's neighborhood in order to assign clusters, thereby producing smoother spatial clusters.

To use *BayesSpace* on all samples at once, we arranged all samples into the same plane as recommended for joint clustering analysis https://edward130603.github.io/BayesSpace/articles/joint_clustering.html with a row offset of 100 per sample. We used `spatialCluster()` with default parameters for `q` = 2 up to 28 applied on the 50 batch-corrected dimensions from *Harmony* (38). Note that *BayesSpace* is not guaranteed to result in *k* equal to *q* as it can merge smaller initial clusters (`init.method = "mclust"` by default) into a single spatial cluster. For example, `spatialCluster(q = 28)` resulted in 24 clusters.

Spatial registration of *BayesSpace* clusters to identify a data-driven gray matter

On the batch corrected *SpatialExperiment* object, spots were pseudo-bulked by their *BayesSpace* cluster for q = 2 through 28 and sample id (Visium capture area), using the `aggregateAcrossCells()` function from *scuttle* v1.5.0 (161). Read counts were normalized to log counts using the `calcNormFactors()` function from *edgeR* v3.37.0 (162). `filterByExpr()` from *edgeR* with default parameters was then used to filter genes that were lowly expressed.

Adjusting for age, sex, and diagnosis, differential gene expression across clusters was then performed using the enrichment model as described previously (24). From *spatialLIBD* v1.7.13 (40), `layer_stat_cor()` was used to compute the correlation between the enrichment results of each BayesSpace cluster for each k and the enrichment results available in Supplementary Table 4 from Maynard, Collado-Torres et al (24). The `fetch_data()` function from *spatialLIBD* (40) was used to retrieve this reference dataset. These correlation results were visualized as a heatmap using the `layer_stat_cor_plot()` function.

Spot-level identification and annotation of heavy-burden AD-related neuropathology

To identify Visium spots with a heavy pathological burden of Aβ and/or pTau for downstream analyses, the pathological burden was measured and thresholded at the spot level, using Aβ and pTau signals, which were quantified by the number (N) of their ROI objects and proportion (P) of pixels covering the ROIs within a spot, respectively. The 99.9th percentile values of NAbeta and PAbeta in samples V10A27004_A1_Br3874 and V10T31036_A1_Br3874, which are both control tissue samples, were identified as Aβ thresholds. As pTau thresholds, the maximum values of NpTau and PpTau in the control samples were identified. Thus, spots with a higher number of Aβ ROI objects (NAbeta) than 1 or a greater proportion of Aβ pixel spot coverage (PAbeta) than 0.108 were labeled to have significant Aβ pathology. Spots with a higher number of pTau ROI objects (NpTau) than 8 or a greater proportion of pTau pixel

spot coverage (PpTau) than 0.0143 were identified as having significant pTau pathology. The `.find_neighbors()` internal function in *BayesSpace* v1.6.0 was used to identify neighboring spots to each pathology spot and were further characterized based on whether they were only adjacent to an 1) Aβ spot, 2) pTau spot or 3) 'both' spot.

Differential gene expression analysis and modeling on gray-matter spots

Spots from *BayesSpace* `q = 2` corresponding to cluster 2, which are the white matter spots, were first dropped as well as those from the control donor Br3874. This resulted in 3,874 spots for none; 1,072 for Aβ; 2,284 for next_Aβ; 8,810 for pTau; 3,217 for next_pTau; 727 for both; and 1,102 for next_both. Then `registration_pseudobulk(min_ncells = 15)` from *spatialLIBD* v1.9.18 (40) was used to pseudo-bulk cells of the same sample ID and pathological category resulting in 41 out of the possible 49 (7 samples x 7 pathological categories) pseudo-bulked samples passing the `min_ncells = 15` filter. Next, `filterByExprs()`, `cpm()`, and `calculateNormFactors()` from *edgeR* (162,163) were used to filter out lowly expressed genes and log-normalize counts resulting in 8,443 genes passing these filters. We then identified differentially expressed genes using three models, as in our previous work (24), using new *spatialLIBD* (40) functions with the `registration_*()` prefix. Given the limited variability across donors, we did not adjust for any covariates. For example, sex is perfectly confounded with sample Br3880 as the other two AD cases are females. First, the ANOVA model used `registration_stats_anova()` from *spatialLIBD* and powered by *limma* (164) to test for differences in mean expression across the 7 pathological categories and found no DEGs (FDR<0.05). Second, the enrichment model used `registration_stats_enrichment()` from *spatialLIBD* to test for differences in expression between one pathological categories versus the remaining six and identified unique 1,840 genes that are DEGs (FDR<0.05) for at least one pathological category. These genes can be either enriched (t>0) or depleted (t<0). See **Table S2** for the Aβ results and **Table S3** for the next_Aβ results. Third, the pairwise model used `registration_stats_pairwise()` from *spatialLIBD* to test for DEGs between each pair of pathological categories (21 pairs total) resulting in 98 unique genes having significant differences (FDR<0.05) in at least one pair. See https://github.com/LieberInstitute/Visium_SPG_AD/blob/master/code/05_deploy_app_wholegenome/Visium_SPG_AD_wholegenome_model_results_FDR5perc.csv for the full results. *EnhancedVolcano* v1.16.0 (165) was used to make the volcano plots for the enrichment model results comparing the log2 fold change against the *p*-values, with a FDR<0.1 cutoff line.

Differential gene expression analysis and modeling on gray-matter spots for the Aβ microenvironment

Similar to the previous analysis, we re-categorized the Aβ and next_Aβ spots as "Aβ_env". We then performed the same type of analysis using functions from *spatialLIBD* (40). With this analysis only one gene was significant (FDR<0.5) for the *anova* model: *TMEM163.* There were 287 DEGs for the *enrichment* model and 15 unique DEGs for the *pairwise* model (FDR<0.5). See **Table S4** for the Aβ_env results or https://github.com/LieberInstitute/Visium_SPG_AD/blob/master/code/18_deploy_app_wholegenome_Abeta_microenv/Visium_SPG_AD_wholegenome_model_results_FDR5perc.csv for the full results. 275 out of the 287 *enrichment* DEGs corresponded to the Aβ_env, with 265 of them depleted (t<0) and 10 of them enriched (t>0). We used `compareCluster(pvalueCutoff = 0.3, qvalueCutoff = 0.3)` with `enrichGO()` and `enrichKEGG()` from *clusterProfiler* v4.6.2 (166) with the Aβ_env enrichment DEGs. While GO terms and KEGG pathways were not significantly enriched (FDR<0.5), enriched (t>0) Aβ_env genes *CYP1B1*, *TNFRSF1A, ZNF385A*, and *RIOK3* were most frequently associated with GO terms.

Statistics and reproducibility

Statistical tests were performed with R version 4.2 with Bioconductor versions 3.13, 3.14, 3.15, and 3.16.0. In addition to software versions listed in the Methods, R session information was recorded with `sessioninfo::session_info()` for many specific analyses on log files or scripts themselves and is available on GitHub and Zenodo (Data and materials availability).

MAGMA

Version (v1.10) of Multi-marker Analysis of GenoMic Annotation (MAGMA) (61) was used to measure genetic risk association of spots containing Aβ plaques and neighbored Aβ plaques, representing the core (Aβ) and periphery (next_Aβ) of Aβ-associated microenvironments, with Alzheimer's disease (AD: Jansen et al. (62)); Frontal Temporal Disorder (Ferrari et al. (63)); and Parkinson's Disease (PD: Nalls et al. (64)). Genes identified as either significantly enriched or depleted based on the Benjamini & Hochberg procedure with a FDR<0.1 (167) were used to create the marker gene sets for each pathology type. We used MAGMA to first annotate SNPs to genes, with window sizes of 10kb to +35kb for each gene. The 1000 Genomes EUR reference panel was used for this step (168). Next, gene-level analyses were performed using the summary statistics provided from the above-mentioned GWAS studies. In the MAGMA software, we used the `snp-wise = mean` model to test whether any of the genes were enriched for genetic risk for each of the GWAS diseases. Finally, competitive gene set analysis was performed with the marker gene sets for Aβ and n_Aβ categories to test whether they are related to the GWAS diseases (**Figure S13A**).

Gene set enrichment analysis

Grubman et al (66) reported a list of differentially expressed genes that overlaps between their findings and those of Mathys et al (136) for each cell type from AD samples. For genes with a reported FDR<0.1, we performed an enrichment analysis using Aβ and n_Aβ categories with *spatialLIBD* v1.11.12 `gene_set_enrichment()` (40) (**Figure S13C**). We performed the same enrichment analysis on differentially expressed genes for AD on bulk RNA-seq reported by Mostafavi et al (65) (**Figure S13B**).

RNAscope smFISH combined with immunofluorescence (FISH-IF) for RNA-protein co-detection

An independent brain donor diagnosed with AD was added to the cohort for this experiment (**Figure 3A** and **Table S1**), and 1 tissue slice from ITC for each of the 4 AD donors was prepared and assayed with the same monoclonal Aβ antibody (6E10) and commercially available RNAscope probes for the genes of interests. In detail, frozen tissue blocks from each of the 4 AD subjects were sectioned at 10 micron thickness (Leica, CM3050s) and stored at −80°C. In Situ Hybridization (ISH) assays were performed with RNAscope technology utilizing the RNAscope Fluorescent Multiplex Kit v.2, 4-plex Ancillary Kit, and RNA-Protein co-detection ancillary kit (Advanced Cell Diagnostics ACD, Cat# 323100, 323120, and 323180) in reference to the manufacturer's instructions: Multiplex Fluorescent Reagent Kit v2 User Manual (ACD, 323100-USM) and RNAscope® Multiplex Fluorescent v2 Assay combined with Immunofluorescence - Integrated Co-Detection Workflow (ACD, MK 51-150 Rev A, Appendix C). Tissue sections were fixed with pre-chilled 10% neutral buffered formalin solution (Sigma-Aldrich, Cat# HT501128) for 15 minutes at 4°C, dehydrated in increasing concentrations of ethanol (50%, 70%, 100%, and 100%), and pretreated with hydrogen peroxide for 10 minutes at room temperature (RT). Sections were incubated with the mouse anti-β-amyloid antibody, clone 6E10 (Biolegend, Cat# 803001, 1:50) overnight at 4°C. After primary antibody incubation, sections were fixed in 10% neutral buffered formalin solution for 30 minutes at RT and treated with protease IV for 30 minutes at RT. The following RNAscope probes were used for in ISH reaction: *PPP3CA*, *UCHL1*, *SST*, *C3*, *IDI1*, and *NINJ1 (*ACD*,* Cat# 477311, 594281-C2, 310591-C3, 485641, 430701-C2, and 540051-C3, respectively, 1x dilution for *PPP3CA* and *C3*, and 1:50 (50x) for *UCHL1*, *SST*, *IDI1*, and *NINJ1*). The 6 probes were grouped into 2 combinations and multiplexed to

co-label 1) *PPP3CA*, *UCHL1*, and *SST* and 2) *C3*, *IDI1*, and *NINJ1* within each tissue sample. After probe labeling, sections were subjected to amplification steps (AMP1–3) and conjugation to fluorescent Opal dyes 570, 620, and 690 (Akoya Biosciences, Cat# FP1488001KT, FP1495001KT, and FP1497001KT, respectively, 1:600-1:2500). At the end of RNAscope procedures, sections were treated with donkey anti-mouse IgG conjugated to Alexa 488 (Thermofisher, Cat# A-21202, 1:400) for 40 minutes at RT and stained with the DAPI solution provided in the RNAscope multiplex kit for counter nuclear staining. The slides were then coverslipped with Fluoromount G (Southern Biotechnology, Cat# 0100-01) and imaged on Vectra Polaris with a MOTiF™ scanning mode. The resulting QPTIFF images were annotated, spectrally unmixed, and fused to recreate an entire slide image using Phenochart (Akoya Biosciences), inForm (Akoya Biosciences), and HALO® image analysis platform (Indica labs), respectively.

RNAscope quantification and spatial proximity analysis using HALO

Prior to segmentation, each tissue section was manually annotated to define a gray matter region based on enrichment of Aβ plaques and to exclude problematic areas such as smeared signals and tissue tears found on the edges. The FISH-IF module and proximity analysis module (version 2.1.5) in HALO were utilized to assess the gene expression changes of genes of interest (GOIs) in the proximity of nearby Aβ plaques with reference to the manufacturer's guidelines: HALO 3.3 FISH-IF Step-by-Step guide (Indica labs, Version 2.1.4 July 2021) and Digital Quantitative RNAscope Image Analysis Guide (Indica labs). For segmentation of extracellular Aβ plaques, the FISH-IF module was optimized to treat Aβ as a nuclear and cellular marker. This process required a paralleled FISH-IF segmentation to analyze cells expressing and not expressing GOIs, independent of the Aβ segmentation (**Figure S15C**). For a given tissue section, therefore, two FISH-IF datasets were generated, one for Aβ and another for GOIs, which we combined to map the segmented objects back to the identical tissue sections (**Figure S15A**). Segmentation was optimized for each object, including Aβ and RNAscope signals for *PPP3CA, UCHL1, SST, C3, IDI1,* and *NINJ1*, using user-defined size and intensity thresholds. A thorough visual inspection was performed to ensure that the segmentation outputs matched the input raw images in terms of object size and shape. The same thresholds were applied to a given GOI across all tissue samples, regardless of the donors. The size thresholds for nucleus and cytoplasm as well as those for Aβ plaques remained constant. Only the copy intensity parameter was adjusted by individual tissue sections to address staining variations between samples, using their average cell intensity of RNAscope signals.

The two datasets of Aβ and GOIs from each tissue section were subjected to downstream proximity analysis to measure the distance between the segmented Aβ and cells expressing and not expressing GOIs, namely GOI- and non-expressors. Based on their proximity to the nearby Aβ, the GOI- and non-expressors were classified into the following 7 intervals: 1) 0-21.25μm, 2) 21.25-42.5μm, 3) 42.5-63.75μm, 4) 63.75-85μm, 5) 85-106.25μm, 6) 106.25-127.5μm, and 7) >127.5μm. The spatially categorized cells from the proximity analysis were then aligned with the complementary FISH-IF dataset for the GOI expressors and non-expressors and assigned their corresponding RNAscope puncta counts, using their unique cell identifier (ID) numbers. The puncta counts were then summed up to compute the average single cell gene expression in each interval. Normalization was implemented with the total number of GOI expressors per interval. For the spatially down-regulated and/or depleted genes identified from the Visium assays, we normalized their gene expression by the total number of cells existing in each sub-region. We summed the GOI expressors and non-expressors and used the value as a denominator to account for the reduction in gene expression driven by not only downregulation of GOIs within the same cell, but also the complete absence of GOI expressors in a defined sub-area. The latter was more pronounced with genes whose expression was sparsely distributed, such as *SST*. This normalization approach aided in the interpretation of the spatial gradients of several GOIs with statistical significance (**Figure S16A-B)**. A log2 (X+1) transformation was implemented, where X is the raw puncta count, to account for the skewed cellular distribution as well as the non-expressors with zero puncta (**Figure S16C**). Quantification plots and statistical testings for the non-parametric Kruskal-Wallis test were made with Prism (version 9).

Data and materials availability

The source data are also publicly available from the Globus endpoint 'jhpce#Visium_SPG_AD' that is also listed at http://research.libd.org/globus. The raw data provided through Globus includes all the FASTQ files and raw image files. The FISH-IF and proximity data, as well as the segmentation settings, were exported as text files and are available on the raw data directory named AD_RsFISHIF_RawData. Processed data are publicly available from the Bioconductor package *spatialLIBD* version 1.11.12 (40) through the `fetch_data()` function. All source code is publicly available through GitHub and permanently archived through Zenodo at https://github.com/LieberInstitute/Visium_SPG_AD (169). Interactive websites are powered by *spatialLIBD* (40), *iSEE* (170), and *samui* (171).

Acknowledgements

We acknowledge Louise A. Huuki-Myers, Boyi Guo, Matthew N. Tran, Svitlana Bach, and Ryan A. Miller for their insightful assistance with statistical testing, MAGMA analyses, data interpretation, and data transfers respectively. They were all employed by the Lieber Institute for Brain Development (LIBD) except for Boyi Guo from the Johns Hopkins Bloomberg School of Public Health, Department of Biostatistics. We acknowledge Elizabeth Engle and the Johns Hopkins Tumor Microenvironment Lab core facility for assistance with the Vectra Polaris slide scanner. We would like to thank the Joint High Performance Computing Exchange (JHPCE) for providing computing resources for these analyses. We thank Amy Deep-Soboslay and James Tooke from LIBD for curation of brain samples and assistance with coordinating dissections. We also thank the office of the County of Santa Clara Medical Examiner-Coroner Office in San Jose, CA and the Western Michigan University Homer Stryker MD School of Medicine, Department of Pathology in Kalamazoo for making post-mortem human tissue donations possible to advance these studies. We are indebted to the generosity of families of brain donors for supporting this research. Finally, we thank the families of Connie and Stephen Lieber and Milton and Tamar Maltz for their generous support of this work. Schematic illustrations were generated using Biorender.

Author contributions

Conceptualization: KM, KRM
Methodology: KM, KRM, LCT, SHK, MT, SP
Software: LCT, MT, SP, HRD, NJE
Validation: SHK, JSL
Formal analysis: SHK, MT, LCT, SP
Investigation: SHK, MT, LCT, SP, JSL
Resources: TMH, JEK, RAB, SRW, MM
Data curation: SHK, LCT, SP, MT
Writing-original draft: SHK, MT, SP, LCT

Writing-review and editing: KM, KRM, SCP, SCH, LCT
Visualization: SHK, LCT, SP
Supervision: KM, KRM, LCT, SCP, SCH
Project administration: KM, KRM
Funding acquisition: KM, KRM

Author disclosure statement

SW and MM are employees of 10x Genomics. All other authors declare no conflicts of interest.

Funding statement

Funding for these studies was provided by the Lieber Institute for Brain Development (LIBD) and 10x Genomics.

Figure legends

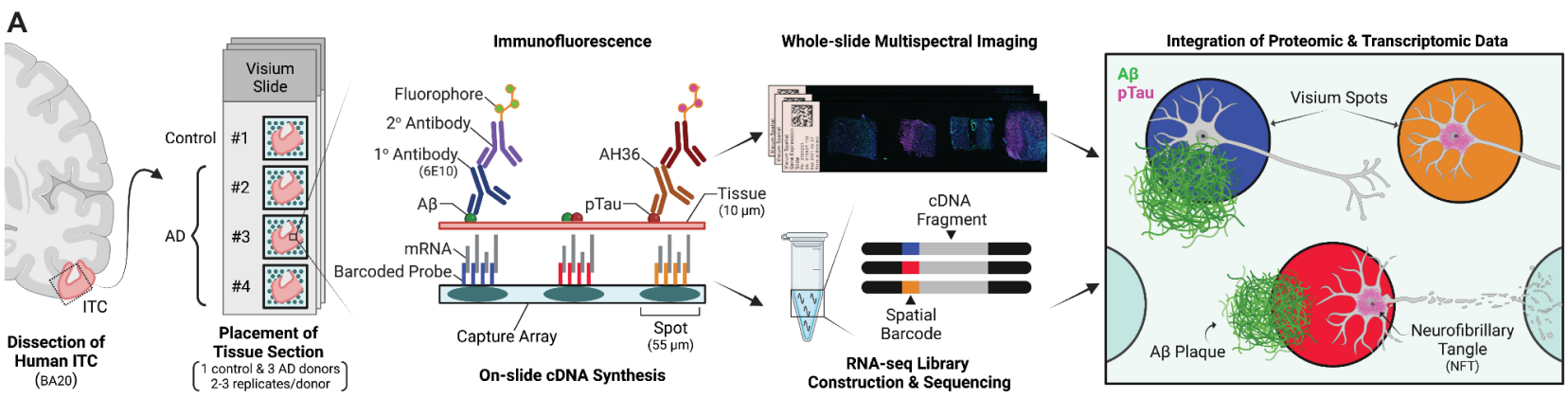

Fig.1 Spatial transcriptomics combined with immunodetection of Aβ and pTau in the human inferior temporal cortex (ITC).

(**A**) Schematic of experimental design using Visium Spatial Proteogenomics (Visium-SPG) to investigate the impact of Aβ and pTau aggregates on the local microenvironment transcriptome in the post-mortem human brain. Human ITC blocks were acquired from 3 donors with AD and 1 age-matched neurotypical control. Tissue blocks were cryosectioned at 10µm to obtain 2-3 replicates per donor and sections were collected onto individual capture arrays of a Visium spatial gene expression slide, yielding a total of 3 gene expression experiments. The entire slide (4 tissue sections) was stained and scanned using multispectral imaging methods to detect Aβ and pTau immunofluorescence (IF) signals as well as autofluorescence. Following imaging, tissue sections were permeabilized and subjected to on-slide cDNA synthesis after which libraries were generated and sequenced. Transcriptomic data was aligned with the respective IF image data to generate gene expression maps of the local transcriptome with respect to Aβ plaques and pTau elements, including neurofibrillary tangles. (**B**) High magnification images show Aβ plaques (white triangles) and various neurofibrillary elements such as tangles (white arrowheads), neuropil threads (red arrowheads), and neuritic tau plaques (yellow arrowheads). Lipofuscin (cyan) was identified through spectral unmixing and pixels confounded with this autofluorescent signal were excluded from analysis, scale bar, 20µm. (**C**) ITC tissue block from Br3880 (left) and corresponding spotplots (right) from the Visium data show gene expression of *MOBP* and *SNAP25,* which demarcates the border between gray matter (GM) and white matter (WM), scale bar, 1mm. Color scale indicates spot-level gene expression in logcounts. (**D**) Image processing and quantification of Aβ and pTau per Visium spot. Aβ and pTau signals were thresholded in their single IF channels for segmentation against autofluorescence background, including lipofuscin. Thresholded Aβ and pTau signals were aligned to the gene expression map of the same tissue section from Br3880 and quantified as the proportion of number of pixels per Visium spot, which is visualized in a spotplot, scale bar, 1mm.

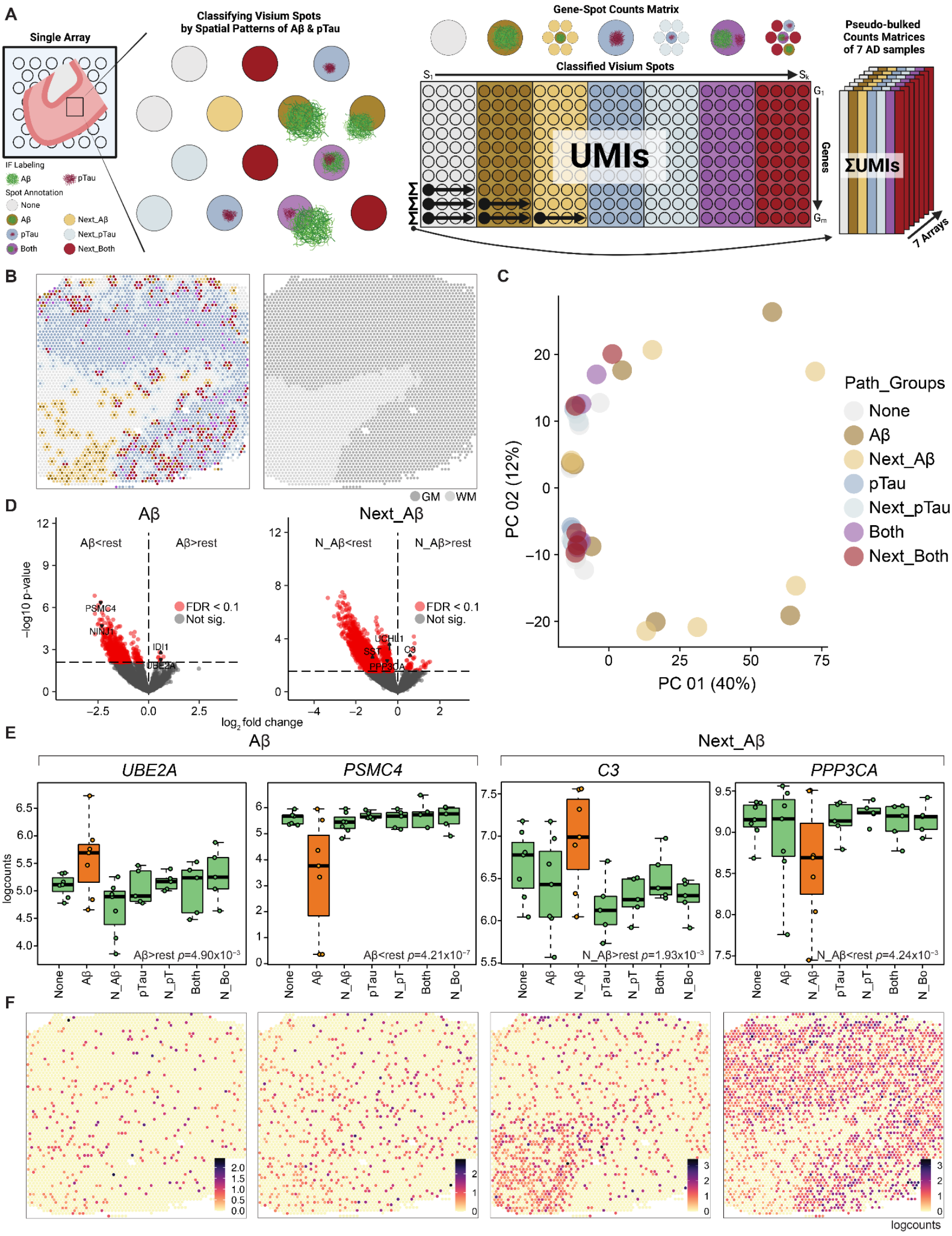

Fig.2 Identification of transcriptomic signatures in local microenvironments harboring AD-related neuropathology.

(**A**) Graphical overview of spot-level annotation for AD-related neuropathology (left), and strategy for pseudo-bulking annotated spots (right). Aβ and pTau labeling was quantified in individual spots, which were subsequently annotated accordingly to reconstruct spatial heterogeneity of pathology according to the following hierarchy: spots containing both Aβ and pTau (purple), Aβ pathology (brown), pTau pathology (blue), and then spots adjacent to both Aβ and pTau (red), Aβ pathology (light brown), and pTau pathology (light blue). Spots with no significant Aβ and pTau deposition were labeled white. Annotated spots were then collapsed into the 7 pathological categories in a gene x spot matrix for each tissue sample. Unique molecular identifier (UMI) counts for each gene were pseudo-bulked within an individual pathological category across the 7 replicate arrays from 3 AD donors to yield 49 pathology-enriched gene expression profiles. (**B**) Spotplot for Br3880 showing spot-level annotation of AD-related neuropathology (left) and unsupervised clustering of spots using *BayesSpace* (right). Spots associated with pathology were aggregated within gray matter (GM; dark gray), which was identified using an unsupervised clustering approach, as in **Figure S11A**. Any pathology-associated spots in the white matter (WM; light gray) were not included in downstream analyses. (**C**) PCA was performed on the 41 pseudo-bulked gene expression profiles across the 7 spatial categories of AD-related neuropathology. PC1 separated the Aβ and next_Aβ spots from the other pathological categories. (**D**) Volcano plots depicting differentially expressed genes (DEGs) between Aβ pathology (Aβ) or adjacent Aβ pathology (Next_Aβ) versus the rest of pathological categories. Each dot represents a gene, plotted with its log2 fold change (x-axis) and -log10 *p*-value (y-axis), thus comparing the effect size (fold change) against the statistical evidence for differential expression (*p*-value). The dashed line represents a *p*-value threshold matching FDR<0.1, with DEGs below the line considered not significant (gray, Not sig.) Significant DEGs that passed the FDR threshold were labeled red and classified by their enrichment (>rest) and depletion (<rest) in gene expression according to the 'enrichment' model. (**E**) Boxplots of DEGs in Aβ pathology spots (*UBE2A* and *PSMC4)* and adjacent Aβ pathology spots (*C3* and *PPP3CA)* depicted in orange across all samples, compared to all other pathological categories depicted in green. For brevity, 'Next' was shortened to N. (**F**) Corresponding spotplots of *UBE2A*, *PSMC4*, *C3*, and *PPP3CA* for Br3880 showing spatial distribution of each DEGs. Color scale indicates spot-level gene expression in logcounts.

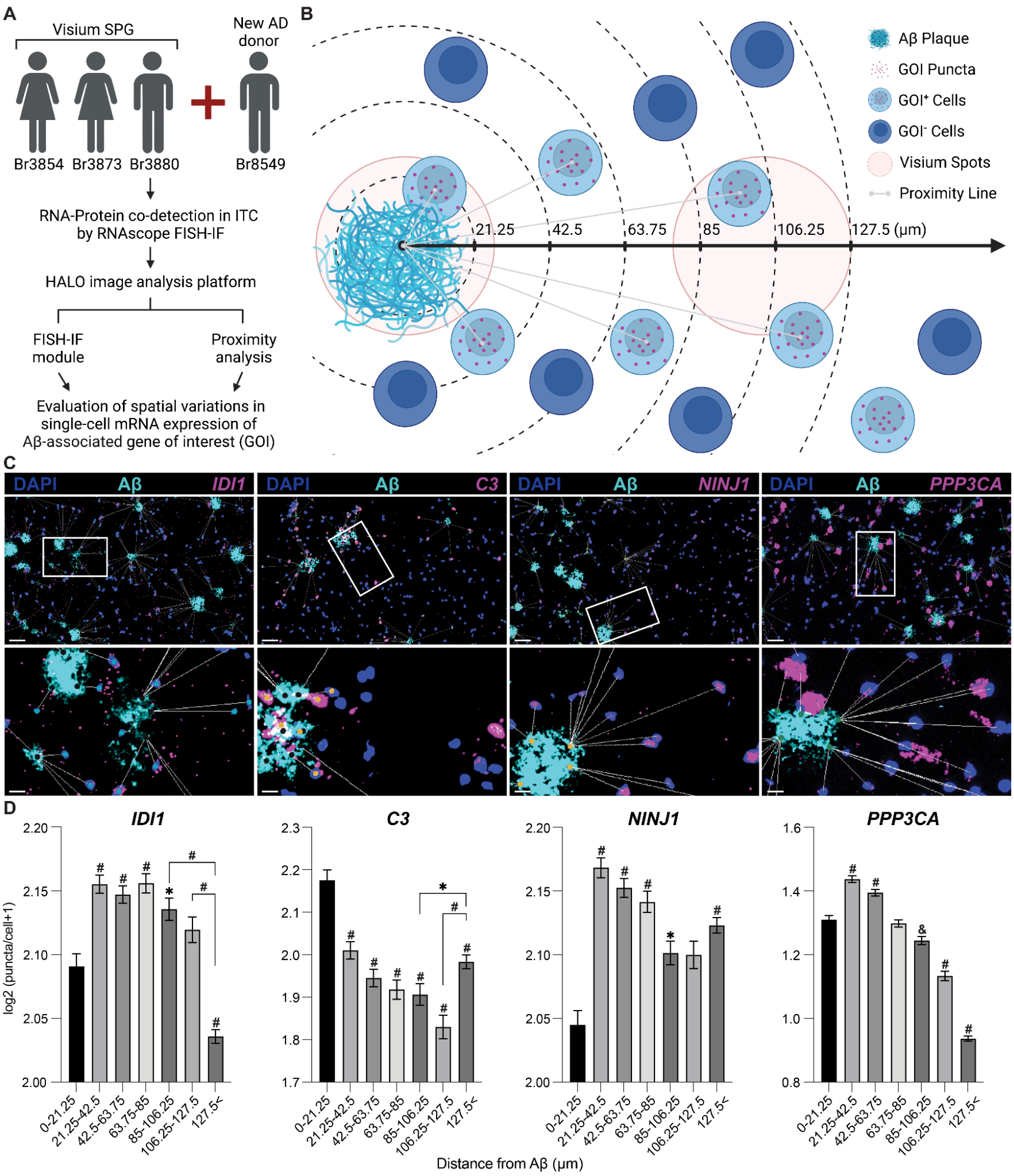

Fig.3 Characterization of Aβ-associated transcriptional signatures at cellular resolution.

(**A**) Flowchart of experimental design and data analysis. Human ITC tissues from 3 original AD donors plus additional male donor Br8549 were subjected to multiplexed staining using RNAscope smFISH combined with immunofluorescence (FISH-IF) to detect genes of interest (GOIs) and Aβ plaques. Images were analyzed with HALO image analysis software to assess spatial relationships between Aβ and cells expressing GOI. The FISH-IF module of HALO was used for image segmentation and quantification of Aβ and GOIs. The proximity analysis module was used to determine a distance between Aβ and cells expressing or not expressing GOIs. The outputs of the two modules were integrated to measure the gene expression of GOIs within a predefined proximity of Aβ at cellular resolution. (**B**) Schematic describing proximity analysis. An Aβ-associated microenvironment was demarcated by approximating the Visium spot grid-line system in which the center of a single Visium spot is 127.5μm away from its neighboring spot. This distance was further subdivided into 6 evenly spaced intervals, resulting in a total of 7 bins to finely resolve the spatial gene expression gradients of GOIs. The proximity between Aβ and nearby cells expressing and not expressing GOIs was measured and used to classify into the 7 bins for quantifying the average GOI gene expression. (**C**) RNA-protein co-detection of Aβ and *IDI1*, *C3*, *NINJ1*, *PPP3CA* reveals the spatial distribution patterns of Aβ (cyan) and GOIs (magenta) at lower (Top, scale bar: 50μm) and higher magnifications (Bottom, scale bar: 12.5μm). Proximity lines indicate the distance between Aβ and nearby cells expressing GOIs (max: 127.5μm). (**D**) Bar plots show quantification of gene expression levels for GOIs in **Figure 3C** across 7 consecutive bins representing increased distance from Aβ, as modeled in **Figure 3B**. Gene expression levels were determined with log2 (X+1) transformation where X represents the counts of puncta in a single cell for a given GOI. Data are mean ± SEM. The first bin was compared to all the rest by default for statistical tests (Kruskal-Wallis test, $^{*}p<0.05$, $^{\&}p<0.005$, and $^{\#}p<0.0001$). The bracket denotes statistical testing between two specified bins. Violin plots are provided in **Figure S16C** describing the cellular distribution and numbers counted for each bin.

Tables

Supplementary Table S1. Sample donor demographics.

This table summarizes the donor demographic information, clinical diagnosis, tissue sample details, and study design for the spatially-resolved transcriptomics study based on Visium-SPG and RNAscope FISH-IF assays. The information provided includes the demographic and clinical details of the donors selected for the study, the types of assays performed, the number of Visium tissue replicates, and tissue sample identifiers, including slide serial numbers and Visium capture areas.

Supplementary Table S2. DEG statistics for the enrichment model for the Aβ category across the 7 pathological categories.

This supplementary table presents the results of differential expression (DE) testing for Aβ spots (i.e., the 'Aβ' category), based on the enrichment model, using the pseudo-bulked Visium-SPG data. The table includes columns for Ensembl gene ID, gene name (symbol), log2 fold change (logFC), enrichment model *t*-statistic, two sided *p*-value, and FDR-adjusted *p*-value. This table can also be re-downloaded from https://libd.shinyapps.io/Visium_SPG_AD_wholegenome/ under the tabs labeled "layer-level data" and "model box plots".

Supplementary Table S3. DEG statistics for the enrichment model for the next_Aβ category across the 7 pathological categories.

This supplementary table presents the results of differential expression (DE) testing for the Aβ-adjacent spots (i.e., the 'next_Aβ'/'n_Aβ' category), based on the enrichment model, using the pseudo-bulked Visium-SPG data. The table includes columns for Ensembl gene ID, gene name (symbol), log2 fold change (logFC), enrichment model *t*-statistic, two sided *p*-value, and FDR-adjusted *p*-value. This table can also be re-downloaded from https://libd.shinyapps.io/Visium_SPG_AD_wholegenome/ under the tabs labeled "layer-level data" and "model box plots".

Supplementary Table S4. DEG statistics for the enrichment model for the Aβ_env category across the 6 pathological categories, when Aβ and next_Aβ were combined into Aβ_env.

This supplementary table presents the results of differential expression (DE) testing for the combined Aβ and Aβ-adjacent spots (i.e., the 'Aβ microenvironment'/'Aβ_env' category), based on the enrichment model, using the pseudo-bulked Visium-SPG data. The table includes columns for Ensembl gene ID, gene name (symbol), log2 fold change (logFC), enrichment model *t*-statistic, two sided *p*-value, and FDR-adjusted *p*-value. This table can also be re-downloaded from https://libd.shinyapps.io/Visium_SPG_AD_wholegenome_Abeta_microenv/ under the tabs labeled "layer-level data" and "model box plots".

Supplemental information

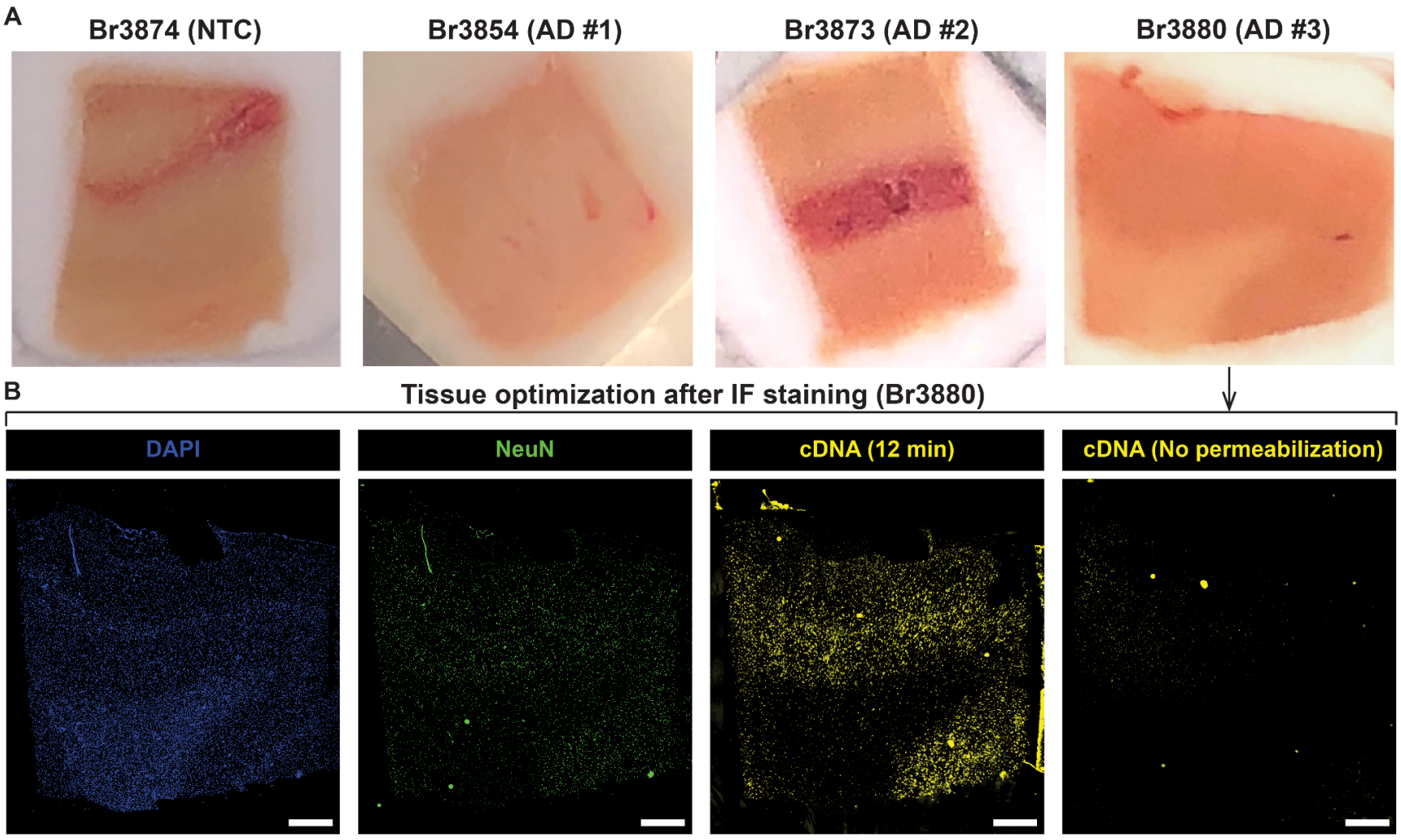

Figure S1. Tissue permeabilization optimization for ITC blocks used for Visium-SPG experiments.

(**A**) Representative images of inferior temporal cortex (ITC) tissue blocks obtained from 1 neurotypical control (NTC) and 3 donors diagnosed with AD that were used for Visium-SPG experiments. (**B**) Representative image from Br3880 of tissue permeabilization optimization experiment. Tissue optimization experiments were conducted to determine the optimal permeabilization time for sufficient cDNA synthesis following immunofluorescence staining. Cryosections from the tissue blocks were immunostained for NeuN and counterstained with DAPI to label the nucleus. After whole-slide imaging, the same cryosections were permeabilized for different time points and subjected to cDNA synthesis with fluorescently labeled nucleotides resulting in a fluorescent cDNA footprint (yellow). The optimal permeabilization time was determined to be 12 minutes, a timepoint at which robust cDNA synthesis was consistently observed across all samples and donors. A non-permeabilized tissue section lacking successful cDNA synthesis shows the baseline fluorescence level. Scale bar, 1mm.

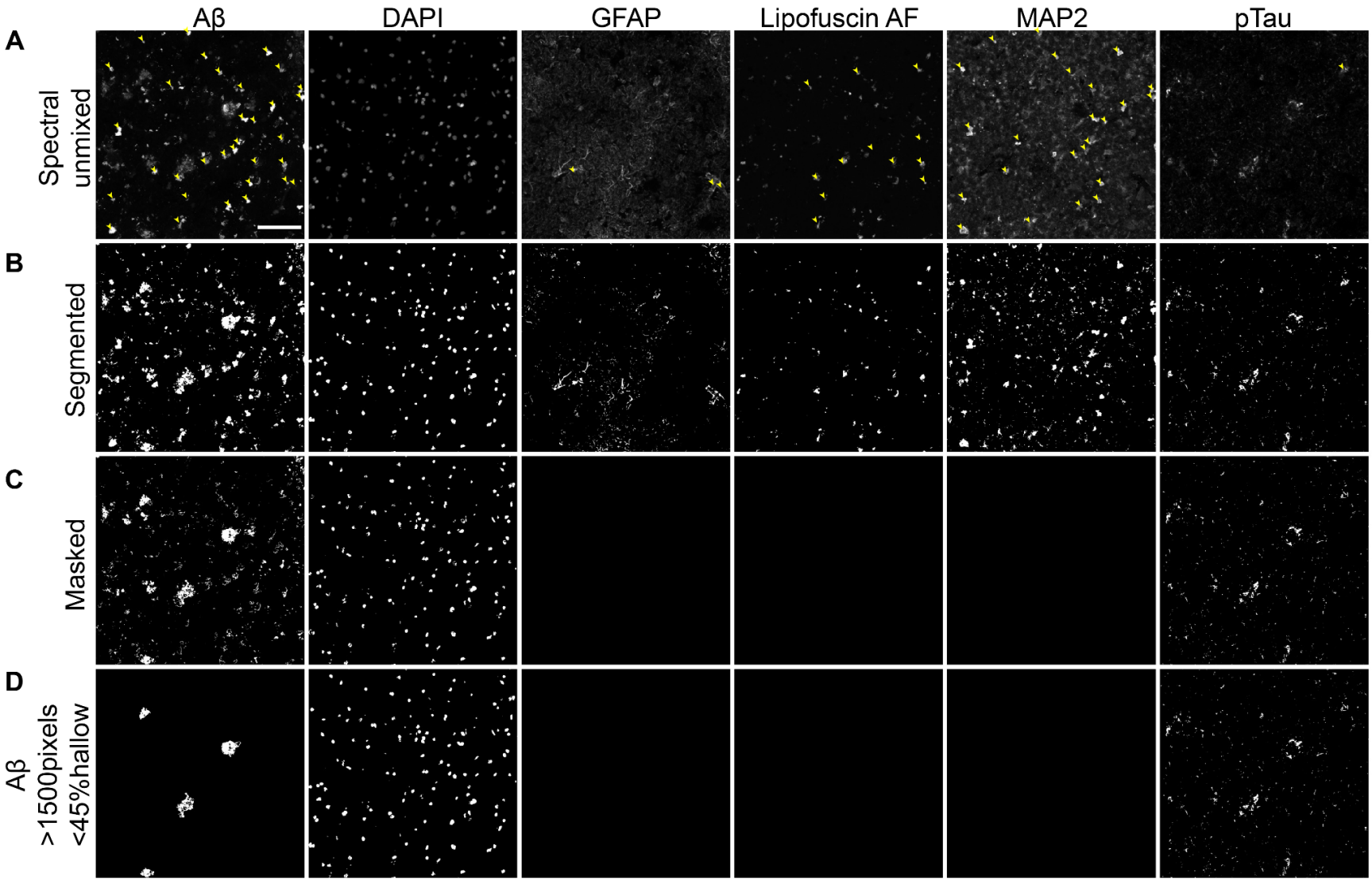

Figure S2. Image processing workflow to threshold background fluorescence and staining artifacts.

High-magnification grayscale images of multichannel IF staining of the gray matter from AD donor Br3880 illustrating the sequence of image processing steps applied to all 6 fluorescence channels. (**A**) After spectral unmixing, residual lipofuscin and particulate matter of ribonucleoside vanadyl complex (RVC), a ribonuclease inhibitor, were observed as background noise and confounding staining artifacts (yellow arrowheads) across multiple channels of the processed IF image including Aβ, GFAP, lipofuscin autofluorescence (AF), MAP2, and pTau. (**B**) All channels were segmented by intensity-based thresholding for each individual channel. (**C**) The segmented objects in the GFAP, AF, and MAP2 channels were used to mask and remove noise and artifacts from all channels. (**D**) The Aβ channel was further thresholded to isolate Aβ plaques using their distinct morphology (4th row, Aβ) based on size (>1500 pixels) and shape (<50% hollow). Detailed descriptions of staining artifacts and image processing workflow were provided in Methods. Scale bar, 100μm.

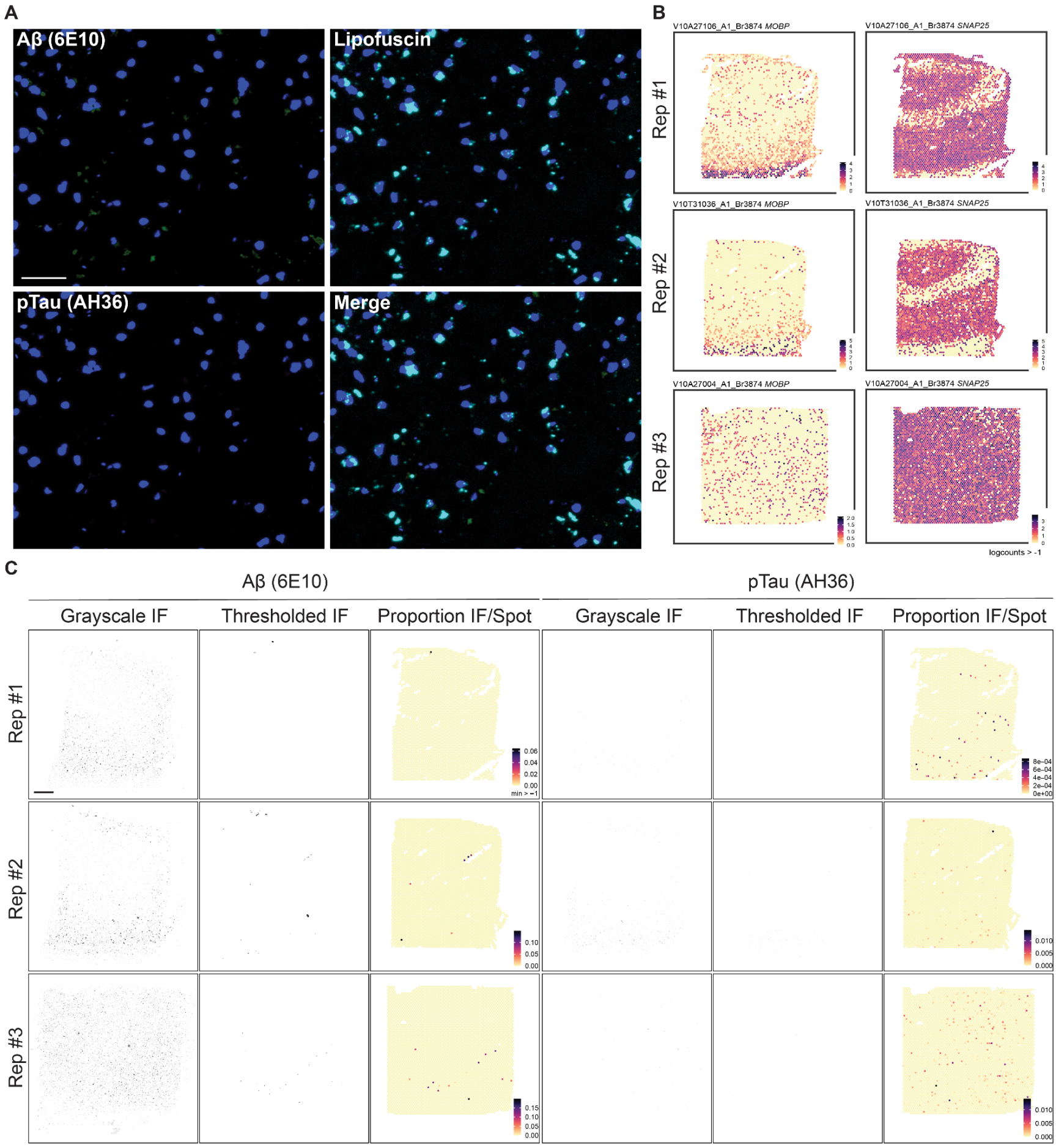

Figure S3. Validation of immunostaining (IF) and image processing workflow using neurotypical control samples.

(**A**) Representative high magnification images of Aβ (6E10), pTau (AH36), and lipofuscin fluorescence in control tissue sections showing little to no AD-related neuropathology in the control donor. Scale bar, 50μm. (**B**) Spotplots of *SNAP25* and *MOBP* across 3 replicate tissue sections from neurotypical control Br3874 showing spatial orientation of gray and white matter, respectively. Replicate 3 (Rep3) was obtained from a different tissue block from the same donor, showing a different tissue-wide morphology. The unclear separation between gray and white matter was noted in this replicate but still included in the downstream analyses for *Harmony*-based batch correction as in **Figure S10**. (**C**) IF image thresholding of Aβ and pTau pathology in control tissue sections and integration with the complementary SRT data. Raw grayscale IF images of Aβ and pTau signals were segmented and thresholded to integrate with complementary spatially resolved spot-level transcriptomes. Thresholded IF images show segmented and thresholded IF signals by size and shape and thus removal of the autofluorescent signals and noise due to lipofuscin and particulate matter of ribonucleoside vanadyl complex (RVC), a ribonuclease inhibitor used in the staining protocol. 6E10 and AH36 refer to clonal names of the monoclonal antibodies raised against Aβ and pTau, respectively. As expected for this control donor, we observed little to no pathology signal on the thresholded IF. Color scale indicates the proportion of Aβ and pTau pixels per Visium spot. Scale bar, 1mm.

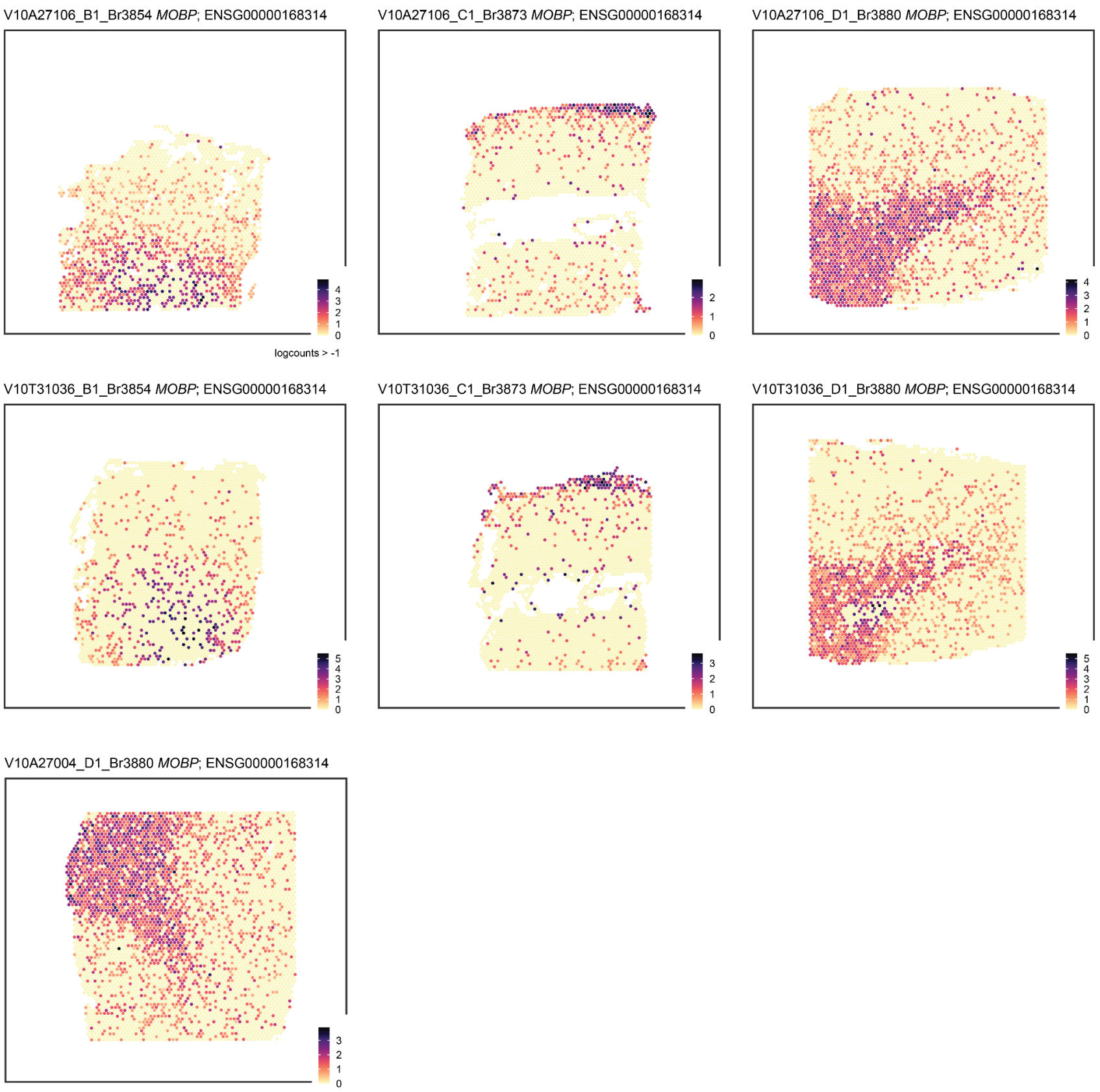

Figure S4. Spotplots of *MOBP* across 7 AD tissue sections from 3 AD donors.

Spot-level gene expression of *MOBP* (myelin-associated oligodendrocyte basic protein) confirms the location of the white matter in each tissue section. Color scale indicates spot-level gene expression in logcounts.

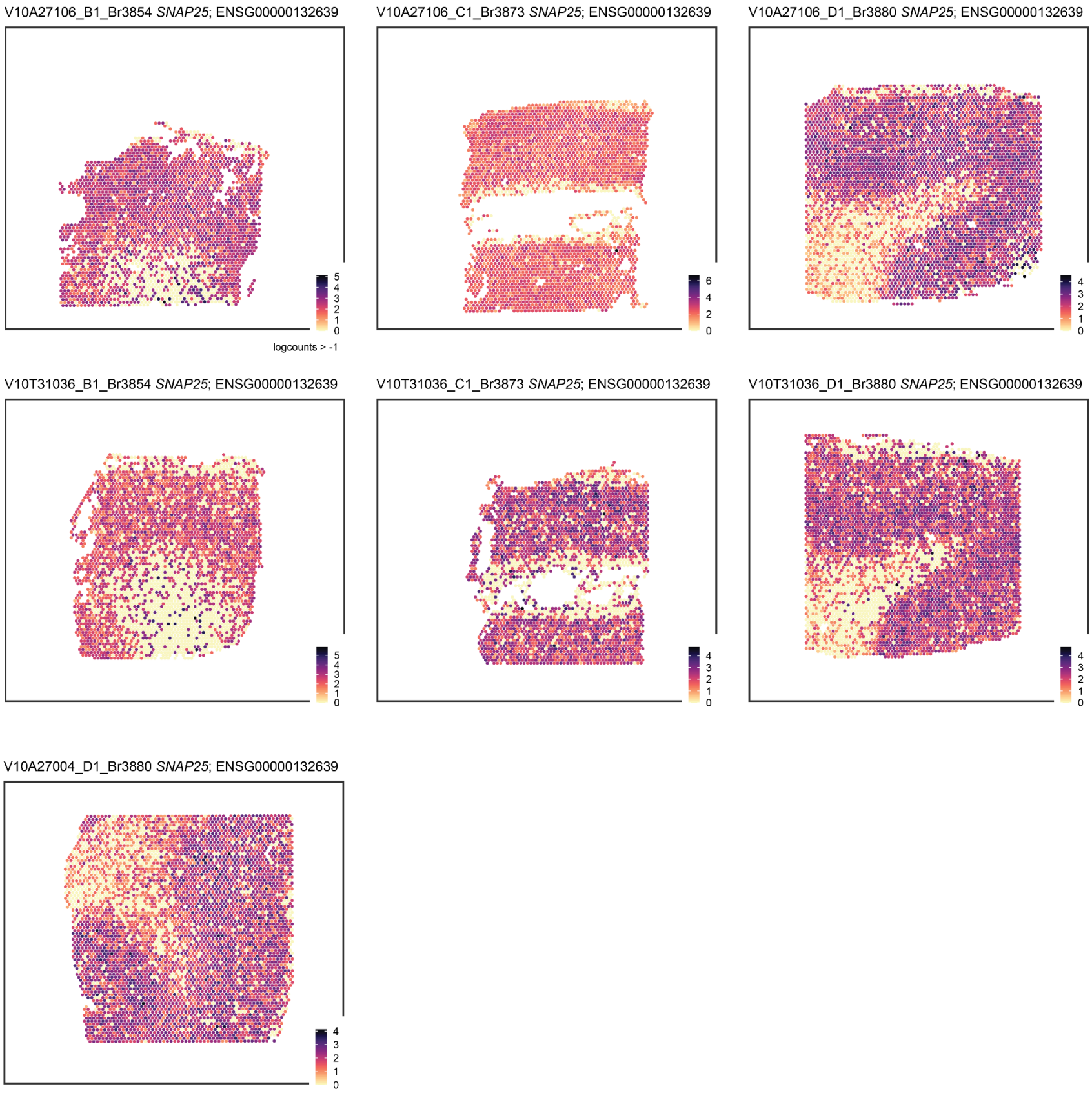

Figure S5. Spotplots of *SNAP25* across 7 AD tissue sections from 3 AD donors.

Spot-level gene expression of the neuronally-enriched gene *SNAP25* (synaptosomal-associated protein 25) confirms the location of the gray matter in each tissue section. Color scale indicates spot-level gene expression in logcounts.

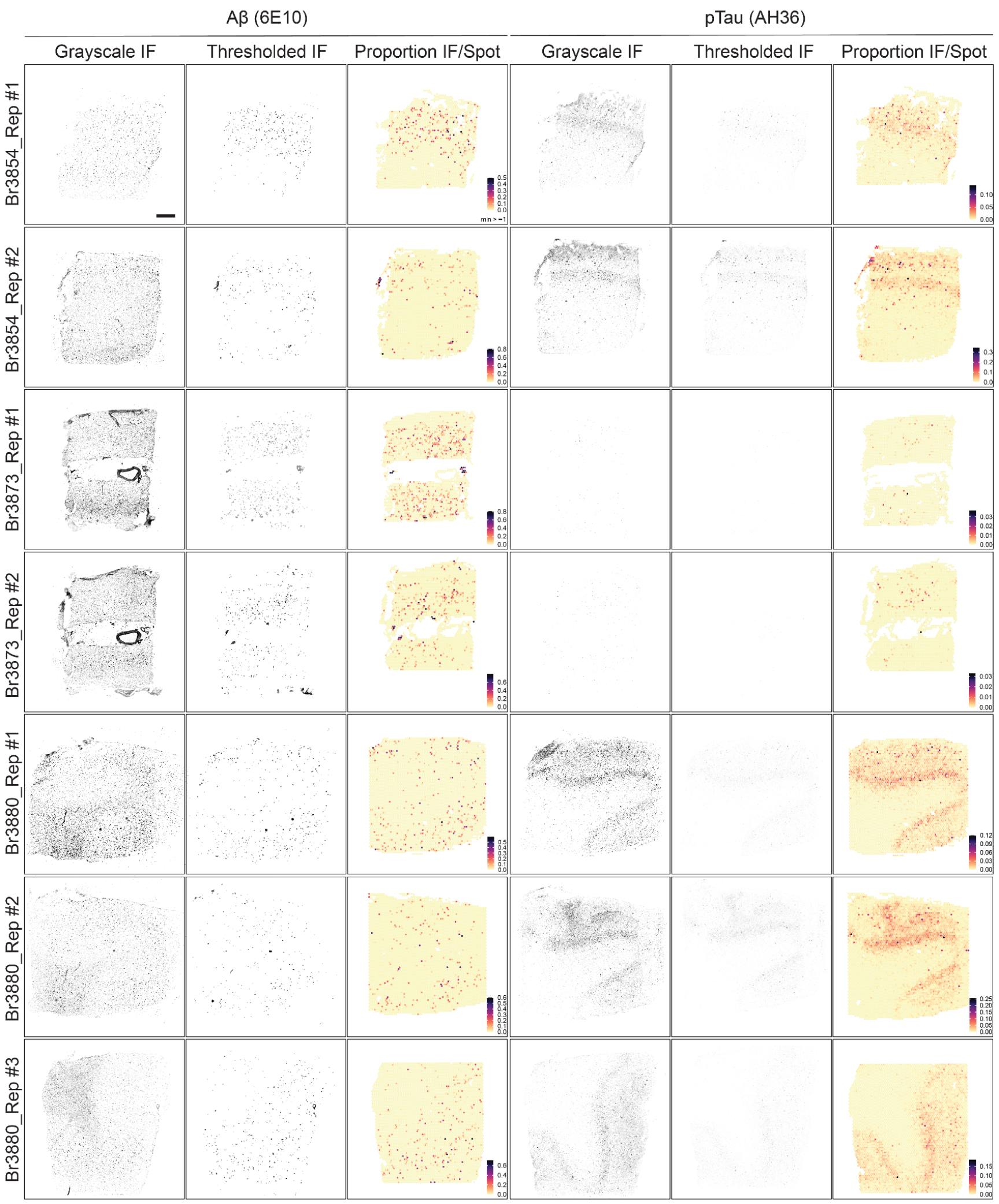

Figure S6. Immunofluorescence image thresholding and integration with spatially-resolved transcriptomics data.

Raw grayscale immunofluorescent (IF) images of Aβ and pTau signals were segmented and thresholded by size and shape to remove autofluorescent signals and noises due to lipofuscin and ribonucleoside vanadyl complex (RVC), a ribonuclease inhibitor used in the staining protocol. 6E10 and AH36 refer to clonal names of the monoclonal antibodies raised against Aβ and pTau, respectively. Thresholded segmentations of image data were then integrated with complementary spatially resolved spot-level transcriptomes (i.e., Visium spots) to construct transcriptome-scale spatial maps of AD-related neuropathology in human ITC tissue sections across 3 AD donors. Color scale indicates the proportion of Aβ and pTau pixels per Visium spot. Scale bar, 1mm.

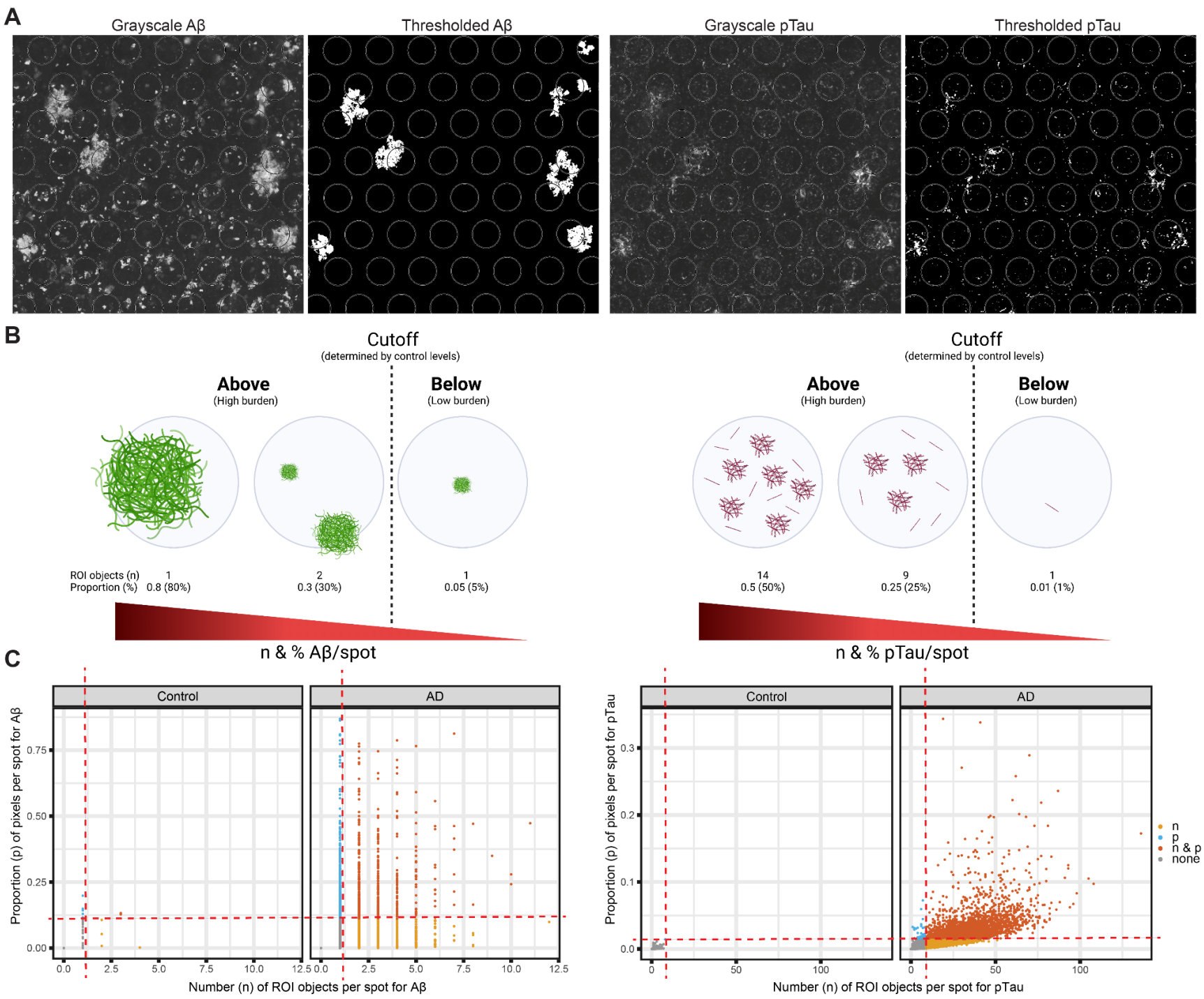

Figure S7. Identification of high-burden Aβ and pTau spots included in downstream analyses.

(**A**) Representative raw grayscale IF and segmented/thresholded images of Aβ (left) and pTau (right) mapped to spot-level transcriptomes on the Visium platform. Diameter of Visium spot, 55µm. (**B**) Schematic cartoon illustrating how AD-related neuropathology was thresholded at the spot level. For individual Aβ (left) and pTau (right) pixels mapped to Visium spots, the number (n) of their region-of-interest (ROI) objects and proportion (p) of their pixels within ROIs were counted per spot. Cut-offs for each pathology were determined based on the values calculated from control tissue sections, which largely lacked pathology and were therefore representative of background signals. Visium spots containing the high pathological burden passing the defined threshold in both metrics (number of objects and proportion of pixels) were included in downstream analyses. (**C**) Distribution of Visium spots bearing varying degrees of AD-related pathology. Visium spots from 3 control (1 neurotypical donor) and 7 AD tissue sections (3 AD donors) were classified separately for Aβ (left) and pTau (right) using two different metrics: the number (n) of ROI objects and proportion (p) of pixels. Two thresholds (red dashed lines) were set with respect to the baseline levels observed in samples V10A27004_A1_Br3874 and V10T31036_A1_Br3874 from the neurotypical control donor. For Aβ, the cut-off values were 1 for (n) and 0.108 for (p); for pTau, 8 for (n) and 0.0143 for (p). Visium spots passing both (orange) or either of the thresholds (yellow and blue) were selected as heavy-burden spots for downstream analyses. Visium spots containing pathology below the thresholds were labeled gray indicating no significant pathology (none).

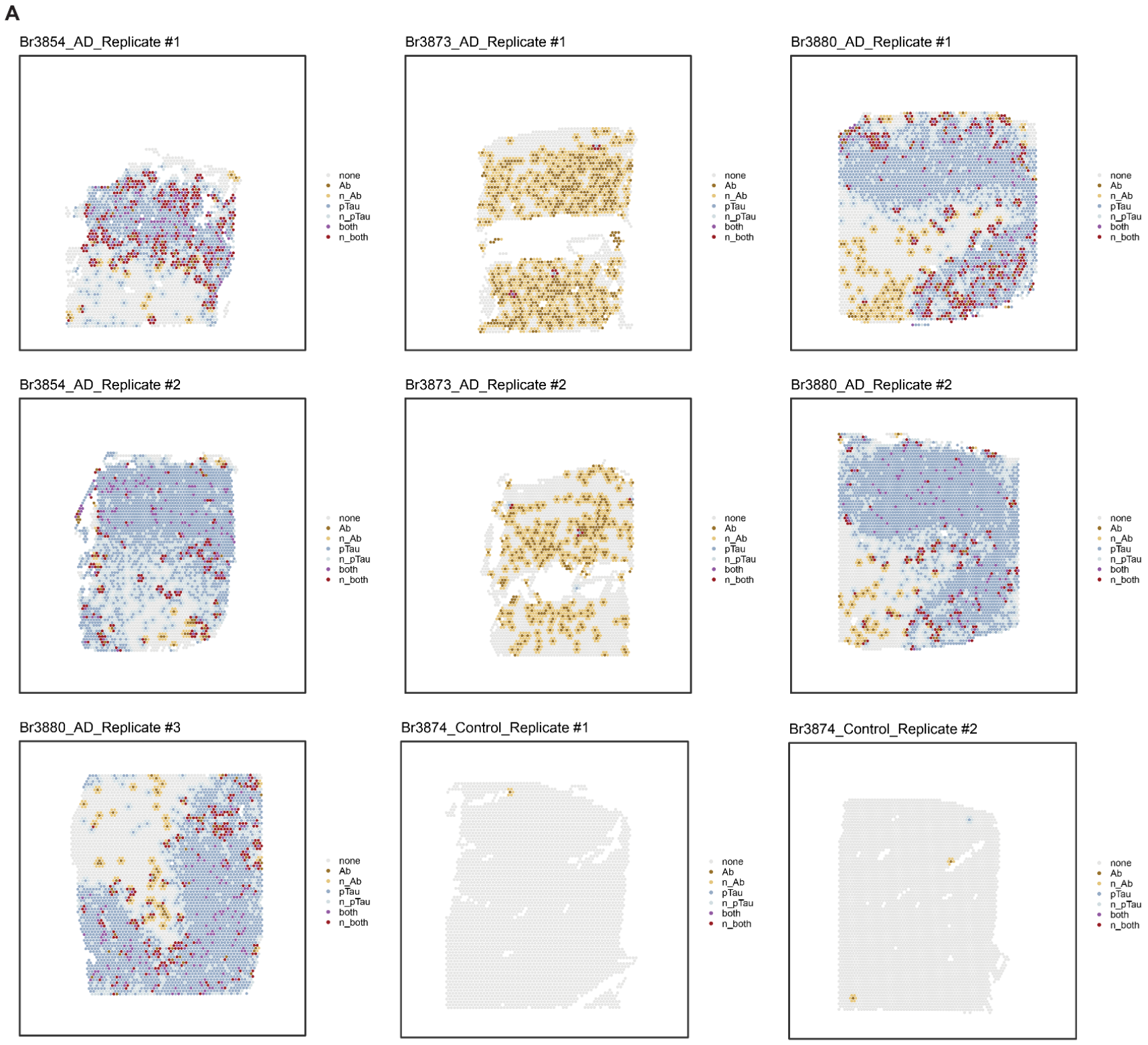

Figure S8. Classification of spots into different AD-related neuropathological categories.

(**A**) Spot-level annotations of AD-related neuropathology across 10 tissue sections. The legend on the right indicates 7 spatial categories of AD-related neuropathology: none for no significant pathology; Ab for Aβ pathology; n_Ab for next to Aβ-containing spots, pTau for pTau pathology; n_pTau for next to pTau-containing spots; both for combined Aβ and pTau pathology; n_both for next to both. (**B**) Composition of annotated Visium spots constituting various spatial patterns of AD-related neuropathology for each AD tissue section across the 7 AD tissue sections used in the downstream analyses. The first column in each sample represents spots residing in the gray matter cluster and the second, the white matter cluster as identified by unsupervised clustering with *BayesSpace*, shown in **Figure S11**.

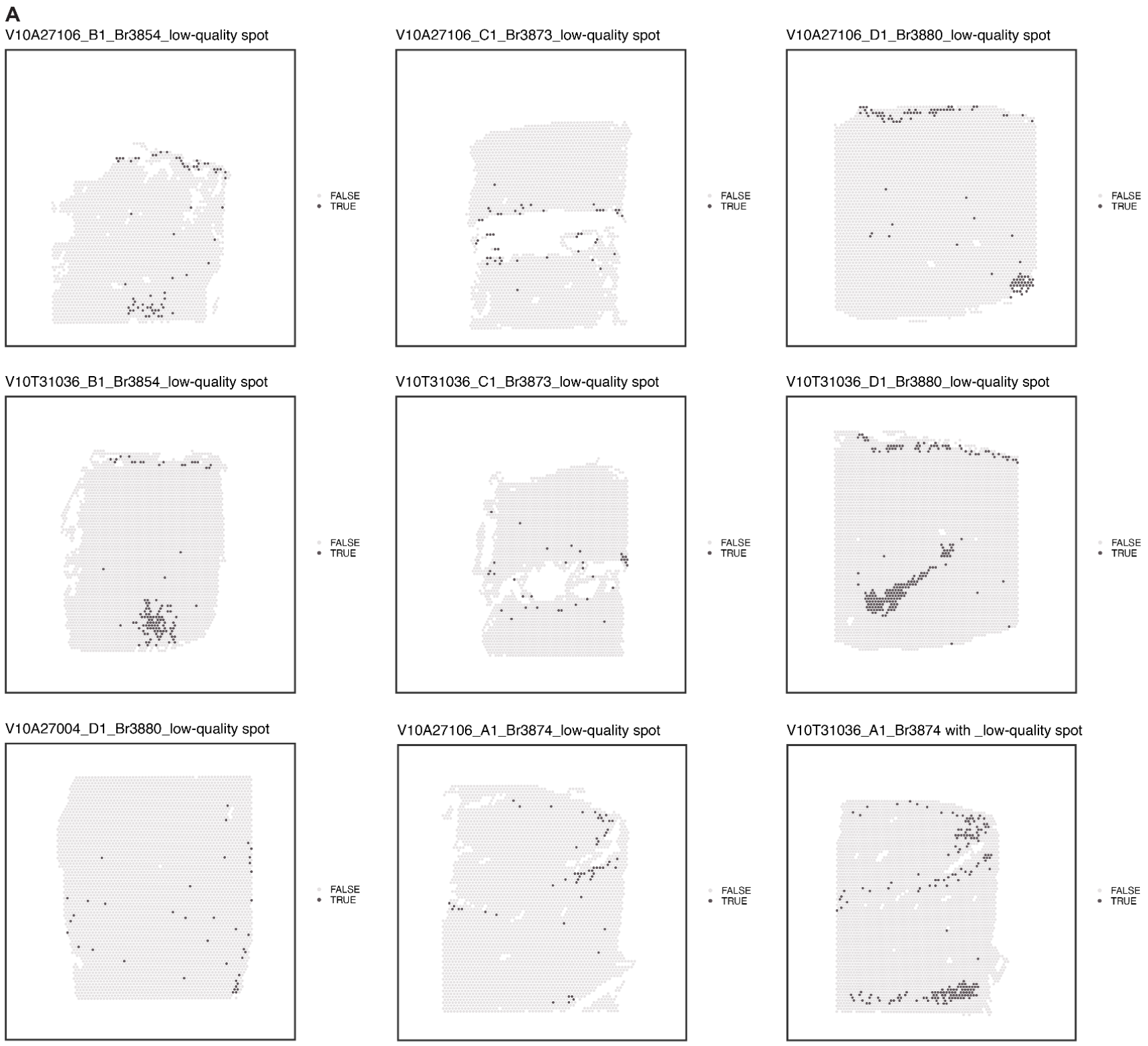

Figure S9. Spot-level quality control of Visium SRT data.

(**A**) Visium spots with low library sizes, low gene expression features, or high mitochondria reads were identified by *scran* for all 10 samples and labeled in dark gray as TRUE. These spots in the 7 AD samples were retained in the downstream analyses due to their biological implication in the laminar organization of AD. (**B**) Manual removal of Visium spots with glare artifacts in the Aβ channel. The raw IF image of a tissue section from Br3880 (left) contains imaging-related glare artifacts in the green channel for Aβ detection (white rectangle). The artifacts were visually identifiable by shape, size, and translucence (right top, raw IF), but remained after image thresholding (right middle, thresholded Aβ channel). Hence, impacted Visium spots were manually identified and excluded using their coordinates on the Visium platform (right bottom, proportion Aβ/spot).

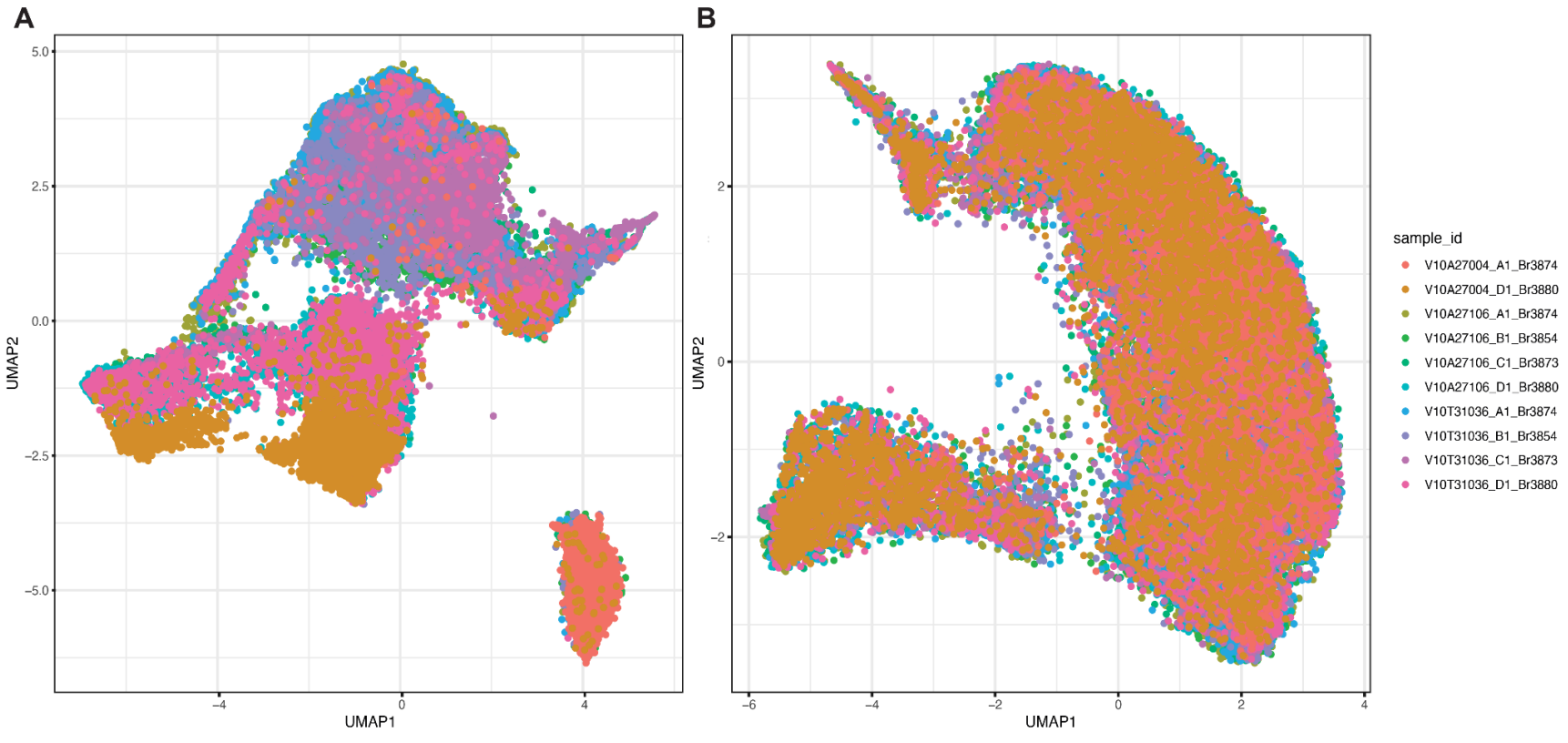

Figure S10. *Harmony*-based batch correction of Visium SRT data.

(**A**) UMAP representation of Visium spots aggregated across 10 tissue sections illustrates the effects of donor and technical variability, colored by sample IDs. (**B**) UMAP on *Harmony*-corrected PCs shows that donor effects and technical variations across multiple Visium-SPG experiments have been adjusted for.

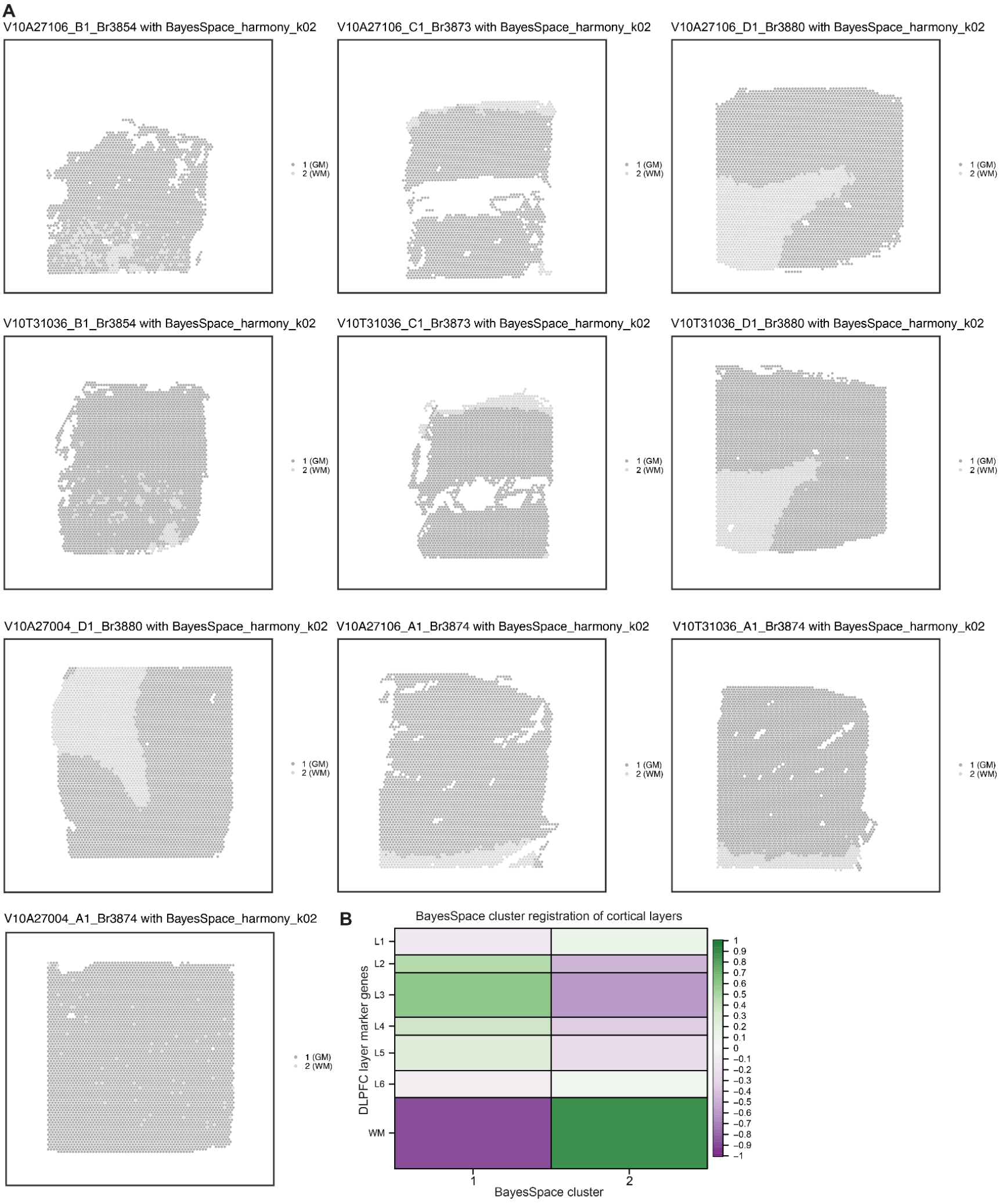

Figure S11. Unsupervised clustering with *BayesSpace* separates white and gray matter clusters in all tissue sections.

(**A**) Spotplots of 10 tissue sections depicting the cluster labels for gray matter (1, GM, dark gray) and white matter (2, WM, light gray) identified in a data-driven manner with the *BayesSpace* clustering method at *k*=2. (**B**) Spatial registration heatmap illustrating the correlation between enrichment *t*-statistics calculated on *BayeSpace* clusters at *k*=2 on x-axis and those from manually annotated layers from Maynard, Collado-Torres, et al. 2021 on the y-axis. *BayesSpace* cluster 1 is associated with the gray matter based on enrichment of genes associated with cortical layers 2-5 in DLPFC.

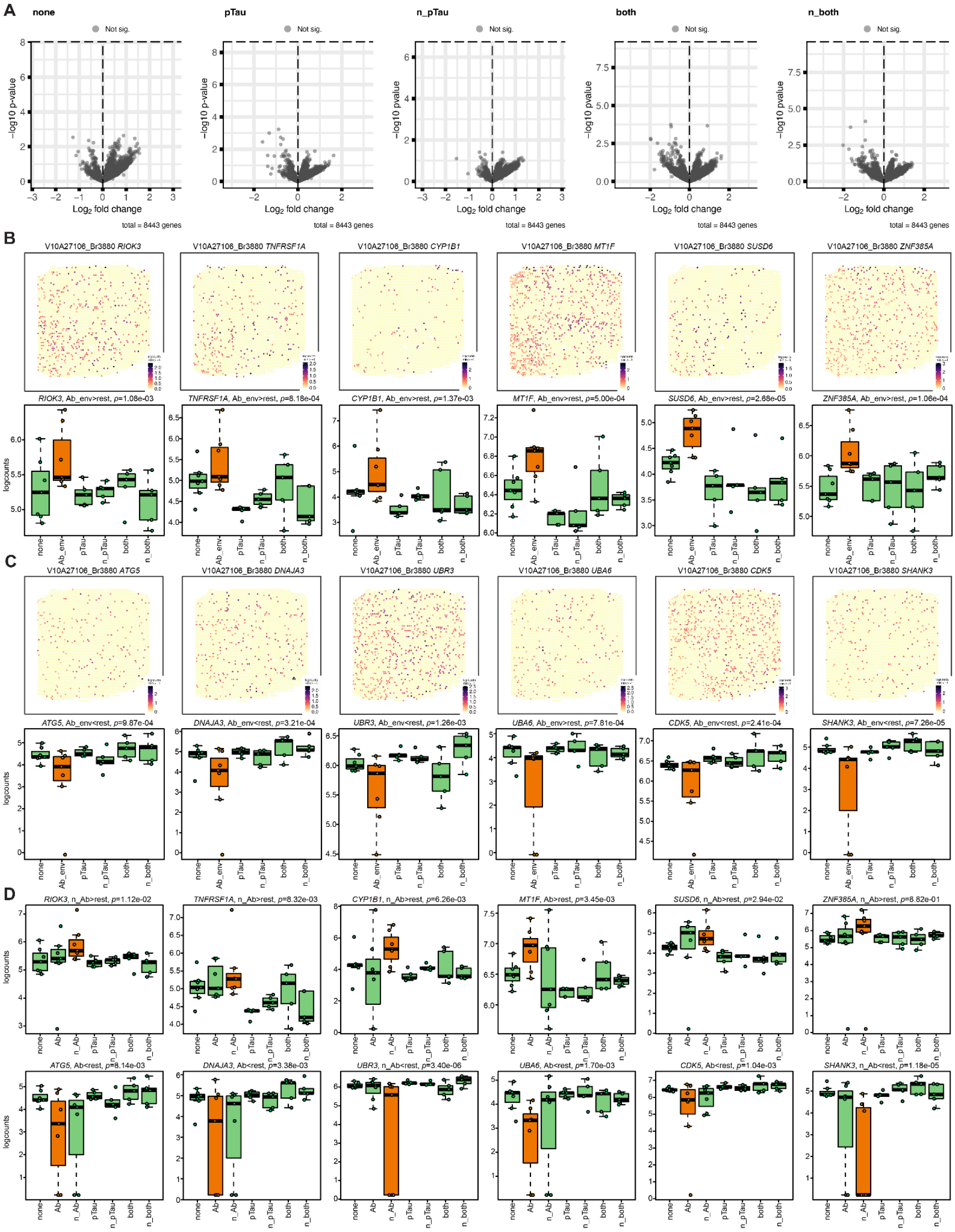

Figure S12. Inspecting biological functions and pathways of AD-associated microenvironments.

(**A**) Volcano plots depicting DEGs in 5 other AD-related pathological categories based on the enrichment model. Each dot represents a gene, plotted with its log2 fold change (x-axis) and -log10 *p*-value (y-axis), thus comparing the effect size (fold change) against the statistical evidence for differential expression (*p*-value). The dashed line represents a *p*-value threshold matching FDR<0.1, with DEGs below the line considered not significant (gray, Not sig.) No DEGs (FDR<0.1) were identified for these 5 pathological categories. For brevity, 'next' was shortened to n. (**B**) Spotplots (top) and boxplots (bottom) of 6 DEGs enriched in the extended Aβ-associated microenvironment (Ab_env). Aβ spots and Aβ-adjacent spots (next_Aβ) were collapsed into a single pathological category to represent the extended Aβ-associated microenvironment (Ab_env), which was then subjected to differential expression testing based on the enrichment model. Spotplots are from Br3880 and color scale indicates spot-level gene expression in logcounts. Boxplots display gene expression levels (logcounts) for all samples and highlight differential expression between one pathological category (orange) versus all other categories (green). For brevity, 'next' was shortened to n. (**C**) Spotplots (top) and boxplots (bottom) of 6 DEGs depleted in the extended Aβ-associated microenvironment (Ab_env). Spotplots are from Br3880 and color scale indicates spot-level gene expression in logcounts. Boxplots display gene expression levels (logcounts) for all samples and highlight differential expression between one pathological category (orange) versus all other categories (green). (**D**) Boxplots of the 12 DEGs associated with the extended Aβ-associated microenvironment (Ab_env) listed in **Figure S12B-C** to indicate their differential gene expression levels across the previously classified 7 pathological categories where Ab_env was spilt into the Aβ and next_Aβ categories. Boxplots display gene expression levels (logcounts) for all samples and highlight differential expression between one pathological category (orange) versus all other categories (green). For brevity, 'next' was shortened to n.

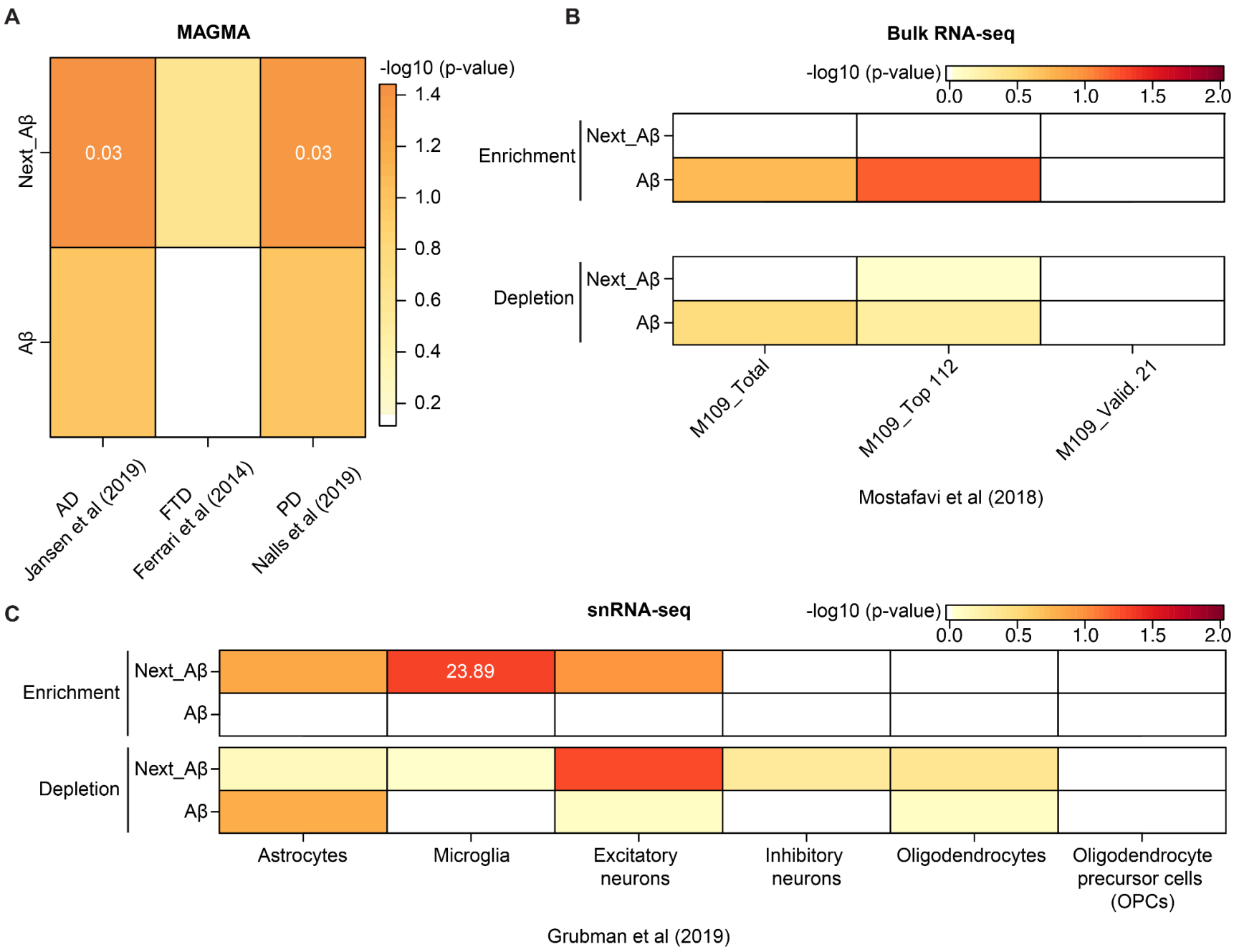

Figure S13. Enrichment of neurodegeneration- and dementia-related gene sets in Aβ-associated microenvironments.

(**A**) MAGMA associations of GWAS datasets for Alzheimer's disease (AD, Jansen et al. 2019), frontotemporal dementia (FTD, Ferrari et al. 2014), and Parkinson's disease (PD, Nalls et al. 2019) with Aβ-associated microenvironments profiled in human ITC. The results were presented in a heatmap, with the color scale indicating −log10 (*p*-value) significance of the association test. The number in each box indicates the effect size (beta) for significant associations ($p<0.05$). (**B**) Spatial gene set enrichment analysis with a bulk RNA-seq dataset of dorsolateral prefrontal cortex (DLPFC) collected from the ROSMAP cohort (Mostafavi et al. 2018). M109_Total refers to a gene module of 390 co-expressed genes strongly associated with cognitive decline and Aβ pathology in AD. M109_Top 112 is a subset of M109 containing top 112 interesting genes selected by an initial Bayesian network, while M109_Valid 21 is a gene set containing 21 validated genes. These gene sets were compared and tested for their associations with Aβ-associated microenvironments profiled for enriched (top) and depleted (bottom) gene sets in the human ITC. The results are summarized in a heatmap, with the color scale indicating −log10 (*p*-value). (**C**) Spatial gene set enrichment analysis with a snRNA-seq dataset for AD (Grubman et al. 2019). Grubman et al. identified AD-associated DEGs between case and control across 6 different cell types in the human entorhinal cortex, which were found to overlap with those identified in human DLPFC (Mathys et al. 2019). These cell type-specific gene sets were compared and tested for their associations with the Aβ-associated microenvironment in the human ITC, separated by enriched (top) and depleted (bottom) gene sets. The results are summarized in a heatmap, with the color scale indicating −log10 (*p*-value) and the numbers in the boxes indicating odd ratios for the enrichment.

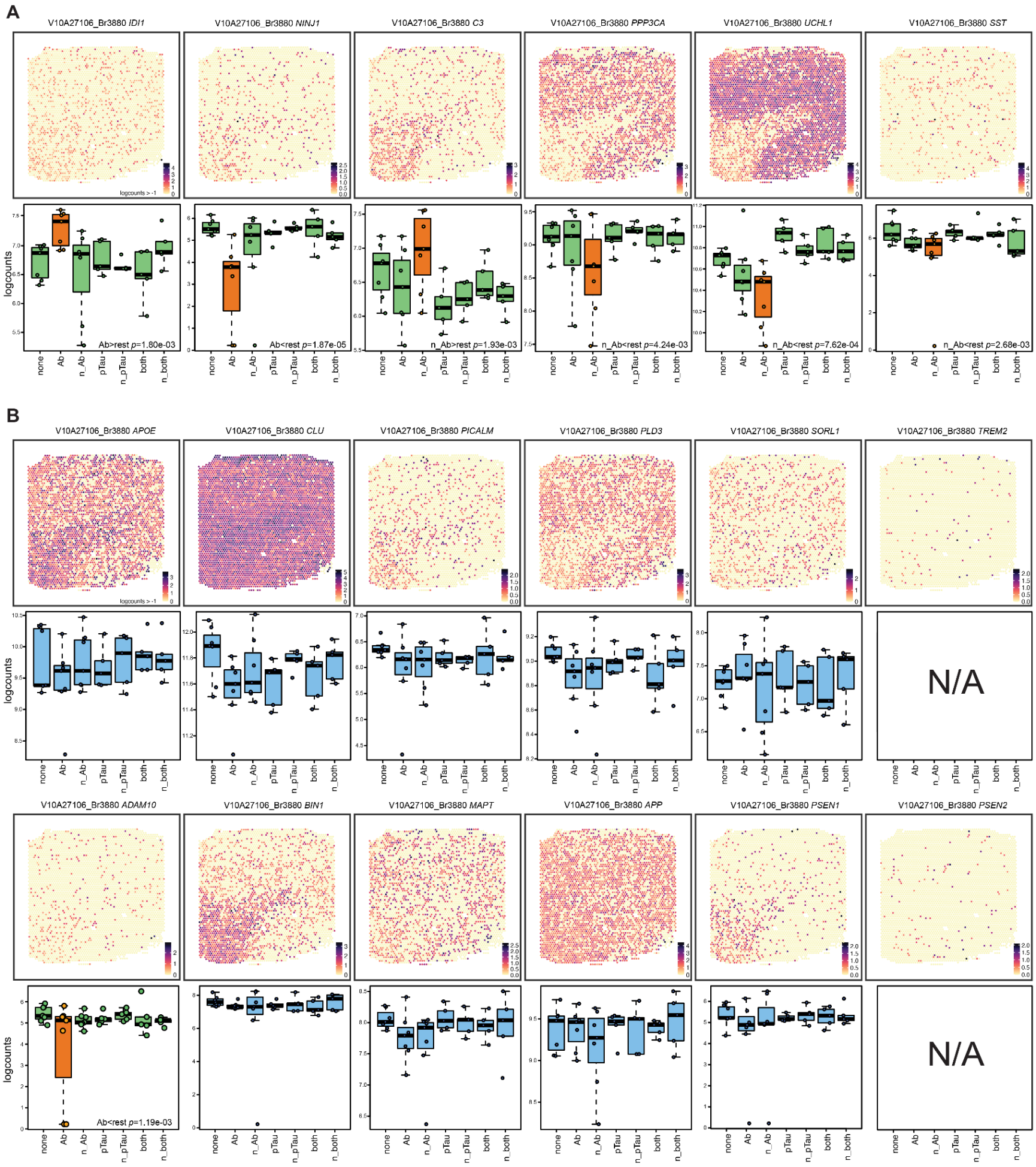

Figure S14. Spatial expression of Aβ-associated genes and AD risk genes.

(**A**) Spotplots (top) and boxplots (bottom) of 6 genes differentially expressed in Aβ and Aβ-adjacent (next_Aβ;n_Ab) pathological categories. Spotplots are from Br3880 and color scale indicates spot-level gene expression in logcounts. Boxplots display gene expression levels (logcounts) for all samples and highlight differential expression between one pathological category (orange) versus all other categories (green). For brevity, 'next' was shortened to n. (**B**) Spotplots (top) and boxplots (bottom) of selected AD-associated risk genes identified from the literature. Except for *ADAM10* (orange-green color scheme), none of these risk genes were significantly enriched or depleted across the 7 spatial categories of AD-related neuropathology (blue color scheme). *TREM2* and *PSEN2* had low tissue-wide gene expression and were thus filtered out prior to performing differential expression analysis (N/A: not available). For brevity, 'next' was shortened to n. For spotplots, color scale indicates spot-level gene expression in logcounts.

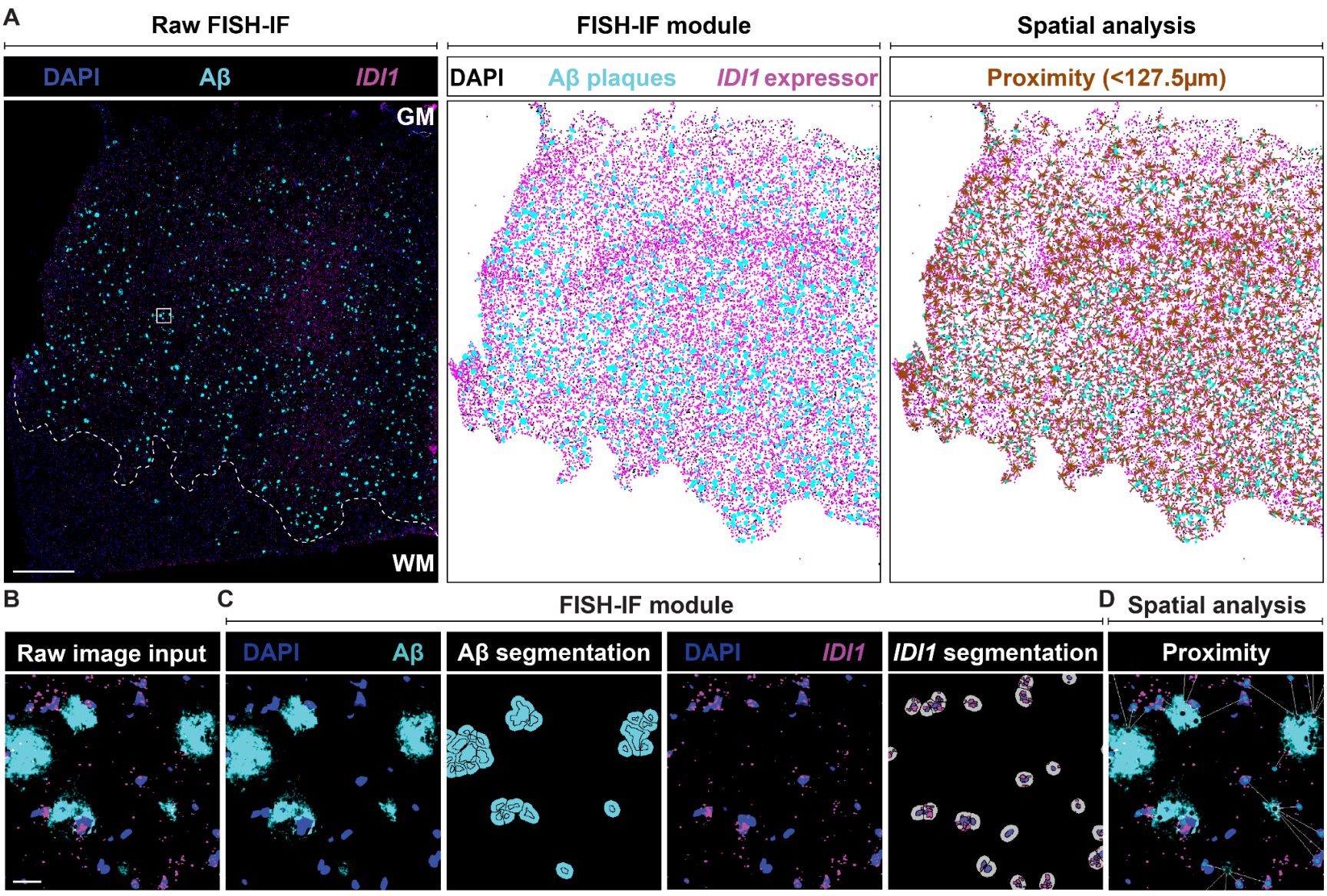

Figure S15. RNAscope FISH-IF image segmentation and quantification for spatial proximity analysis using HALO software.

(**A**) Tissue-wide image segmentation and spatial analysis of Aβ and cells expressing GOIs (GOI expressors) using gene *IDI1* and Br3854 as a representative example. RNAscope FISH-IF staining image (left) showing the distribution of Aβ (cyan) and GOI expressors (*IDI1I* expressors; magenta) throughout the entire tissue section. Based on the high density of Aβ plaques, the gray matter (GM) was manually annotated (white dashed line) and selectively incorporated into downstream image analyses. The raw staining image was computationally processed using the FISH-IF module in the HALO image analysis software to segment Aβ plaques and *IDI1* expressors (middle). Subsequent spatial analysis measured the proximity between Aβ and *IDI1* expressors with proximity lines (brown) drawn between the segmented objects distanced less than 127.5μm, a predetermined radius based on the Visium spot grid that defined the Aβ-associated microenvironment. Scale bar, 1mm. (**B**) Higher-magnification raw input image of Aβ and *IDI1* expressors. Scale bar, 25μm. (**C**) Higher-magnification demonstration of FISH-IF module segmentation of Aβ plaques and *IDI1* expressors, independently. Due to the varied pixel intensities within Aβ plaques, a single Aβ plaque (cyan) was divided into multiple fragments upon segmentation (Aβ segmentation). The *IDI1* transcript signals (magenta) were segmented as individual puncta (*IDI1* segmentation), which were then counted to measure gene expression within single cells. *IDI1* expressors were identified based on the presence of the segmented *IDI1* signals in nuclei (blue) and estimated cytoplasm (gray). The puncta outside of the nucleus and cytoplasm was not able to be quantified with this module. (**D**) Higher-magnification view of spatial analysis to determine the proximity between the centroids of the segmented fragments of Aβ plaques and neighboring *IDI1* expressors, with proximity lines (white) drawn between objects at a maximum of 127.5μm apart.

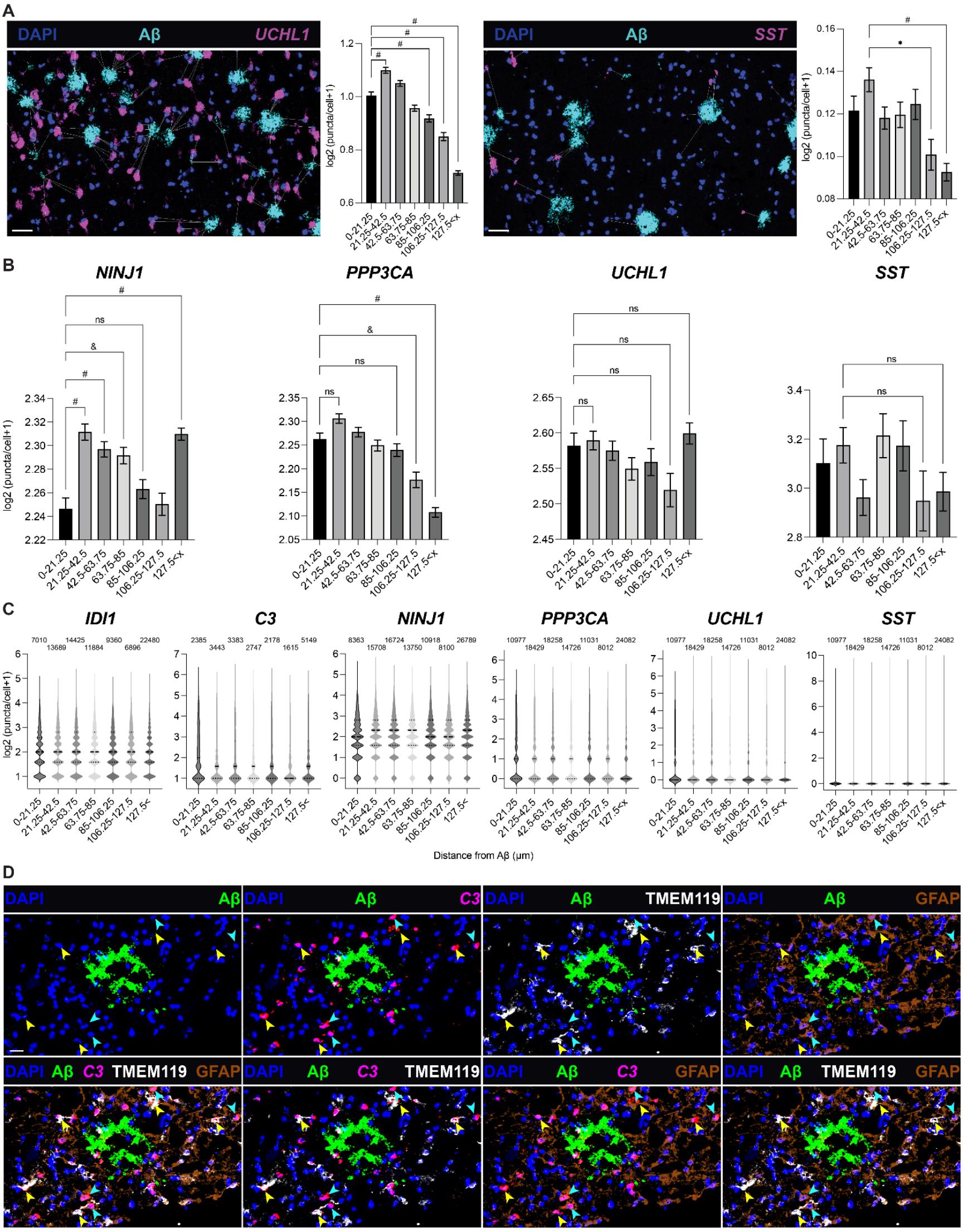

Figure S16. Validation of quantification strategies of Aβ-associated transcriptional signatures at cellular resolution.

(**A**) RNA-protein co-detection of Aβ and two GOIs, *UCHL1* (left) and *SST* (right) showing the spatial expression of the GOIs (magenta) relative to nearby Aβ. Proximity lines indicate the distance between Aβ and nearby GOI expressors (max: 127.5μm). Scale bar, 50μm. Quantification of each GOI shows gene expression changes across the 7 bins with log2 (X+1) transformation where X indicates the puncta counts. A total of cells, including GOI expressors and non-expressors, were counted to normalize gene expression for each bin. The interval for each bin was labeled on the x-axis. Data are mean ± SEM (Kruskal-Wallis test, $^{*}p<0.05$ and $^{\#}p<0.0001$). (**B**) Bar plots illustrate gene expression changes for 4 GOIs, *NINJ1*, *PPP3CA*, *UCHL1*, and *SST* across 7 distance bins when normalization was performed only with GOI expressors, as in the box plots for *IDI1* and *C3* in **Figure 3D**. Gene expression levels were quantified with log2 (X+1) transformation where X indicates the puncta counts. The distance for each bin was specified on the x-axis. Data are mean ± SEM (Kruskal-Wallis test, ns=not significant, $^{*}p<0.05$, $^{\&}p<0.005$, and $^{\#}p<0.0001$). (**C**) Violin plots showing the discrete distribution of GOI expressors with log2 (X+1) transformation where X indicates the puncta counts. The number labeled in each column indicates the total number of cells counted across the 7 bins and included for the quantification plots in **Figure 3D** and **Figure S16A**. For *IDI1* and *C3* (enriched genes), only the expressors were counted, while for *NINJ1*, *PPP3CA*, *UCHL1*, and *SST* (depleted genes), both expressors and non-expressors were counted to address potential depletion due to non-expressing cells which may artificially dilute gene expression by expressors. *PPP3CA*, *UCHL1*, and *SST* showed the same number of counted cells in every interval as their gene expression was stained and measured within the same tissue samples. (**D**) RNA-protein co-detection of Aβ (green), *C3* transcripts (magenta), TMEM119 (white), and GFAP (brown) to show enrichment of *C3* in TMEM119^{+} microglia (yellow arrowheads) and GFAP^{+} astrocytes (cyan arrowheads) in the vicinity of Aβ plaques. Scale bar, 20μm.

References

1. Schoknecht K, David Y, Heinemann U. The blood-brain barrier-gatekeeper to neuronal homeostasis: clinical implications in the setting of stroke. Semin Cell Dev Biol. 2015 Feb;38:35–42.
2. Khanna A, Kahle KT, Walcott BP, Gerzanich V, Simard JM. Disruption of ion homeostasis in the neurogliovascular unit underlies the pathogenesis of ischemic cerebral edema. Transl Stroke Res. 2014 Feb;5(1):3–16.
3. McGavern DB, Kang SS. Illuminating viral infections in the nervous system. Nat Rev Immunol. 2011 May;11(5):318–29.
4. Quail DF, Joyce JA. The microenvironmental landscape of brain tumors. Cancer Cell. 2017 Mar 13;31(3):326–41.
5. Pluvinage JV, Wyss-Coray T. Systemic factors as mediators of brain homeostasis, ageing and neurodegeneration. Nat Rev Neurosci. 2020 Feb;21(2):93–102.
6. Hemphill MA, Dauth S, Yu CJ, Dabiri BE, Parker KK. Traumatic brain injury and the neuronal microenvironment: a potential role for neuropathological mechanotransduction. Neuron. 2015 Mar 18;85(6):1177–92.
7. Kempuraj D, Thangavel R, Natteru PA, Selvakumar GP, Saeed D, Zahoor H, et al. Neuroinflammation Induces Neurodegeneration. J Neurol Neurosurg Spine. 2016 Nov 18;1(1).
8. Galloway DA, Phillips AEM, Owen DRJ, Moore CS. Phagocytosis in the brain: homeostasis and disease. Front Immunol. 2019 Apr 16;10:790.
9. Réaux-Le Goazigo A, Van Steenwinckel J, Rostène W, Mélik Parsadaniantz S. Current status of chemokines in the adult CNS. Prog Neurobiol. 2013 May;104:67–92.
10. Gupta A, Pulliam L. Exosomes as mediators of neuroinflammation. J Neuroinflammation. 2014 Apr 3;11:68.
11. Snyder SH. Neurotransmitters, receptors, and second messengers galore in 40 years. J Neurosci. 2009 Oct 14;29(41):12717–21.
12. Cummings JL. Alzheimer's disease. N Engl J Med. 2004 Jul 1;351(1):56–67.
13. Nelson PT, Braak H, Markesbery WR. Neuropathology and cognitive impairment in Alzheimer disease: a complex but coherent relationship. J Neuropathol Exp Neurol. 2009 Jan;68(1):1–14.
14. Vickers JC, Mitew S, Woodhouse A, Fernandez-Martos CM, Kirkcaldie MT, Canty AJ, et al. Defining the earliest pathological changes of Alzheimer's disease. Curr Alzheimer Res. 2016;13(3):281–7.
15. Zhang H, Wei W, Zhao M, Ma L, Jiang X, Pei H, et al. Interaction between Aβ and Tau in the Pathogenesis of Alzheimer's Disease. Int J Biol Sci. 2021 May 27;17(9):2181–92.
16. Long JM, Holtzman DM. Alzheimer disease: an update on pathobiology and treatment strategies. Cell. 2019 Oct;179(2):312–39.
17. Navarro JF, Croteau DL, Jurek A, Andrusivova Z, Yang B, Wang Y, et al. Spatial Transcriptomics Reveals Genes Associated with Dysregulated Mitochondrial Functions and Stress Signaling in Alzheimer Disease. iScience. 2020 Oct 23;23(10):101556.
18. Chen W-T, Lu A, Craessaerts K, Pavie B, Sala Frigerio C, Corthout N, et al. Spatial transcriptomics and in situ sequencing to study alzheimer's disease. Cell. 2020 Aug 20;182(4):976-991.e19.
19. Edler MK, Sherwood CC, Meindl RS, Hopkins WD, Ely JJ, Erwin JM, et al. Aged chimpanzees exhibit pathologic hallmarks of Alzheimer's disease. Neurobiol Aging. 2017 Nov;59:107–20.
20. Mckean NE, Handley RR, Snell RG. A review of the current mammalian models of alzheimer's disease and challenges that need to be overcome. Int J Mol Sci. 2021 Dec 6;22(23).
21. Halliday GM, Double KL, Macdonald V, Kril JJ. Identifying severely atrophic cortical subregions in Alzheimer's disease. Neurobiol Aging. 2003 Oct;24(6):797–806.
22. Josephs KA, Martin PR, Weigand SD, Tosakulwong N, Buciuc M, Murray ME, et al. Protein contributions to brain atrophy acceleration in Alzheimer's disease and primary age-related tauopathy. Brain. 2020 Dec 5;143(11):3463–76.
23. Scott MR, Hampton OL, Buckley RF, Chhatwal JP, Hanseeuw BJ, Jacobs HI, et al. Inferior temporal tau is associated with accelerated prospective cortical thinning in clinically normal older adults. Neuroimage. 2020 Oct 15;220:116991.
24. Maynard KR, Collado-Torres L, Weber LM, Uytingco C, Barry BK, Williams SR, et al. Transcriptome-scale spatial gene expression in the human dorsolateral prefrontal cortex. Nat Neurosci. 2021;24(3):425–36.
25. Baghallab I, Reyes-Ruiz JM, Abulnaja K, Huwait E, Glabe C. Epitomic Characterization of the Specificity of the Anti-Amyloid Aβ Monoclonal Antibodies 6E10 and 4G8. J Alzheimers Dis. 2018;66(3):1235–44.
26. Gil L, Niño SA, Chi-Ahumada E, Rodríguez-Leyva I, Guerrero C, Rebolledo AB, et al. Perinuclear Lamin A and Nucleoplasmic Lamin B2 Characterize Two Types of Hippocampal Neurons through Alzheimer's Disease Progression. Int J Mol Sci. 2020 Mar 7;21(5).
27. Hirota Y, Sakakibara Y, Ibaraki K, Takei K, Iijima KM, Sekiya M. Distinct brain pathologies associated with Alzheimer's disease biomarker-related phospho-tau 181 and phospho-tau 217 in App knock-in mouse models of amyloid-β amyloidosis. Brain Commun. 2022 Nov 6;4(6):fcac286.
28. Serrano-Pozo A, Frosch MP, Masliah E, Hyman BT. Neuropathological alterations in Alzheimer disease. Cold Spring Harb Perspect Med. 2011 Sep;1(1):a006189.
29. Delizannis AT, Nonneman A, Tsering W, De Bondt A, Van den Wyngaert I, Zhang B, et al. Effects of microglial depletion and TREM2 deficiency on Aβ plaque burden and neuritic plaque tau pathology in 5XFAD mice. Acta Neuropathol Commun. 2021 Sep 9;9(1):150.
30. Bennett RE, DeVos SL, Dujardin S, Corjuc B, Gor R, Gonzalez J, et al. Enhanced tau aggregation in the presence of amyloid β. Am J Pathol. 2017 Jul;187(7):1601–12.
31. Makin S. The amyloid hypothesis on trial. Nature. 2018 Jul;559(7715):S4–7.
32. Busche MA, Hyman BT. Synergy between amyloid-β and tau in Alzheimer's disease. Nat Neurosci. 2020 Oct;23(10):1183–93.
33. Renner M, Lacor PN, Velasco PT, Xu J, Contractor A, Klein WL, et al. Deleterious effects of amyloid beta oligomers acting as an extracellular scaffold for mGluR5. Neuron. 2010 Jun 10;66(5):739–54.
34. Rahman MM, Lendel C. Extracellular protein components of amyloid plaques and their roles in Alzheimer's disease pathology. Mol Neurodegener. 2021 Aug 28;16(1):59.

35. Arendt T, Morawski M, Gärtner U, Fröhlich N, Schulze F, Wohmann N, et al. Inhomogeneous distribution of Alzheimer pathology along the isocortical relief. Are cortical convolutions an Achilles heel of evolution? Brain Pathol. 2017 Sep;27(5):603–11.

36. Sepulcre J, Schultz AP, Sabuncu M, Gomez-Isla T, Chhatwal J, Becker A, et al. In vivo tau, amyloid, and gray matter profiles in the aging brain. J Neurosci. 2016 Jul 13;36(28):7364–74.

37. Stepanchuk AA, Barber PA, Lashley T, Joseph JT, Stys PK. Quantitative detection of grey and white matter amyloid pathology using a combination of K114 and CRANAD-3 fluorescence. Neurobiol Dis. 2021 Dec;161:105540.

38. Korsunsky I, Millard N, Fan J, Slowikowski K, Zhang F, Wei K, et al. Fast, sensitive and accurate integration of single-cell data with Harmony. Nat Methods. 2019 Dec;16(12):1289–96.

39. Zhao E, Stone MR, Ren X, Guenthoer J, Smythe KS, Pulliam T, et al. Spatial transcriptomics at subspot resolution with BayesSpace. Nat Biotechnol. 2021 Nov;39(11):1375–84.

40. Pardo B, Spangler A, Weber LM, Page SC, Hicks SC, Jaffe AE, et al. spatialLIBD: an R/Bioconductor package to visualize spatially-resolved transcriptomics data. BMC Genomics. 2022 Jun 10;23(1):434.

41. Wang Y, Tang X, Yu B, Gu Y, Yuan Y, Yao D, et al. Gene network revealed involvements of Birc2, Birc3 and Tnfrsf1a in anti-apoptosis of injured peripheral nerves. PLoS ONE. 2012 Sep 17;7(9):e43436.

42. Turner MD, Nedjai B, Hurst T, Pennington DJ. Cytokines and chemokines: At the crossroads of cell signalling and inflammatory disease. Biochim Biophys Acta. 2014 Nov;1843(11):2563–82.

43. Egusquiaguirre SP, Yeh JE, Walker SR, Liu S, Frank DA. The STAT3 Target Gene TNFRSF1A Modulates the NF-κB Pathway in Breast Cancer Cells. Neoplasia. 2018 May;20(5):489–98.

44. Song CY, Ghafoor K, Ghafoor HU, Khan NS, Thirunavukkarasu S, Jennings BL, et al. Cytochrome P450 1B1 Contributes to the Development of Atherosclerosis and Hypertension in Apolipoprotein E-Deficient Mice. Hypertension. 2016 Jan;67(1):206–13.

45. Palenski TL, Sorenson CM, Jefcoate CR, Sheibani N. Lack of Cyp1b1 promotes the proliferative and migratory phenotype of perivascular supporting cells. Lab Invest. 2013 Jun;93(6):646–62.

46. Tobi EW, Slieker RC, Stein AD, Suchiman HED, Slagboom PE, van Zwet EW, et al. Early gestation as the critical time-window for changes in the prenatal environment to affect the adult human blood methylome. Int J Epidemiol. 2015 Aug;44(4):1211–23.

47. Zhang T, Ji D, Wang P, Liang D, Jin L, Shi H, et al. The atypical protein kinase RIOK3 contributes to glioma cell proliferation/survival, migration/invasion and the AKT/mTOR signaling pathway. Cancer Lett. 2018 Feb 28;415:151–63.

48. Dai H, Wang L, Li L, Huang Z, Ye L. Metallothionein 1: A new spotlight on inflammatory diseases. Front Immunol. 2021 Nov 5;12:739918.

49. Gialeli C, Gungor B, Blom AM. Novel potential inhibitors of complement system and their roles in complement regulation and beyond. Mol Immunol. 2018 Oct;102:73–83.

50. Shang Z, Lv H, Zhang M, Duan L, Wang S, Li J, et al. Genome-wide haplotype association study identify TNFRSF1A, CASP7, LRP1B, CDH1 and TG genes associated with Alzheimer's disease in Caribbean Hispanic individuals. Oncotarget. 2015 Dec 15;6(40):42504–14.

51. Nho K, Risacher SL, Apostolova L, Bice PJ, Brosch J, Deardorff R, et al. Novel *CYP1B1-RMDN2* Alzheimer's disease locus identified by genome-wide association analysis of cerebral tau deposition on PET. medRxiv. 2023 Mar 1;

52. Yu L, Dawe RJ, Boyle PA, Gaiteri C, Yang J, Buchman AS, et al. Association Between Brain Gene Expression, DNA Methylation, and Alteration of Ex Vivo Magnetic Resonance Imaging Transverse Relaxation in Late-Life Cognitive Decline. JAMA Neurol. 2017 Dec 1;74(12):1473–80.

53. Prokopenko D, Hecker J, Kirchner R, Chapman BA, Hoffman O, Mullin K, et al. Identification of Novel Alzheimer's Disease Loci Using Sex-Specific Family-Based Association Analysis of Whole-Genome Sequence Data. Sci Rep. 2020 Mar 19;10(1):5029.

54. Myhre O, Utkilen H, Duale N, Brunborg G, Hofer T. Metal dyshomeostasis and inflammation in Alzheimer's and Parkinson's diseases: possible impact of environmental exposures. Oxid Med Cell Longev. 2013 Apr 17;2013:726954.

55. Smith AM, Davey K, Tsartsalis S, Khozoie C, Fancy N, Tang SS, et al. Diverse human astrocyte and microglial transcriptional responses to Alzheimer's pathology. Acta Neuropathol. 2022 Jan;143(1):75–91.

56. Uddin MS, Stachowiak A, Mamun AA, Tzvetkov NT, Takeda S, Atanasov AG, et al. Autophagy and alzheimer's disease: from molecular mechanisms to therapeutic implications. Front Aging Neurosci. 2018 Jan 30;10:04.

57. Castro JP, Wardelmann K, Grune T, Kleinridders A. Mitochondrial chaperones in the brain: safeguarding brain health and metabolism? Front Endocrinol (Lausanne). 2018 Apr 26;9:196.

58. Lee PCW, Sowa ME, Gygi SP, Harper JW. Alternative ubiquitin activation/conjugation cascades interact with N-end rule ubiquitin ligases to control degradation of RGS proteins. Mol Cell. 2011 Aug 5;43(3):392–405.

59. Roselli F, Livrea P, Almeida OFX. CDK5 is essential for soluble amyloid β-induced degradation of GKAP and remodeling of the synaptic actin cytoskeleton. PLoS ONE. 2011 Jul 29;6(7):e23097.

60. Wan L, Ai J-Q, Yang C, Jiang J, Zhang Q-L, Luo Z-H, et al. Expression of the excitatory postsynaptic scaffolding protein, shank3, in human brain: effect of age and alzheimer's disease. Front Aging Neurosci. 2021 Aug 24;13:717263.

61. de Leeuw CA, Mooij JM, Heskes T, Posthuma D. MAGMA: generalized gene-set analysis of GWAS data. PLoS Comput Biol. 2015 Apr 17;11(4):e1004219.

62. Jansen IE, Savage JE, Watanabe K, Bryois J, Williams DM, Steinberg S, et al. Genome-wide meta-analysis identifies new loci and functional pathways influencing Alzheimer's disease risk. Nat Genet. 2019 Mar;51(3):404–13.

63. Ferrari R, Hernandez DG, Nalls MA, Rohrer JD, Ramasamy A, Kwok JBJ, et al. Frontotemporal dementia and its subtypes: a genome-wide association study. Lancet Neurol. 2014 Jul;13(7):686–99.

64. Unable to find information for 8187858.

65. Mostafavi S, Gaiteri C, Sullivan SE, White CC, Tasaki S, Xu J, et al. A molecular network of the aging human brain provides insights into the pathology and cognitive decline of Alzheimer's disease. Nat Neurosci. 2018 Jun;21(6):811–9.

66. Grubman A, Chew G, Ouyang JF, Sun G, Choo XY, McLean C, et al. A single-cell atlas of entorhinal cortex from individuals with Alzheimer's disease reveals cell-type-specific gene expression regulation. Nat Neurosci. 2019 Dec;22(12):2087–97.

67. Li X, Wang C-Y. From bulk, single-cell to spatial RNA sequencing. Int J Oral Sci. 2021 Nov 15;13(1):36.

68. Tan WCC, Nerurkar SN, Cai HY, Ng HHM, Wu D, Wee YTF, et al. Overview of multiplex immunohistochemistry/immunofluorescence techniques in the era of cancer immunotherapy. Cancer Commun (Lond). 2020 Apr 17;40(4):135–53.

69. Pelka K, Hofree M, Chen JH, Sarkizova S, Pirl JD, Jorgji V, et al. Spatially organized multicellular immune hubs in human colorectal cancer. Cell. 2021 Sep 2;184(18):4734-4752.e20.

70. Huuki-Myers LA, Montgomery KD, Kwon SH, Page SC, Hicks SC, Maynard KR, et al. Data-driven Identification of Total RNA Expression Genes (TREGs) for Estimation of RNA Abundance in Heterogeneous Cell Types. BioRxiv. 2022 Apr 29;

71. Batiuk MY, Tyler T, Dragicevic K, Mei S, Rydbirk R, Petukhov V, et al. Upper cortical layer-driven network impairment in schizophrenia. Sci Adv. 2022 Oct 14;8(41):eabn8367.

72. Lerma-Martin C, Badia-i-Mompel P, Ramirez Flores RO, Sekol P, Hofmann A, Thaewel T, et al. Spatial cell type mapping of multiple sclerosis lesions. BioRxiv. 2022 Nov 3;

73. Ma Z, Shiao SL, Yoshida EJ, Swartwood S, Huang F, Doche ME, et al. Data integration from pathology slides for quantitative imaging of multiple cell types within the tumor immune cell infiltrate. Diagn Pathol. 2017 Sep 18;12(1):69.

74. Niazi MKK, Parwani AV, Gurcan MN. Digital pathology and artificial intelligence. Lancet Oncol. 2019 May;20(5):e253–61.

75. Borovec J, Kybic J, Arganda-Carreras I, Sorokin DV, Bueno G, Khvostikov AV, et al. ANHIR: Automatic Non-Rigid Histological Image Registration Challenge. IEEE Trans Med Imaging. 2020 Oct;39(10):3042–52.

76. Lee WJ, Brown JA, Kim HR, La Joie R, Cho H, Lyoo CH, et al. Regional Aβ-tau interactions promote onset and acceleration of Alzheimer's disease tau spreading. Neuron. 2022 Jun 15;110(12):1932-1943.e5.

77. Hanseeuw BJ, Betensky RA, Jacobs HIL, Schultz AP, Sepulcre J, Becker JA, et al. Association of amyloid and tau with cognition in preclinical alzheimer disease: A longitudinal study. JAMA Neurol. 2019 Aug 1;76(8):915–24.

78. Yang Z, Li H, Tang Y, Liu X, Liao Q, Fan C, et al. CYP1B1 deiciency ameliorates learning and memory deficits caused by high fat diet in mice. Am J Transl Res. 2019 Apr 15;11(4):2194–206.

79. Liu S-L, Wang C, Jiang T, Tan L, Xing A, Yu J-T. The role of cdk5 in alzheimer's disease. Mol Neurobiol. 2016 Sep;53(7):4328–42.

80. Steeland S, Gorlé N, Vandendriessche C, Balusu S, Brkic M, Van Cauwenberghe C, et al. Counteracting the effects of TNF receptor-1 has therapeutic potential in Alzheimer's disease. EMBO Mol Med. 2018 Apr;10(4).

81. Jhamandas JH, Mactavish D. β-Amyloid protein (Aβ) and human amylin regulation of apoptotic genes occurs through the amylin receptor. Apoptosis. 2012 Jan;17(1):37–47.

82. Ajoolabady A, Lindholm D, Ren J, Pratico D. ER stress and UPR in Alzheimer's disease: mechanisms, pathogenesis, treatments. Cell Death Dis. 2022 Aug 15;13(8):706.

83. Emmerling MR, Watson MD, Raby CA, Spiegel K. The role of complement in Alzheimer's disease pathology. Biochimica et Biophysica Acta (BBA) - Molecular Basis of Disease. 2000 Jul;1502(1):158–71.

84. Kolev MV, Ruseva MM, Harris CL, Morgan BP, Donev RM. Implication of complement system and its regulators in Alzheimer's disease. Curr Neuropharmacol. 2009 Mar;7(1):1–8.

85. Gong B, Radulovic M, Figueiredo-Pereira ME, Cardozo C. The Ubiquitin-Proteasome System: Potential Therapeutic Targets for Alzheimer's Disease and Spinal Cord Injury. Front Mol Neurosci. 2016 Jan 26;9:4.

86. Oddo S. The ubiquitin-proteasome system in Alzheimer's disease. J Cell Mol Med. 2008 Apr;12(2):363–73.

87. Zheng Q, Huang T, Zhang L, Zhou Y, Luo H, Xu H, et al. Dysregulation of Ubiquitin-Proteasome System in Neurodegenerative Diseases. Front Aging Neurosci. 2016 Dec 15;8:303.

88. Zhang Y, Zhao Y, Liu Y, Wang M, Yu W, Zhang L. Exploring the regulatory roles of circular RNAs in Alzheimer's disease. Transl Neurodegener. 2020 Sep 21;9(1):35.

89. Basel-Vanagaite L, Dallapiccola B, Ramirez-Solis R, Segref A, Thiele H, Edwards A, et al. Deficiency for the ubiquitin ligase UBE3B in a blepharophimosis-ptosis-intellectual-disability syndrome. Am J Hum Genet. 2012 Dec 7;91(6):998–1010.

90. Gomes AV. Genetics of proteasome diseases. Scientifica (Cairo). 2013 Dec 30;2013:637629.

91. Yuan X-Z, Sun S, Tan C-C, Yu J-T, Tan L. The role of ADAM10 in alzheimer's disease. J Alzheimers Dis. 2017;58(2):303–22.

92. Götz J, Ittner LM. Animal models of Alzheimer's disease and frontotemporal dementia. Nat Rev Neurosci. 2008 Jul;9(7):532–44.

93. Lee VM, Goedert M, Trojanowski JQ. Neurodegenerative tauopathies. Annu Rev Neurosci. 2001;24:1121–59.

94. Gaiteri C, Chen M, Szymanski B, Kuzmin K, Xie J, Lee C, et al. Identifying robust communities and multi-community nodes by combining top-down and bottom-up approaches to clustering. Sci Rep. 2015 Nov 9;5:16361.

95. Langfelder P, Horvath S. WGCNA: an R package for weighted correlation network analysis. BMC Bioinformatics. 2008 Dec 29;9:559.

96. Kleshchevnikov V, Shmatko A, Dann E, Aivazidis A, King HW, Li T, et al. Cell2location maps fine-grained cell types in spatial transcriptomics. Nat Biotechnol. 2022 May;40(5):661–71.

97. Biancalani T, Scalia G, Buffoni L, Avasthi R, Lu Z, Sanger A, et al. Deep learning and alignment of spatially resolved single-cell transcriptomes with Tangram. Nat Methods. 2021 Nov;18(11):1352–62.

98. Elosua-Bayes M, Nieto P, Mereu E, Gut I, Heyn H. SPOTlight: seeded NMF regression to deconvolute spatial transcriptomics spots with single-cell transcriptomes. Nucleic Acids Res. 2021 May 21;49(9):e50.

99. Dimitrov D, Türei D, Garrido-Rodriguez M, Burmedi PL, Nagai JS, Boys C, et al. Comparison of methods and resources for cell-cell communication inference from single-cell RNA-Seq data. Nat Commun. 2022 Jun 9;13(1):3224.

100. De Strooper B, Karran E. The cellular phase of alzheimer's disease. Cell. 2016 Feb 11;164(4):603–15.

101. Wang H, Kulas JA, Wang C, Holtzman DM, Ferris HA, Hansen SB. Regulation of beta-amyloid production in neurons by astrocyte-derived cholesterol. Proc Natl Acad Sci USA. 2021 Aug 17;118(33).

102. Marquer C, Laine J, Dauphinot L, Hanbouch L, Lemercier-Neuillet C, Pierrot N, et al. Increasing membrane cholesterol of neurons in culture recapitulates Alzheimer's disease early phenotypes. Mol Neurodegener. 2014 Dec 18;9:60.

103. Nugent AA, Lin K, van Lengerich B, Lianoglou S, Przybyla L, Davis SS, et al. TREM2 Regulates Microglial Cholesterol Metabolism upon Chronic Phagocytic Challenge. Neuron. 2020 Mar 4;105(5):837-854.e9.

104. Damisah EC, Rai A, Grutzendler J. TREM2: modulator of lipid metabolism in microglia. Neuron. 2020 Mar 4;105(5):759–61.

105. Langness VF, van der Kant R, Das U, Wang L, Chaves RDS, Goldstein LSB. Cholesterol-lowering drugs reduce APP processing to Aβ by inducing APP dimerization. Mol Biol Cell. 2021 Feb 1;32(3):247–59.

106. Rudajev V, Novotny J. Cholesterol as a key player in amyloid β-mediated toxicity in Alzheimer's disease. Front Mol Neurosci. 2022 Aug 25;15:937056.

107. Nakamura K, Mori F, Tanji K, Miki Y, Yamada M, Kakita A, et al. Isopentenyl diphosphate isomerase, a cholesterol synthesizing enzyme, is localized in Lewy bodies. Neuropathology. 2015 Oct;35(5):432–40.

108. Liddelow SA, Guttenplan KA, Clarke LE, Bennett FC, Bohlen CJ, Schirmer L, et al. Neurotoxic reactive astrocytes are induced by activated microglia. Nature. 2017 Jan 26;541(7638):481–7.

109. Hartmann K, Sepulveda-Falla D, Rose IVL, Madore C, Muth C, Matschke J, et al. Complement 3+-astrocytes are highly abundant in prion diseases, but their abolishment led to an accelerated disease course and early dysregulation of microglia. Acta Neuropathol Commun. 2019 May 22;7(1):83.

110. Liu K, Wang Y, Li H. The Role of Ninjurin1 and Its Impact beyond the Nervous System. Dev Neurosci. 2020;42(5–6):159–69.

111. Newton K, Dixit VM, Kayagaki N. Dying cells fan the flames of inflammation. Science. 2021 Nov 26;374(6571):1076–80.

112. Ahn BJ, Le H, Shin MW, Bae S-J, Lee EJ, Wee H-J, et al. Ninjurin1 deficiency attenuates susceptibility of experimental autoimmune encephalomyelitis in mice. J Biol Chem. 2014 Feb 7;289(6):3328–38.

113. Chen L, Song M, Yao C. Calcineurin in development and disease. Genes Dis. 2021 Mar;

114. Tramutola A, Di Domenico F, Barone E, Perluigi M, Butterfield DA. It Is All about (U)biquitin: Role of Altered Ubiquitin-Proteasome System and UCHL1 in Alzheimer Disease. Oxid Med Cell Longev. 2016 Jan 5;2016:2756068.

115. Solarski M, Wang H, Wille H, Schmitt-Ulms G. Somatostatin in Alzheimer's disease: A new Role for an Old Player. Prion. 2018 Jan 2;12(1):1–8.

116. Tran MN, Maynard KR, Spangler A, Huuki LA, Montgomery KD, Sadashivaiah V, et al. Single-nucleus transcriptome analysis reveals cell-type-specific molecular signatures across reward circuitry in the human brain. Neuron. 2021 Oct 6;109(19):3088-3103.e5.

117. Kovacs GG, Robinson JL, Xie SX, Lee EB, Grossman M, Wolk DA, et al. Evaluating the Patterns of Aging-Related Tau Astrogliopathy Unravels Novel Insights Into Brain Aging and Neurodegenerative Diseases. J Neuropathol Exp Neurol. 2017 Apr 1;76(4):270–88.

118. Vinters HV. Cerebral amyloid angiopathy. A critical review. Stroke. 1987 Apr;18(2):311–24.

119. Iwamoto N, Nishiyama E, Ohwada J, Arai H. Distribution of amyloid deposits in the cerebral white matter of the Alzheimer's disease brain: relationship to blood vessels. Acta Neuropathol. 1997 Apr;93(4):334–40.

120. Collins-Praino LE, Francis YI, Griffith EY, Wiegman AF, Urbach J, Lawton A, et al. Soluble amyloid beta levels are elevated in the white matter of Alzheimer's patients, independent of cortical plaque severity. Acta Neuropathol Commun. 2014 Aug 17;2:83.

121. Nasrabady SE, Rizvi B, Goldman JE, Brickman AM. White matter changes in Alzheimer's disease: a focus on myelin and oligodendrocytes. Acta Neuropathol Commun. 2018 Mar 2;6(1):22.

122. Wagner J, Degenhardt K, Veit M, Louros N, Konstantoulea K, Skodras A, et al. Medin co-aggregates with vascular amyloid-β in Alzheimer's disease. Nature. 2022 Dec;612(7938):123–31.

123. Tomimoto H, Akiguchi I, Akiyama H, Ikeda K, Wakita H, Lin JX, et al. Vascular changes in white matter lesions of Alzheimer's disease. Acta Neuropathol. 1999 Jun;97(6):629–34.

124. Roher AE, Kuo Y-M, Esh C, Knebel C, Weiss N, Kalback W, et al. Cortical and leptomeningeal cerebrovascular amyloid and white matter pathology in Alzheimer's disease. Mol Med. 2003 Apr;9(3–4):112–22.

125. Ryan NS, Biessels G-J, Kim L, Nicholas JM, Barber PA, Walsh P, et al. Genetic determinants of white matter hyperintensities and amyloid angiopathy in familial Alzheimer's disease. Neurobiol Aging. 2015 Dec;36(12):3140–51.

126. van Westen D, Lindqvist D, Blennow K, Minthon L, Nägga K, Stomrud E, et al. Cerebral white matter lesions - associations with Aβ isoforms and amyloid PET. Sci Rep. 2016 Feb 9;6:20709.

127. Banerjee G, Carare R, Cordonnier C, Greenberg SM, Schneider JA, Smith EE, et al. The increasing impact of cerebral amyloid angiopathy: essential new insights for clinical practice. J Neurol Neurosurg Psychiatr. 2017 Nov;88(11):982–94.

128. Weidauer S, Wagner M, Hattingen E. White Matter Lesions in Adults - a Differential Diagnostic Approach. Rofo. 2020 Dec;192(12):1154–73.

129. Mehta RI, Schneider JA. What is "Alzheimer's disease"? The neuropathological heterogeneity of clinically defined Alzheimer's dementia. Curr Opin Neurol. 2021 Apr 1;34(2):237–45.

130. Ferrari R, Wang Y, Vandrovcova J, Guelfi S, Witeolar A, Karch CM, et al. Genetic architecture of sporadic frontotemporal dementia and overlap with Alzheimer's and Parkinson's diseases. J Neurol Neurosurg Psychiatr. 2017 Feb;88(2):152–64.

131. Arneson D, Zhang Y, Yang X, Narayanan M. Shared mechanisms among neurodegenerative diseases: from genetic factors to gene networks. J Genet. 2018 Jul;97(3):795–806.

132. Romito-DiGiacomo RR, Menegay H, Cicero SA, Herrup K. Effects of Alzheimer's disease on different cortical layers: the role of intrinsic differences in Abeta susceptibility. J Neurosci. 2007 Aug 8;27(32):8496–504.

133. Leng K, Li E, Eser R, Piergies A, Sit R, Tan M, et al. Molecular characterization of selectively vulnerable neurons in Alzheimer's disease. Nat Neurosci. 2021 Feb;24(2):276–87.

134. Braak H, Thal DR, Ghebremedhin E, Del Tredici K. Stages of the pathologic process in Alzheimer disease: age categories from 1 to 100 years. J Neuropathol Exp Neurol. 2011 Nov;70(11):960–9.

135. Poe GR, Foote S, Eschenko O, Johansen JP, Bouret S, Aston-Jones G, et al. Locus coeruleus: a new look at the blue spot.

Nat Rev Neurosci. 2020 Nov;21(11):644–59.

136. Mathys H, Davila-Velderrain J, Peng Z, Gao F, Mohammadi S, Young JZ, et al. Single-cell transcriptomic analysis of Alzheimer's disease. Nature. 2019 Jun;570(7761):332–7.

137. Black S, Phillips D, Hickey JW, Kennedy-Darling J, Venkataraaman VG, Samusik N, et al. CODEX multiplexed tissue imaging with DNA-conjugated antibodies. Nat Protoc. 2021 Aug;16(8):3802–35.

138. Ben-Chetrit N, Niu X, Swett AD, Sotelo J, Jiao MS, Stewart CM, et al. Integration of whole transcriptome spatial profiling with protein markers. Nat Biotechnol. 2023 Jan 2;

139. Liu Y, DiStasio M, Su G, Asashima H, Enninful A, Qin X, et al. High-plex protein and whole transcriptome co-mapping at cellular resolution with spatial CITE-seq. Nat Biotechnol. 2023 Feb 23;

140. Hunter S, Brayne C. Do anti-amyloid beta protein antibody cross reactivities confound Alzheimer disease research? J Negat Results Biomed. 2017 Jan 26;16(1):1.

141. Neddens J, Temmel M, Flunkert S, Kerschbaumer B, Hoeller C, Loeffler T, et al. Phosphorylation of different tau sites during progression of Alzheimer's disease. Acta Neuropathol Commun. 2018 Jun 29;6(1):52.

142. Williams CG, Lee HJ, Asatsuma T, Vento-Tormo R, Haque A. An introduction to spatial transcriptomics for biomedical research. Genome Med. 2022 Jun 27;14(1):68.

143. Janesick A, Shelansky R, Gottscho A, Wagner F, Rouault M, Beliakoff G, et al. High resolution mapping of the breast cancer tumor microenvironment using integrated single cell, spatial and in situ analysis of FFPE tissue. BioRxiv. 2022 Oct 7;

144. Fang R, Xia C, Close JL, Zhang M, He J, Huang Z, et al. Conservation and divergence of cortical cell organization in human and mouse revealed by MERFISH. Science. 2022 Jul;377(6601):56–62.

145. Hasin Y, Seldin M, Lusis A. Multi-omics approaches to disease. Genome Biol. 2017 May 5;18(1):83.

146. Takei Y, Yun J, Zheng S, Ollikainen N, Pierson N, White J, et al. Integrated spatial genomics reveals global architecture of single nuclei. Nature. 2021 Feb;590(7845):344–50.

147. Kreitmaier P, Katsoula G, Zeggini E. Insights from multi-omics integration in complex disease primary tissues. Trends Genet. 2023 Jan;39(1):46–58.

148. Lipska BK, Deep-Soboslay A, Weickert CS, Hyde TM, Martin CE, Herman MM, et al. Critical factors in gene expression in postmortem human brain: Focus on studies in schizophrenia. Biol Psychiatry. 2006 Sep 15;60(6):650–8.

149. Zandi PP, Jaffe AE, Goes FS, Burke EE, Collado-Torres L, Huuki-Myers L, et al. Amygdala and anterior cingulate transcriptomes from individuals with bipolar disorder reveal downregulated neuroimmune and synaptic pathways. Nat Neurosci. 2022 Mar 7;25(3):381–9.

150. Hyman BT, Phelps CH, Beach TG, Bigio EH, Cairns NJ, Carrillo MC, et al. National Institute on Aging-Alzheimer's Association guidelines for the neuropathologic assessment of Alzheimer's disease. Alzheimers Dement. 2012 Jan;8(1):1–13.

151. Benavides SH, Monserrat AJ, Fariña S, Porta EA. Sequential histochemical studies of neuronal lipofuscin in human cerebral cortex from the first to the ninth decade of life. Arch Gerontol Geriatr. 2002 Jun;34(3):219–31.

152. Moreno-García A, Kun A, Calero O, Medina M, Calero M. An Overview of the Role of Lipofuscin in Age-Related Neurodegeneration. Front Neurosci. 2018 Jul 5;12:464.

153. Maynard KR, Tippani M, Takahashi Y, Phan BN, Hyde TM, Jaffe AE, et al. dotdotdot: an automated approach to quantify multiplex single molecule fluorescent in situ hybridization (smFISH) images in complex tissues. Nucleic Acids Res. 2020 May 8;

154. Tippani M, Divecha HR, Catallini II JL, Weber LM, Kwon SH, Spangler A, et al. VistoSeg: processing utilities for high-resolution Visium/Visium-IF images for spatial transcriptomics data (supplementary material). Figshare. 2022;

155. 10x Genomics. spaceranger count, 10x Genomics [Internet]. [cited 2022 Apr 17]. Available from: https://support.10xgenomics.com/spatial-gene-expression/software/pipelines/latest/using/count

156. Righelli D, Weber LM, Crowell HL, Pardo B, Collado-Torres L, Ghazanfar S, et al. SpatialExperiment: infrastructure for spatially-resolved transcriptomics data in R using Bioconductor. Bioinformatics. 2022 May 26;38(11):3128–31.

157. Lun ATL, McCarthy DJ, Marioni JC. A step-by-step workflow for low-level analysis of single-cell RNA-seq data with Bioconductor. [version 2; peer review: 3 approved, 2 approved with reservations]. F1000Res. 2016 Aug 31;5:2122.

158. Márquez-Jurado S, Díaz-Colunga J, das Neves RP, Martinez-Lorente A, Almazán F, Guantes R, et al. Mitochondrial levels determine variability in cell death by modulating apoptotic gene expression. Nat Commun. 2018 Jan 26;9(1):389.

159. Parodi-Rullán R, Sone JY, Fossati S. Endothelial mitochondrial dysfunction in cerebral amyloid angiopathy and alzheimer's disease. J Alzheimers Dis. 2019;72(4):1019–39.

160. Osorio D, Cai JJ. Systematic determination of the mitochondrial proportion in human and mice tissues for single-cell RNA-sequencing data quality control. Bioinformatics. 2021 May 17;37(7):963–7.

161. McCarthy DJ, Campbell KR, Lun ATL, Wills QF. Scater: pre-processing, quality control, normalization and visualization of single-cell RNA-seq data in R. Bioinformatics. 2017 Apr 15;33(8):1179–86.

162. Robinson MD, McCarthy DJ, Smyth GK. edgeR: a Bioconductor package for differential expression analysis of digital gene expression data. Bioinformatics. 2010 Jan 1;26(1):139–40.

163. Robinson MD, Oshlack A. A scaling normalization method for differential expression analysis of RNA-seq data. Genome Biol. 2010 Mar 2;11(3):R25.

164. Ritchie ME, Phipson B, Wu D, Hu Y, Law CW, Shi W, et al. limma powers differential expression analyses for RNA-sequencing and microarray studies. Nucleic Acids Res. 2015 Apr 20;43(7):e47.

165. Blighe K, Rana S, Lewis M. EnhancedVolcano: Publication-ready volcano plots with enhanced colouring and labeling. 2022;

166. Wu T, Hu E, Xu S, Chen M, Guo P, Dai Z, et al. clusterProfiler 4.0: A universal enrichment tool for interpreting omics data. Innovation (Camb). 2021 Aug 28;2(3):100141.

167. Benjamini Y, Hochberg Y. Controlling the false discovery rate: a practical and powerful approach to multiple testing. Journal of the Royal Statistical Society: Series B (Methodological). 1995 Jan;57(1):289–300.

168. 1000 Genomes Project Consortium, Auton A, Brooks LD, Durbin RM, Garrison EP, Kang HM, et al. A global reference for

human genetic variation. Nature. 2015 Oct 1;526(7571):68–74.

169. Collado-Torres L, Parthiban S, Tippani M, Divecha H. LieberInstitute/Visium_SPG_AD: v0_initial. Zenodo. 2023;

170. Rue-Albrecht K, Marini F, Soneson C, Lun ATL. iSEE: Interactive SummarizedExperiment Explorer. [version 1; peer review: 3 approved]. F1000Res. 2018 Jun 14;7:741.

171. Sriworarat C, Nguyen A, Eagles NJ, Collado-Torres L, Martinowich K, Maynard KR, et al. Performant web-based interactive visualization tool for spatially-resolved transcriptomics experiments. BioRxiv. 2023 Feb 23;

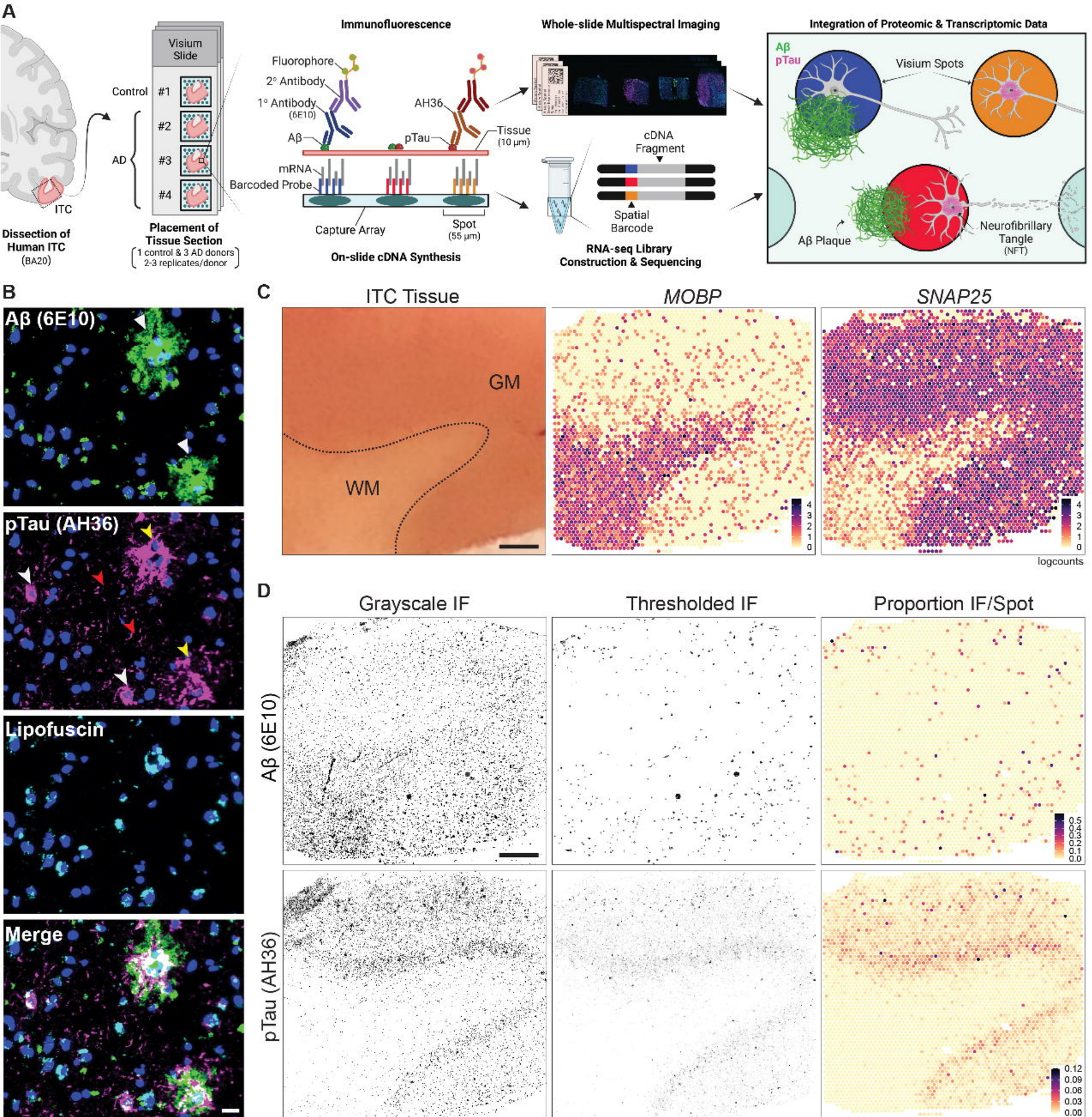
A
Visium Slide
Control
#1
#2
AD
#3
#4
ITC
Dissection of Human ITC (BA20)
Placement of Tissue Section
1 control & 3 AD donors
2-3 replicates/donor
Immunofluorescence
Fluorophore
2° Antibody
1° Antibody (6E10)
Aβ
AH36
pTau
Tissue (10 μm)
mRNA
Barcoded Probe
Capture Array
Spot (55 μm)
On-slide cDNA Synthesis
Whole-slide Multispectral Imaging
cDNA Fragment
Spatial Barcode
RNA-seq Library Construction & Sequencing
Integration of Proteomic & Transcriptomic Data
Aβ
pTau
Visium Spots
Aβ Plaque
Neurofibrillary Tangle (NFT)
B
Aβ (6E10)
pTau (AH36)
Lipofuscin
Merge
C
ITC Tissue
GM
WM
MOBP
SNAP25
4
3
2
1
0
logcounts
D
Grayscale IF
Thresholded IF
Proportion IF/Spot
Aβ (6E10)
pTau (AH36)
0.5
0.4
0.3
0.2
0.1
0.0
0.12
0.09
0.06
0.03
0.00

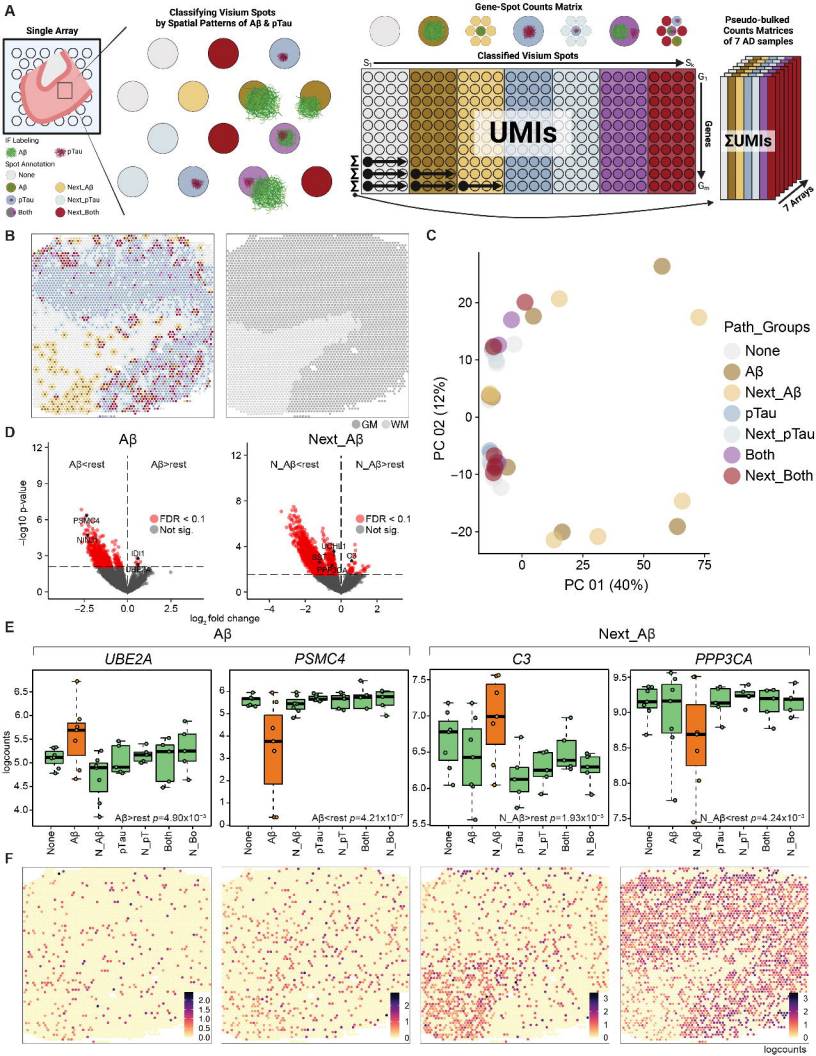
A
Single Array
Classifying Visium Spots
by Spatial Patterns of Aβ & pTau
Gene-Spot Counts Matrix
Classified Visium Spots
Pseudo-bulked
Counts Matrices
of 7 AD samples
UMIs
Genes
ΣUMIs
7 Arrays
Labeling
Aβ
pTau
Spot Annotation
None
Aβ
pTau
Both
Next_Aβ
Next_pTau
Next_Both
B
GM
WM
C
Path_Groups
None
Aβ
Next_Aβ
pTau
Next_pTau
Both
Next_Both
PC 02 (12%)
PC 01 (40%)
D
Aβ
Next_Aβ
Aβ<rest
Aβ>rest
N_Aβ<rest
N_Aβ>rest
FDR < 0.1
Not sig.
−log10 p-value
log2 fold change
PSMC4
NUP1
IQ11
UBE2A
SPHK1
C3
PPP3CA
E
Aβ
Next_Aβ
UBE2A
PSMC4
C3
PPP3CA
logcounts
Aβ>rest p=4.90x10⁻³
Aβ<rest p=4.21x10⁻⁷
N_Aβ>rest p=1.93x10⁻³
N_Aβ<rest p=4.24x10⁻³
None
Aβ
N_Aβ
pTau
N_pT
Both
N_Bo
F
logcounts

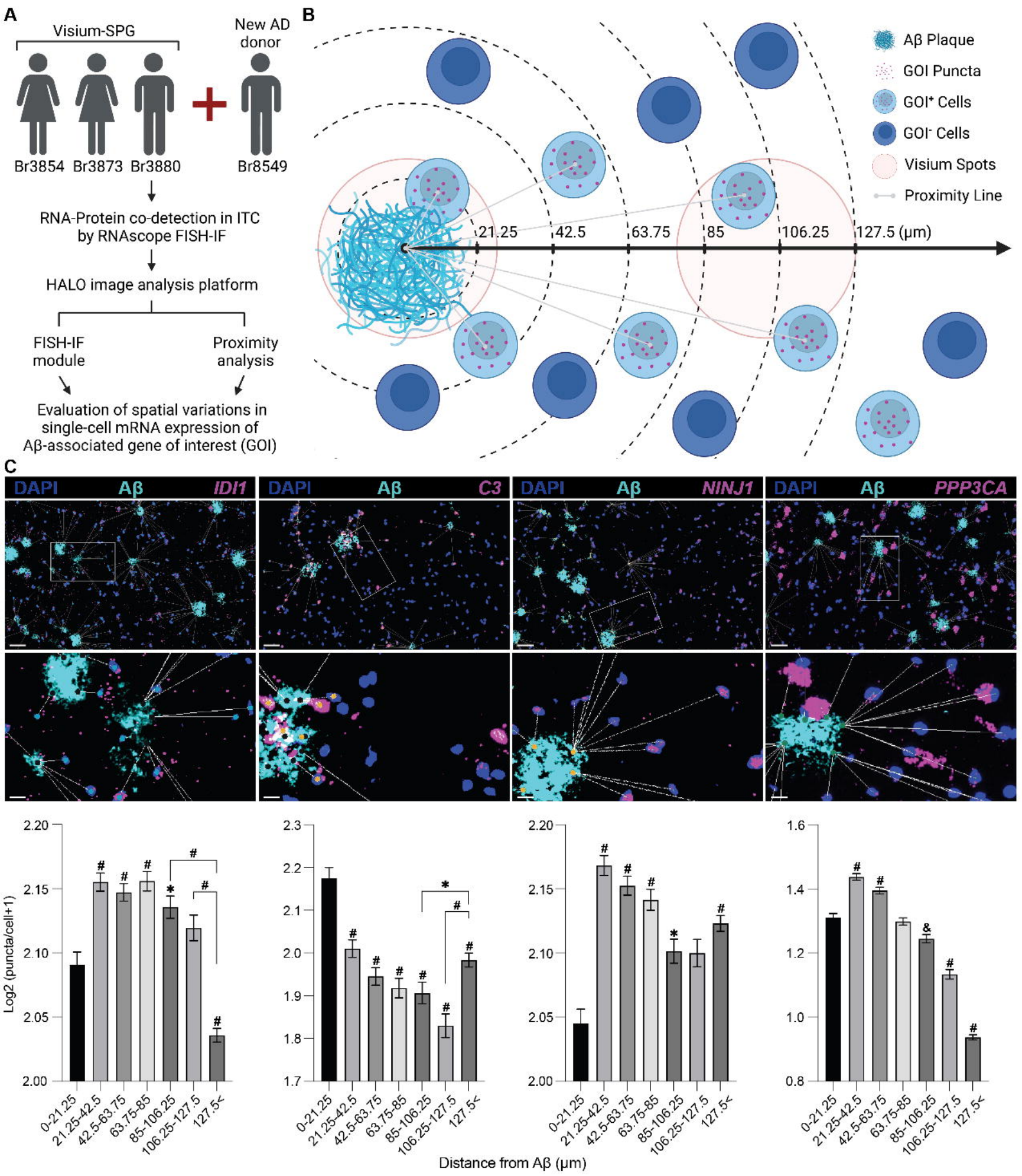
A
Visium-SPG
New AD donor
Br3854
Br3873
Br3880
Br8549
RNA-Protein co-detection in ITC by RNAscope FISH-IF
HALO image analysis platform
FISH-IF module
Proximity analysis
Evaluation of spatial variations in single-cell mRNA expression of Aβ-associated gene of interest (GOI)
B
Aβ Plaque
GOI Puncta
GOI+ Cells
GOI- Cells
Visium Spots
Proximity Line
21.25
42.5
63.75
85
106.25
127.5 (μm)
C
DAPI
Aβ
IDI1
C3
NINJ1
PPP3CA
Log2 (puncta/cell+1)
0-21.25
21.25-42.5
42.5-63.75
63.75-85
85-106.25
106.25-127.5
127.5<
Distance from Aβ (μm)